EXPERIMENTAL AND COMPUTATIONAL STUDY OF NON-WOVEN DAMAGE MECHANICS

A Dissertation

Presented to the Faculty of the Graduate School

of Cornell University

in Partial Fulfillment of the Requirements for the Degree of

Doctor of Philosophy

by

Naigeng Chen

May 2018

EXPERIMENTAL AND COMPUTATIONAL STUDY OF NON-WOVEN DAMAGE MECHANICS

Naigeng Chen, Ph.D.

Cornell University 2018

Non-wovens are of emerging industrial and research importance due to the characteristic high surface area, high porosity, high damage tolerance and low cost. Despite wide applications, predicting non-woven mechanical strength and toughness remains a difficult task. One difficulty is that non-wovens usually experience complex microstructure change at finite strains, which involves a combination of fiber stretching, fiber bending, fiber rotation and bond breakage. Another challenge comes from the lack of effective experimental method to characterize interfiber bond properties. Moreover, the fiber deformation in a non-woven is non-affine, which is different from a classical continuum solid. Modeling microscopic fiber deformation and bond fracture within a continuum mechanics framework is not yet well established.

This dissertation contributes to understand non-woven damage mechanics and to model non-woven mechanical behaviors at finite strains. First, we present a series of mechanical tests with in-situ X-ray imaging on three versions of non-woven with different areal weights. Experimental results revealed that (1) the decrease in the number of bonds in low density materials was significant, and drastic damage occurred at a lower strain than in the high density counterparts (2) no significant fiber orientation change was observed before the peak load in high areal weight non-wovens, which suggests that the inter-fiber bonds provide strong constraints on the network structure and limit fiber ro-

tation. Second, we present a novel combined experimental and computational approach to extract bond strength. The method proposed in this work carries the dual advantages of characterizing actual bonds in a non-woven and characterizing hundreds of bonds simultaneously. Third, we present a micromechanics based damage model which is built upon modeling single bond breaking process and linking local damage events to macroscopic behaviors. The model is able to reproduce experimentally observed behaviors include elastic slope, non-linear hardening slope, peak load and damage localization under uniaxial tensile loading as a function of network density. The proposed model bridges non-woven microstructure and macroscopic behaviors and thus can serve as an effective tool for future studies of the mechanics of fiber network materials.

BIOGRAPHICAL SKETCH

Naigeng Chen was born in Tianjin, China, on October 9th, 1990. He attended Yaohua Middle school from 2003 to 2008. After that, he started his undergraduate study in Tsinghua University with a major in Automotive Engineering. He did his undergraduate thesis in Automotive Crash Laboratory, under the guidance of Prof. Qing Zhou and Prof. Yong Xia. During that time, he had grown interests in research topics in solid mechanics and polymer science. In 2012, he graduated from Tsinghua and went to the United States to pursuit his PhD degree. He entered Sibley School of Mechanical and Aerospace Engineering in Cornell University, and became the first student of Prof. Meredith N. Silberstein. In 2016, he got his Master of Science degree in Mechanical Engineering field. His doctoral research involves a combination of experimental and computational study of damage mechanics of fiber network materials.

ACKNOWLEDGEMENTS

First and foremost, I would like to thank my advisor Prof. Meredith N. Silberstein. Without her guidance and support, this Ph.D. dissertation would not have been possible. I am grateful for her patience and encouragement, for the freedom she gave me to explore my research interests and for her time in training my research skills. I feel lucky to be her first Ph.D. student.

I would like to thank Prof. Paul R. Dawson, for being such a great committee member. Thank him for his support, his caring and valuable feedbacks. His lecture notes on continuum mechanics have been of great value to my graduate work. I would also like to thank my the other committee member, Prof. S. Leigh Phoenix. His knowledge of composite materials and suggestions have added great values to my research. Moreover, Prof. Shefford P. Baker, Prof. Matthew P. Miller and Prof. Alan T. Zehnder provided great comments on parts of my dissertation work which helped greatly improve my understanding of this material. I would like to thank them as well.

I would like to thank Marcia, for being so responsive and helping me with the administrative aspect of my research.

My appreciation also goes to my collaborators: Margaret K.A. Koker and Simge Uzun. I was really fortunate to obtain great supports from people in Cornell High Energy Synchrotron Source (CHESS), without whom the experimental work in this dissertation would not have been possible. I would like to thank Ernest Fontes for introducing me to the CHESS community and for promoting my work. Thank Rong for setting up X-ray beams, Zach for setting up detectors, Phil for all the helps on the software end, Eric for all the helps on the hardware end, Robin for teaching me to use her CT setup and Sean for building the test stage.

The members in Mechanics of Material Design Lab (MMD), Meenakshi, Suwon, Yuval, Jaewoo and Zelin, provided great suggestions on my research and helped me practicing conference talks. I would like to thank them all as well.

I would like to thank my friends in the general mechanics field in Cornell: Yi, Tianshu, Pankaj, Matt, Jingyi, Haibin, Darren, Xinzeng, Snow, Mincong, Jiakun and Zezhou. The discussions with these people are always very inspiring. I would like to thank my other great friends in Cornell: Huichan, Yuxing, Zhe, Lin, Liang, Xuetian, Saien, Abdullah, Yuqi, Qi, Lihai, Shuo, Chuchu, Jialie, Sunny, Peijie and Xieyue, for their accompany through these wonderful years in Ithaca.

Last but not the least, I would like to thank my dearest parents: Xin Chen and Meihua Jiang. I cannot be more grateful for their endless care and unconditional love, without which I could not have gone this far.

Part of work presented in this dissertation is based upon research conducted at CHESS which is supported by the NSF & NIH/NIGMS via NSF award DMR-1332208. Naigeng Chen is supported by CHESS, which is supported by the NSF & NIH/NIGMS via NSF award DMR-1332208. Financial support for part of this work was provided by a Cornell Affinito-Stewart grant. Xradia/Zeiss Imaging data was acquired in the Cornell BRC-Imaging Facility using the shared, NIH-funded (S10OD012287) Xradia XRM-520 nano-CT.

TABLE OF CONTENTS

LIST OF TABLES

LIST OF FIGURES

CHAPTER 1

INTRODUCTION

1.1 Non-woven materials

Non-wovens are a material class that encompasses all fabrics not manufactured by a weaving or knitting process. From a geometric point of view, non-wovens are random fiber networks in which contact fibers are bonded by different bonding techniques. Non-woven materials have advantageous physical properties including high porosity and high damage tolerance, hence have been widely used in fields including energy, water, ballistic protection, tissue engineering and medical disposables (Ahmed et al., 2015; Liu et al., 2013; Yoon et al., 2008; Huang et al., 2003; Russell, 2006). The manufacturing methods for non-wovens are versatile, and the recent advancement of electrospinning technique opens a new avenue for manufacturing multifunctional polymeric non-woven felts (Greiner and Wendorff, 2007). Non-woven constituent fibers can be made by a broad range of materials. Based on different applications, glass fiber, metallic fiber or polymeric fiber can be used (Greiner and Wendorff, 2007; Ridruejo et al., 2010; Yuranov et al., 2005). Typical bonding techniques include thermal bonding, needle punching (local entanglement) and application of external adhesives (Choi et al., 2004; Jearanaisilawong, 2008; Chen et al., 2016b). In addition to versatile manufacturing methods, non-wovens are excellent materials from the perspective of flexibility in material design. Fiber material and bonding types, as well as network microstructure (including fiber layout, fiber sizes, fiber densities and bond densities), have direct influence on non-woven mechanical behaviors as a bulk (Picu, 2011). All these features provide a rich set

of design parameters for engineers to design non-woven materials with desired functionalities or mechanical properties.

1.2 Non-woven mechanics

Non-woven mechanics is a study of the relationship between network microstructure characteristics (fiber behaviors, bond behaviors and fiber layout) and macroscopic mechanical behaviors. In this section, I will review some recent advances in the non-woven mechanics field from both experimental and material modeling perspectives.

Material scientists have found that processing conditions, like fiber extruding speed, bonding speed and bonding temperatures, directly influence non-woven morphology (fiber diameter, fiber curvature, etc.) and mechanical properties (Andreassen et al., 1995; Bhat et al., 2004; Lee et al., 2008; Michielsen and Jain, 2010; Pai et al., 2011b). For thermally bonded non-wovens, there is an optimal temperature for material strength. Material strength increases with bonding temperature due to an increase in bond sizes, but decreases beyond the optimal temperature due to premature failure of fibers at fiber-bond interfaces (Michielsen et al., 2006).

Researchers have been using experimental techniques to characterize non-woven macroscopic mechanical behaviors and monitor microstructure change with deformation. These experimental efforts provide important information on non-woven micromechanics and valuable data for material model development. Conventional tensile tests revealed that the mechanical behaviors of some polymeric non-wovens were sensitive to temperature and strain rates (Jubera

et al., 2014). Some non-wovens had anisotropic fiber layout so their mechanical behaviors were found sensitive to loading directions (Jearanaisilawong, 2008). Fracture tests showed that low fiber density non-wovens were not sensitive to stress concentrators (cracks or notches). This notch insensitivity behavior can be explained by the fact that long fiber segments transmit load away from the crack so the severity of stress concentration around the crack-tip is reduced (Ridruejo et al., 2010, 2015). Macrosopic testing does not provide much detail on non-woven microscopic deformation mechanisms. In order to monitor network microstructure change with deformation, researchers incorporated advanced imaging techniques into mechanical tests. Micro-computed tomography (μCT) generates a 3D image of a material and has been successfully applied to a variety of non-wovens such as paper (Isaksson et al., 2012), gas diffusion layers (Tötzke et al., 2014), and needle punched (Jeon et al., 2014) and point bonded non-wovens (Demirci et al., 2011). Changes in structural parameters, including pore size, fiber orientation and contact efficiency, have been computed. X-ray diffraction (XRD) experiments on fiber networks with crystalline fibers probe for information such as orientation distribution changes. The anisotropic fiber realignment behavior of a needle punched polyethylene non-woven was revealed through XRD in recent works in Martínez-Hergueta et al. (2015, 2016a).

Non-woven material models can be roughly divided into two categories: discrete models and homogenized models. For the discrete modeling strategy, each fiber and bond are modeled explicitly, using finite element method. Such discrete network models have advantages of capturing detailed load distribution and deformation profile of a network structure. Discrete network models have been used to study the effects of microstructural features (fiber density, fiber length and bond density) on macroscopic mechanical properties (Ridruejo

et al., 2010; Heyden, 2000; Bronkhorst, 2003; Kulachenko and Uesaka, 2012; Jin et al., 2013). It has been found that fiber density plays an important role in the mechanics of fiber network materials. In high density networks, fibers deform nearly affinely and individually deform axially even under local compression. In low density networks, fibers deform non-affinely and bending mode dominates (Wilhelm and Frey, 2003; Shahsavari and Picu, 2013a,b; Chen et al., 2015). Though discrete network models capture detailed physics, they are not computationally efficient. Homogenized models are useful for large specimen simulations. In the pioneering work of Cox (1952), two dimensional non-woven small deformation elastic properties were derived theoretically assuming that each material point is an assembly of long straight non-interacting fibers. The load response of a material point can be calculated as the sum of loads carried by each constituent fiber scaled by fiber density. This concept was later extended to three dimensional and finite strain cases (Narter et al., 1999; Planas et al., 2007). In recent years, many researchers have worked towards incorporating different aspects of micromechanics such as fiber undulation, fiber bending, fiber re-orientation process and local entanglement into homogenized modeling frameworks (Pai et al., 2011b; Silberstein et al., 2012; Raina and Linder, 2014; Martínez-Hergueta et al., 2016b).

Non-wovens experience progressive damage under external loading (Isaksson et al., 2006; Ridruejo et al., 2011). The damage comes from either interfiber bond fracture or fiber fracture. It has been found that interfiber bond damage usually starts accumulating at small strains and affects both mechanical strength and elasticity degradation. Therefore, a good understanding of bond damage mechanics is beneficial for modeling non-woven mechanical behaviors. Experimental techniques, including acoustic emission detection, in-

situ SEM, and in-situ computed tomography have been used to monitor bond fracture with deformation (Isaksson and Hägglund, 2007; Ridruejo et al., 2011; Chen et al., 2016a). Discrete network simulations have been used to study damage evolution laws (Aström et al., 1994; Hägglund and Isaksson, 2008; Abhilash et al., 2012). Isaksson et al. (2004) developed a constitutive model to capture anisotropic plasticity and damage evolution in paper materials. The parameters in the damage evolution law were obtained by fitting to uniaxial tensile experimental results. Ridruejo et al. (2012) used a phenomenological damage evolution law to describe the effects of bond fracture on the load carrying capacity of a fiber.

1.3 Challenges in non-woven mechanics

A good understanding of non-woven mechanics and having predictive material models at hand would greatly benefit non-woven material design. However, there are some challenges in achieving these two goals. One challenge comes from the complex deformation mechanism of a fiber network under finite deformations. Non-woven elasticity has been well studied in the past 60 years. But beyond the small deformation region, the deformation mechanisms become more complicated. Significant structural change, including fiber stretching, fiber bending, fiber rotation and bond breakage, is involved. We need a clear physical picture of the coupling between fiber deformation and bond fracture, and the relationship between microstructure and deformation mechanisms to build physically sound material models.

Another challenge comes from a lack of experimental methods in charac-

terizing bond strength, which is an important input of material models. Precise characterization of bond properties is a difficult task, since non-wovens are composed of fibers that have diameters on the order of microns or less. One strategy for determining bond strength is to directly test individual bonds with either a specially designed tensile testing apparatus or an atomic force microscope (AFM) (Torgnysdotter et al., 2007b; Schmied et al., 2012, 2013; Kulachenko and Uesaka, 2012). For these kinds of experiments, individual fiber-fiber bonds were made independently rather than extracted from a non-woven. Whether the result reflects bond properties within actual non-woven product needs further proof since the fabrication process of a bond specimen might be different from the actual manufacturing process. Further, testing individual bonds one at a time is laborious. As an alternative strategy, peel tests are efficient for characterizing hundreds of bonds at the same time (Koubaa and Koran, 1995; Yousefi Shivyari et al., 2016). Peel tests provide Mode-I interlayer bonding energy in layered non-woven materials. An average bond energy can be estimated considering the number of bonds on the interface. A drawback of this method is that individual bond strength cannot be determined. Considering that bond strength usually has great variance (Schmied et al., 2012, 2013), it is important to have a detailed description of bond strength distributions.

Apart from complex deformation mechanisms and a lack of bond strength determination method, incorporating non-woven micromechanics information into a homogenized material model is another difficult task. As mentioned in Section 1.2, discrete network simulations capture all micromechanics features but are computationally heavy and can hardly be used in real world applications. If we choose to model non-wovens within a continuum mechanics framework, we need to be careful since fiber (microscopic) deformation in network

structures is non-affine in contrast to classical continua. The linkage between macroscopic mechanical behaviors and microscopic deformation (fiber stretching and bond breakage) has not yet been well established.

1.4 Organization and contributions

In this dissertation, I focus on studying the following three topics: (1) elucidating non-woven deformation mechanisms at finite strains (2) providing an effective and efficient technique for characterizing interfiber bond strength distributions, and (3) building a micromechanics constitutive model to capture damage evolution in different density non-wovens.

The non-wovens that I used throughout this dissertation are from Dupont Typar geotextile series. The three investigated non-wovens, SF20, SF32 and SF65, are differentiated by areal weight and fiber volume fraction. Both quantities increase following the sequence: SF20, SF32 and SF65. All these materials are made by long continuous polypropylene fibers with 40 μm to 60 μm diameter. The fiber segment length (bond-to-bond distance) of these three materials are approximately 0.24mm, 0.19mm and 0.13mm, respectively. It has been found that specimen size has strong effects on non-woven mechanical behaviors (Shahsavari and Picu, 2013b). In this dissertation, I used 9mm×27mm size specimens for macroscopic mechanical characterization. The results of this size specimens are found to be reasonably representative of bulk materials. 2mm×2mm specimens are used to obtain bond strength information. The mechanical behaviors of this small size specimens are very different from bulk materials. The tensile responses of 2mm×2mm specimens are more similar to

stretching individual fibers since typically several fibers will span the entire distance from grip to grip. A more detailed discussion of size effects on this type of geotextile is included in Chapter 2 supplementary material 2.5.

The organization of this dissertation is detailed below.

In Chapter 2, we present our experimental observations of deformation mechanisms in the Typar non-woven series. We incorporate two X-ray imaging techniques into conventional mechanical tests to monitor network microstructure change with deformation. In-situ micro-computed tomography was used to image the 3D microstructures at different strains. We found that the number of bonds and volume fraction decrease in low density materials were more significant than high density counterparts. In-situ X-ray diffraction was used to track fiber orientation evolution in both monotonic tensile and stress relaxation tests. It was found that no significant fiber orientation change was observed before peak stress in high areal weight non-wovens, which suggests the inter-fiber bonds provide strong constraints on the network structure and limit fiber rotation. This work reveals the importance of bond damage on the deformation mechanism of non-wovens and provides thorough microstructural data sets for the model development and validation.

In Chapter 3, a novel combined experimental and computational approach to extract bond strengths is presented. In this method, a small specimen is imaged and the obtained 3D geometry of the network is directly modeled in a finite element framework. Bond properties are determined by matching the finite element simulation predicted mechanical response to the experimental data. This method is demonstrated by applying it to a commercial polypropylene non-woven. Validation of the obtained bond strength values was conducted with

larger size artificial network simulations and peel tests. The proposed method in this chapter carries the dual advantages of characterizing actual bonds in a non-woven and characterizing hundreds of bonds simultaneously. The method can be applied to a variety of non-woven fabrics that are bonded at fiber-fiber intersections.

In Chapter 4, a micromechanics damage model for non-wovens is presented. The model is built upon modeling single bond breaking processes and linking local damage events to macroscopic behaviors. In this model, a nonlinear term is introduced to describe how the non-affine deformation of fibers results in loading of a bond. The traction load on a bonded interface is determined by considering local force balance and network constraints. A bond breaks when its traction load exceeds a critical value, and this local information is used to update the global damage state through a classical continuum damage mechanics framework. Spatial correlation of damage in a network structure is modeled using a non-local averaging scheme. The proposed model is applied to the Typar non-woven series as an example application. The proposed model captures elasticity, non-linear hardening, peak load and progressive degradation after peak load in different density non-wovens. Damage states predicted in numerical simulations match well with the in-situ imaging results presented in Chapter 2, demonstrating the predictive capability of the model.

In Chapter 5, I conclude my dissertation with thoughts on future work.

CHAPTER 2

IN-SITU X-RAY STUDY OF THE DEFORMATION MECHANISMS OF NON-WOVEN POLYPROPYLENE

2.1 Introduction

Non-wovens are fibrous materials manufactured without a weaving or knitting process. A typical non-woven consists of a set of fibers oriented according to a manufacturing process determined statistical distribution. Due to versatile manufacturing methods, high porosity and high impact absorption capabilities, non-woven materials constitute a rapidly growing portion of the textile industry, with demonstrated applications in a variety of fields including energy, water, ballistic protection, tissue engineering and medical disposables (Ahmed et al., 2015; Liu et al., 2013; Yoon et al., 2008; Huang et al., 2003; Russell, 2006). Non-woven mechanics are complex and still poorly understood due to the random nature of fiber distributions and their evolution under straining (Picu, 2011). A better understanding of the relationship between microstructure and macroscale mechanical behavior will improve and accelerate the non-woven design process.

The relationship of non-woven elasticity to microstructure and constituent material has been established with increasing fidelity over the last 60 years. In pioneering work conducted by Cox (1952), the elastic properties of a fiber network consisting of long, straight, non-interacting fibers were established to depend on the initial fiber orientation, fiber cross-sectional area, and intrinsic fiber elastic modulus. This framework was later extended to 3D fiber orientation distributions (Narter et al., 1999). Later studies revealed that initial fiber cur-

vature and fiber bending can both significantly influence elastic network properties (Wilhelm and Frey, 2003; Shahsavari and Picu, 2012; Pai et al., 2011b,a), decreasing stiffness and increasing in-plane Poisson's ratio. Sparse networks with high fiber length to diameter aspect ratios tend toward bending-dominated rather than stretching-dominated elasticity (Wilhelm and Frey, 2003; Shahsavari and Picu, 2012).

The relationship of non-woven mechanical properties to microstructure and constituent material under large deformation remains challenging to establish due to the combination of fiber deformation, fiber orientation, and fiber-fiber contact change. Material strength depends on both specimen size and boundary conditions with long range correlations among stresses in the fibers (Hatami-Marbini and Picu, 2009; Kulachenko and Uesaka, 2012). Prior work on thermally-bonded polypropylene non-wovens demonstrated that bond damage leads to extensive fiber realignment. The speed of the realignment process results in strain rate dependent failure modes (Ridruejo et al., 2011; Jubera et al., 2014). In order to properly describe the large transverse strain observed in high aspect ratio non-wovens in uniaxial tensile tests, fiber elastic-plastic bending needed to be considered (Silberstein et al., 2012). Bond damage is the main damage mechanism in paper-like materials (Isaksson et al., 2004, 2006). Bronkhorst (2003) studied the elastic-plastic behavior of a 2D fiber network and found that neglecting connectivity through the thickness caused a significant disparity with experiment results.

One promising avenue to understanding non-woven mechanics is to characterize microstructure change during deformation. Micro-computed tomography (μCT) generates a 3D image of a material and has been successfully applied

to a variety of non-wovens such as paper (Isaksson et al., 2012), gas diffusion layers (Tötzke et al., 2014), and needle punched (Jeon et al., 2014) and point bonded non-wovens (Demirci et al., 2011). Changes in structural parameters, including pore size, fiber orientation and contact efficiency, have been computed. X-ray diffraction (XRD) experiments on fiber networks with crystalline fibers probe for information such as orientation distribution changes. The anisotropic fiber realignment behavior of a needle punched polyethylene non-woven was revealed through XRD in a recent work by Martínez-Hergueta et al. (2015).

The aim of this work is to elucidate the deformation mechanisms of a series of polypropylene (PP) non-wovens and explore the effects of areal weight on mechanical behavior. Through the application of synchrotron radiation, non-woven microstructure changes under uniaxial tensile loading were imaged. Structural information (number of bonds, volume fraction and fiber orientation distribution) was extracted to quantitatively describe damage progression and the fiber realignment process. Specifically, μCT was used to visualize the deformed material configurations at strains spanning elastic, pre-, and post-yield regions. It was observed that low areal weight non-woven had more damage than high areal weight counterparts at the same strain. Moreover, XRD experiments were used to continuously track local fiber orientation changes in both monotonic tensile and stress relaxation tests. The kinematic constraints imposed by bonds were apparent through the limited fiber realignment in high areal weight non-wovens at small strains. The experimental results also indicated whether fiber bending was a significant deformation mode for each of the different areal weight non-wovens.

2.2 Experimental

2.2.1 Materials

The Dupont Typar geotextile series of non-wovens used in this investigation are composed of PP fibers with diameters ranging in size from 40 μm to 60 μm. The fibers are created by extrusion and stretched to induce a semi-crystalline structure. These fibers are randomly distributed and bonded into a sheet by applying simultaneous heat and pressure (DuPont, 2014). The manufacturing process results in both isolated fibers and small fiber bundles within the material (Ridruejo et al., 2011). The three investigated non-wovens, SF20, SF32 and SF65, are differentiated by thickness, areal weight, and the fiber-filled volume fraction of the material (Table 2.1). All three quantities increase following the sequence: SF20, SF32, SF65. These materials essentially consist of layers of fibers, however most fibers do cross between layers over relatively short distances. SF20, SF32, and SF65 have approximately 7, 9, and 12 layers of fibers respectively.

Table 2.1: Material properties of the investigated non-wovens provided by the manufacturer (DuPont, 2014), where $v_f = a_w/(t\rho_{fiber})$ and $\rho_{fiber} = 946$ kg/m^3.

Material Type	Thickness t (mm)	Areal weight a_w (g/m^2)	Volume fraction v_f
SF20	0.35	68	0.205
SF32	0.43	110	0.270
SF65	0.59	220	0.394

2.2.2 Characterization of mechanical behavior

A Zwick/Roell Z010 testing system was used to characterize the mechanical properties of the non-wovens and single PP fibers under uniaxial tension. The load was recorded using a 10 kN and a 20 N load cell for non-woven and fiber tests, respectively. Five specimens of each non-woven type were tested to capture specimen dependent variation. Rectangular non-woven specimens 45 mm in length and 9 mm in width were tested with the gauge length set to 27 mm. This gauge dimension was chosen to achieve uniaxial tension while keeping the width small enough to image with the μCT setup (explained in section 2.2.3). A limited set of experiments were also performed on larger and smaller specimens with results provided in the supplementary materials 2.5. The width and thickness of each specimen were measured at three different locations with a micrometer to determine an average initial cross-sectional area. To create single fiber specimens, fibers were extracted from non-woven SF20 by tweezers and then glued on a cardboard template, spanning across a 15 mm cut-out region on the cardboard. The single fiber had circular cross section area and the diameter was measured at nine locations under an optical microscope prior to testing. Force and crosshead displacement were converted to engineering stress and engineering strain by dividing by the initial cross-sectional area and the initial gauge length respectively. Specimens were elongated at a constant strain rate of 0.00588 s^{-1} until failure to determine the Young's modulus E, strength σ_f and failure strain ϵ_f. Cyclic tests were carried out at a strain rate of 0.00588 s^{-1} for loading, unloading, and reloading portions; strains at the start of the unloading steps range from 0.02 to 0.8. The unloading modulus was calculated from the first 0.02 strain of each unload. To investigate relaxation behavior, another set of specimens were stretched at a constant strain rate of 0.00588 s^{-1} to an engineer-

ing strain of 0.1 and held at constant strain for 10 min. A stretched exponential function (Williams and Watts, 1970) was fit to the normalized stress relaxation curve to obtain a characteristic relaxation time.

2.2.3 Synchrotron X-ray studies

X-ray studies were performed at the F3 beamline at the Cornell High Energy Synchrotron Source (CHESS). A Si(111) double crystals monochromator was used to tune the incident X-ray beam energy to 10 keV and 8 keV for the μCT and XRD experiments, respectively. The resulting energy bandwidth was on the order of 10^4. For the μCT imaging, the second Si(111) crystal was replaced with a 5° miscut Si(111) crystal to increase the size of the incident beamspot on the specimen and allow for a larger imaging region. A custom-built dual actuator load frame (see supplementary material 2.5) was used at the F3 beamline for in-situ deformation throughout the X-ray experiments. The same 27 mm by 9 mm gauge section was used for all X-ray experiments as for the Zwick mechanical testing.

Micro-computed tomography

Changes in the 3D microstructure of the non-woven specimens, induced by deformation, were monitored using in-situ μCT imaging. The experimental setup is shown in Figure 2.1a. The X-ray beamsize was 7 mm by 7 mm. An LSO:Tb scintillator, a lens system and an Andor Neo 5.5 sCMOS detector were employed to convert the attenuated X-ray beam passing through the specimen into absorption contrast radiographs. For each tomograph (μCT scan), the specimen

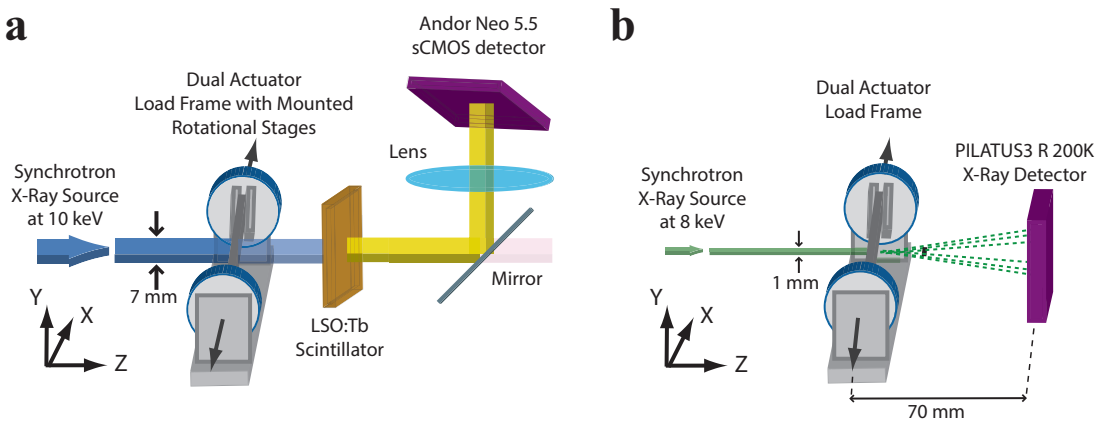

Figure 2.1: (a) Schematic of in-situ μCT experimental setup. The load frame stretches the specimen to a specific strain and then rotates the specimen 180° as absorption radiographs from the incident synchrotron beam are recorded with a CMOS detector. (b) Schematic of in-situ XRD experimental setup. The load frame stretches the specimen continuously as diffraction patterns from the incident synchrotron beam are recorded on an X-ray detector.

was rotated 180° about the loading axis in 0.25° steps (721 radiographs total). Sets of radiographs with 0.5 s exposure time were acquired. A 5 min relaxation time was added before each scan to ensure morphology change during imaging was minimal. Dark images (closed shutter) and beam profile images (open shutter, no specimen) were also acquired using the same exposure time. Elongation of the non-woven specimens was incremented in a step-wise manner to strains of 0, 0.01, 0.02, 0.1, 0.15 and 0.3. At each of the 6 strains, a scan was performed. Specimen dimensions and the methods of mechanical testing are the same as used for the mechanical behavior characterization in Section 2.2.2. Two specimens of each areal weight were tested during this experiment.

The raw radiographs, as well as beam profile and dark images, were processed into a stack of cross-sectional slices using the commercial software Octo-

pus (OctopusImaging, 2013). Each slice consisted of 1000 pixels by 1000 pixels with a corresponding pixel size of 6.5 μm. The commercial software AVIZO Fire (ThermoFisherScientific, 2014) was used for image denoising and data visualization.

Microstructural changes were quantified in terms of changes in volume fraction v_f and bond numbers. These analyses were performed with user-written Matlab R2015a scripts (TheMathworks, 2015). In order to account for the irregular material shape at finite deformation, the reconstructed volume was divided into 20×20 grids on the initial specimen plane (XY plane as shown in Figure 2.1). The reported v_f at each strain is the mean of v_f values calculated within each grid space. The v_f within each grid space was defined as the maximum v_f along the thickness direction with fixed sampling volume. Since the calculation of v_f is sensitive to the intensity threshold of the image stack, the threshold value was selected such that the initial calculated v_f of each specimen matches the values given in the material data sheet as provided in Table 2.1. Bond number is defined as the total number of connected bonding regions in the 3D image. A voxel is within a bonding region as long as its minimal distance to the background is larger than a threshold value. This bond identification approach is an upper bound estimate that utilizes the flattening caused when the nonwoven is bonded with combined heat and pressure to distinguish bonds from non-bonded contacting fibers.

X-ray diffraction

In-situ XRD experiments provide information about fiber orientation during deformation of the non-wovens. The experimental setup is shown in Figure 2.1b.

The x-ray beamsize on the specimen was 1 mm by 1 mm. Diffraction patterns were captured by a PILATUS3 R 200K detector placed 70 mm behind the specimen. Individual diffraction patterns were captured of six different single fibers extracted from the SF20 material. For the non-woven loading experiments, each specimen was either stretched to failure or to a certain strain and then allowed to relax, following the mechanical test methods described in Section 2.2.2. The specimens were loaded at a strain rate of 0.00588 s^{-1} corresponding to a range in strain of 0.003 per diffraction pattern. For both continuous loading and relaxation experiments, a series of XRD patterns were recorded with an exposure time of 0.5 s each.

The collected XRD patterns represent the sum of the diffraction from each of the individual fibers within the diffraction volume. The orientation distribution function is a measure of the orientation distribution of fibers in the non-woven specimen, which can be computed by resolving the intensity distribution of a diffraction ring by azimuthal angle. This diffraction pattern intensity distribution to fiber orientation distribution extraction is unique since we utilize a peak corresponding to only one orientation of the fiber. It is assumed that strain within individual fibers has negligible effect on the orientation analysis; this assumption is assessed in the supplementary material 2.5. In order to quantify the realignment process during the deformation process of non-wovens, the ensemble averaged orientation parameter p is calculated:

$$p = 2\langle \cos^2 \alpha \rangle - 1 \tag{2.1}$$

where α is the angle between fiber axis and loading axis. An in-plane randomly oriented set of fibers will have an orientation parameter value of 0. If all fibers

are aligned perpendicular to the loading axis p is -1, and if all fibers are aligned along the loading axis p is 1. Image processing and analysis calculations were performed in Matlab R2015a (TheMathworks, 2015).

2.3 Results and discussion

2.3.1 Non-woven mechanical behaviors

The non-wovens used in this study deform elastic-plastically under uniaxial tensile loading (Figure 2.2). Due to the random nature of the material, the variations in mechanical response from specimen to specimen are large. Three representative monotonic curves are included in Figure 2.2, corresponding to three tests of maximum tensile strength, median tensile strength and minimum tensile strength. The stress-strain curve of each areal weight has similar shape before the peak stress, consisting of a short linear region followed by a gradual roll over region. All of the curves are smooth at the beginning and become jagged starting around the peak stress, by which point fiber breakage is visually apparent. The three different areal weight materials are qualitatively distinct in the post-peak stress failure evolution. The failure of SF20 (lowest areal weight) progresses gradually, resulting in a long tail on the stress-strain curve. Some SF32 (intermediate areal weight) specimens undergo gradual failure, while others have sharp decreases in stress after the peak stress. All SF65 (highest areal weight) specimens have rupture-like failure. It is important to note that these specimens exhibit a more gradual damage mode than would be seen at larger specimen sizes (see supporting material). The differences in mechanical prop-

erties among the three areal weights are summarized in Table 2.2. Material of higher areal weight has higher stiffness, higher strength, later failure initiation and longer relaxation time. When the mechanical response is scaled by volume fraction, the three non-wovens have similar scaled Young's moduli, but the scaled strength of the more compact non-wovens is higher. This means that on a per weight basis the more compact material has better strength without compromising stiffness.

Material damage can be evaluated macroscopically with cyclic loading. In Figure 2.2a-c, representative cyclic stress-strain curves of three types of non-wovens are overlaid on the uniaxial tensile curves. A permanent set (non-zero strain at zero stress) is present after each unloading step for all three areal weights. This permanent set comes from a combination of fiber plastic deformation and material structure damage (Ridruejo et al., 2012). Damage also manifests as a decreased unloading slope with deformation. The differences in the degradation process among the three types of non-wovens are evident in Figure 2.2d, in which unloading slopes are normalized by the initial Young's moduli and plotted against the strains when unloading initiated. All the non-woven normalized moduli decrease once the macroscopic deformation was imposed. At each strain, normalized unloading modulus increases with increasing areal weight (SF20, SF32 and SF65).

For the three non-wovens made from the same constituent fiber and made through the same manufacturing process, high areal weight non-wovens are stiffer, stronger, less stretchy and less degraded before the large scale failure than low areal weight non-wovens. In order to better understand these observations from mechanical tests, detailed characterizations of constituent fibers

and microstructure deformation were carried out and are discussed in the following sections.

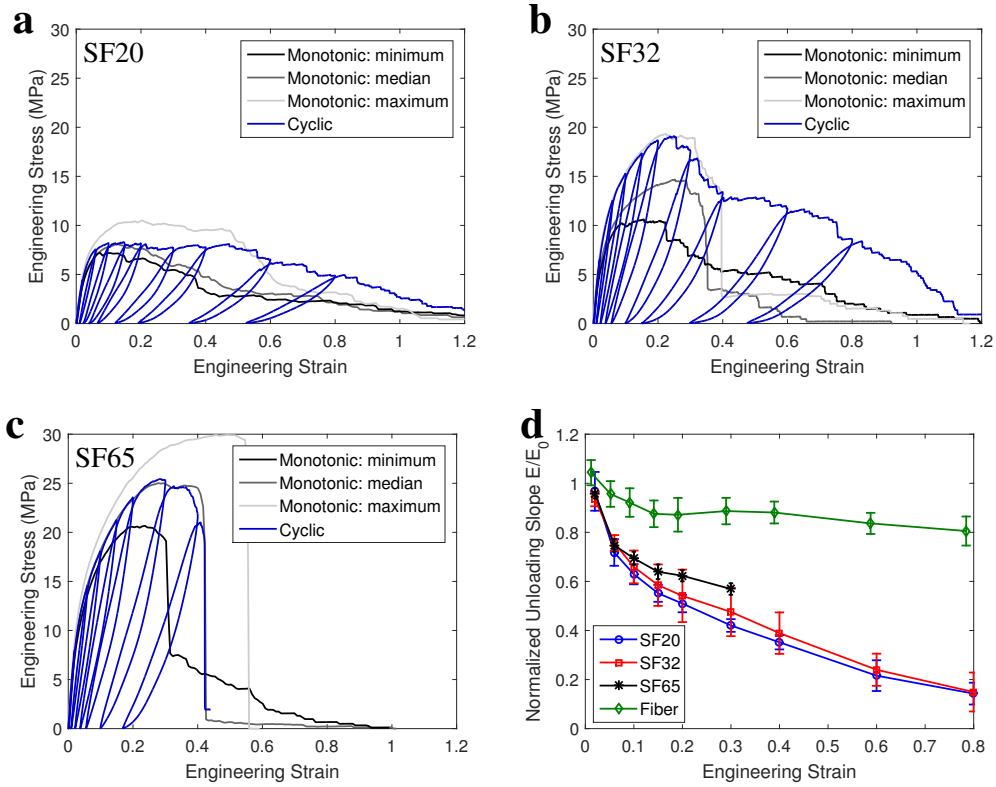

Figure 2.2: Mechanical characterization of three types of non-wovens. Monotonic and cyclic uniaxial tensile behaviors of (a) SF20, (b) SF32 and (c) SF65. Due to large specimen to specimen variations, the maximum, median and minimum strength tests are shown. (d) Normalized unloading slope versus the strain when unloading step started.

2.3.2 Fiber mechanical behaviors

The constituent fibers are elastic-visco-plastic, as is typical for thermoplastic polymers. In Figure 2.3, the tensile stress-strain curves exhibit a linear region followed by gradual yield and then linear hardening. The fracture is rupture-like, occurring around a strain of 1.3. In the cyclic tests, large hysteresis loops

Table 2.2: Mechanical properties of constituent fibers and non-wovens under uniaxial tensile loading. Young's modulus and strength are scaled by volume fraction v_f. ϵ_f is defined as the strain at peak load in an engineering stress-strain curve.

Material	Scaled modulus E/v_f (GPa)	Scaled strength σ_f/v_f (MPa)	Failure ϵ_f	Relaxation time τ (10^4 s)
Fiber	2.45 ± 0.15	293 ± 8	1.3 ± 0.3	1.9 ± 0.3
SF20	0.78 ± 0.03	31 ± 3	0.15 ± 0.06	1.39 ± 0.18
SF32	0.84 ± 0.07	42 ± 7	0.21 ± 0.06	1.66 ± 0.15
SF65	0.85 ± 0.04	52 ± 5	0.33 ± 0.08	1.83 ± 0.10

and permanent sets are observed after the unloading step, even when the fibers are stretched to small strains. The mechanical properties of fibers are listed in Table 2.2. The fiber modulus is approximately three times the scaled non-woven Young's moduli, which is consistent with theoretical predictions for non-bonded long fiber networks (Cox, 1952). This indicates that initial non-woven elasticity is at most minimally related to bond properties. The similarity of non-woven and fiber relaxation constants suggests that non-woven relaxation is due to individual fiber relaxation.

2.3.3 Non-woven 3D microstructure in tension

Non-woven deformation involves a combination of fiber deformation, relative fiber movement and bond damage. The 3D microstructures of an SF32 specimen at four different strain states are shown in Figure 2.4. Prior to deformation, the material was predominantly planar with thickness variation on the order of the fiber diameter. Fibers were randomly oriented in the specimen (XY) plane,

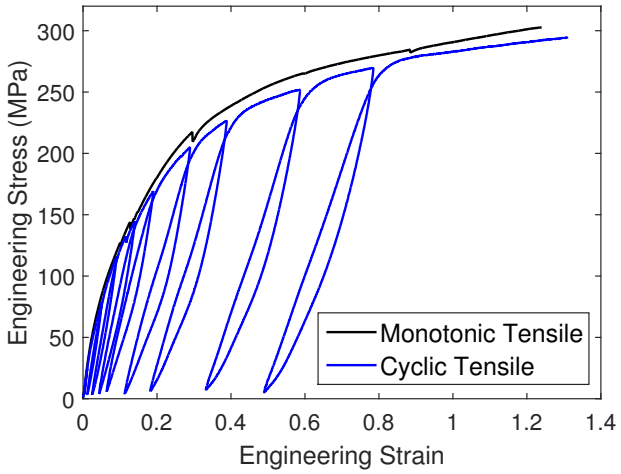

Figure 2.3: Tensile stress-strain characterizations of single PP fibers.

with corresponding non-uniform pore sizes and distributions. Interweaving is apparent among the fibers. Fibers are distorted from their cylindrical shape in contact regions between the fibers. The fibers were observed to be long with little curvature. Dangling fiber ends were not apparent except at the edges of the material. At a strain of 0.02, minimal change in material microstructure could be seen. As the specimen was stretched to a strain of 0.1, a combination of both straight and wavy fibers were observed. The wavy fibers were aligned mostly along the direction transverse to the applied tension. Some fibers bent out of the material plane forming an arc-shape structure. Overall, the material surface was no longer planar. At a strain of 0.3, consolidation of fibers across the transverse direction occurred, and the specimen edges became jagged. The majority of the fibers that remained straight were well aligned with the loading direction. Due to large scale damage, fibers separated into layers in the through thickness direction, resulting in a loosely connected network.

A comparison of the microstructures of the three non-woven types at a strain of 0.1 is shown in Figure 2.5. Of the three non-wovens, the width reduction of

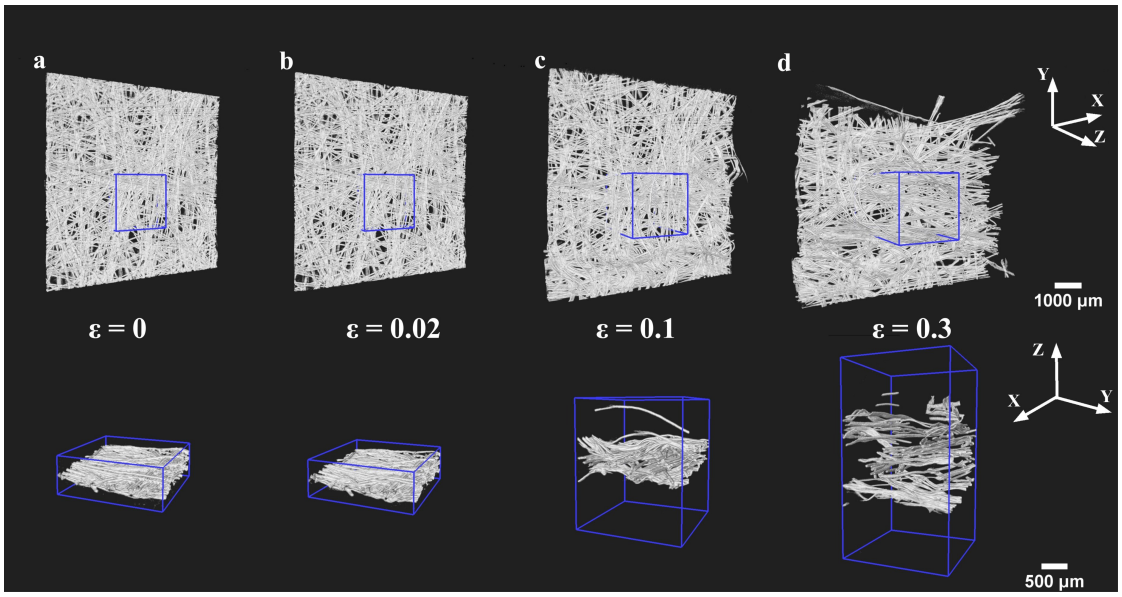

Figure 2.4: 3D microstructure images of a non-woven SF32 specimen at strains of (a) 0, (b) 0.02, (c) 0.1 and (d) 0.3. Top: full 6.5 mm by 6.5 mm reconstructed volume. Bottom: an enlarged partial view.

the SF20 specimen was the most significant. Fibers aligned with the transverse direction were mostly sinusoidal, which was evident in the loosely connected regions compressed by the surrounding highly bonded regions. In some parts of the (comparatively thin) SF20 specimen, the whole material became wavy and delamination occurred on the specimen scale. In contrast, the high areal weight non-woven, SF65, remained mostly planar at this same strain. The arced fiber segment lengths were short. Unlike the low areal weight counterparts, no large bulges formed by bundles of bending fibers were observed in SF65. The multiple layers of the non-woven help to stabilize each other and provide increased strength relative to a material consisting of independent layers.

The number of bonded regions and filled volume fraction are used here to quantitatively describe structural damage in non-wovens (Figure 2.6). Number

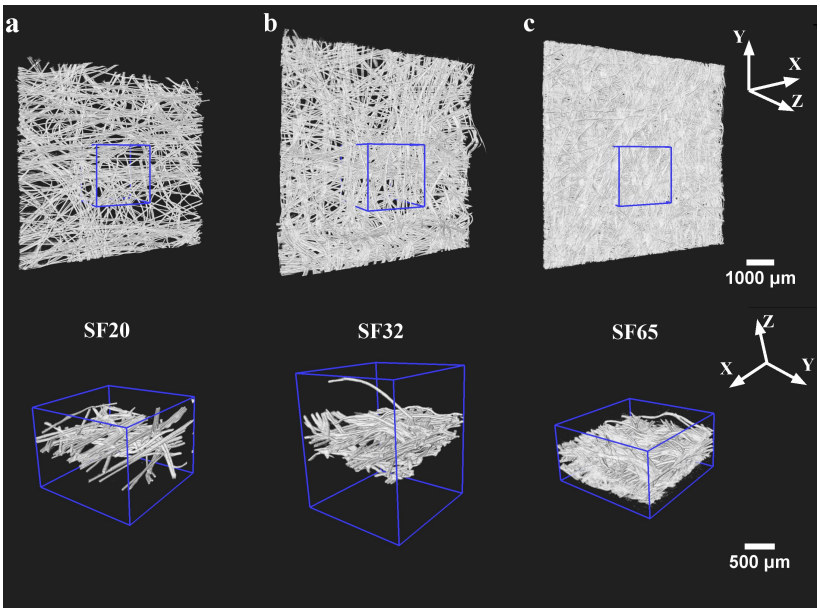

Figure 2.5: 3D microstructure images of non-woven specimens (a) SF20, (b) SF32 and (c) SF65 at a strain of 0.1. Top: full 6.5 mm by 6.5 mm reconstructed volume. Bottom: an enlarged partial view.

of bonds is a crucial characteristic, since bonds hold the fibers together and provide strength to the material. SF65 had more than double the initial bonds of SF32 and more than four times that of SF20. The number of bonds in all three non-wovens decreased starting from a strain of 0.02 indicating the bond fracture initiated at small strains. Until a strain of 0.15, the bond number drop in SF20 was almost the same as SF65. Considering the fraction of initial bonds, the relative bond fracture in SF20 was more significant. The SF32 specimen shown here has more bond fracture than SF20. Looking into the corresponding stress-strain curve (see supplementary material 2.5), it was found that this SF32 specimen is severely damaged before a strain of 0.1. In larger samples since the number of fibers engaged in supporting the load increases with increasing specimen size as the influence from artificially short fiber segments near the edge is reduced; this may result in either greater or lesser bond survival depending on the bond

strength distribution. At the onset of large scale damage, bonds over a relatively localized strip of the material are responsible for the ultimate failure of the non-woven, so the total bond count does not decrease as drastically as might otherwise be expected. Decreases in volume fraction, a result of material delamination, are indicative of interlayer bond fraction and fiber out of plane bending that locally increases the specimen thickness more than the width contracts from fiber alignment. The volume fraction of SF20 and SF32 were relatively constant until a strain of 0.02 and then decreased significantly, while the volume fraction of SF65 remained relatively constant until the scan at a strain of 0.15. The observations of decreasing number of bonds and decreasing volume fraction show that structural damage in the low areal weight non-woven initiated at smaller strains. Also, structural damage is more drastic for low areal weight material than for high areal weight ones. These conclusions support the analysis of material degradation in cyclic test section for which unloading slope decreased more drastically for the low areal weight non-woven than for the high areal weight non-woven.

2.3.4 Fiber orientation evolution under loading

Fiber orientation distribution is a key factor in determining non-woven behaviors. In non-wovens composed of ductile fibers, the degree of fiber alignment due to tensile loading is significant at finite strains (Silberstein et al., 2012; Yano et al., 2012). Fiber alignment determines how the force supported by each fiber adds up to the overall non-woven stress and is indicative of whether the non-woven accomodates deformation by fiber stretching (high energy) or fiber bending and rotation (low energy). XRD experiments were carried out in order to

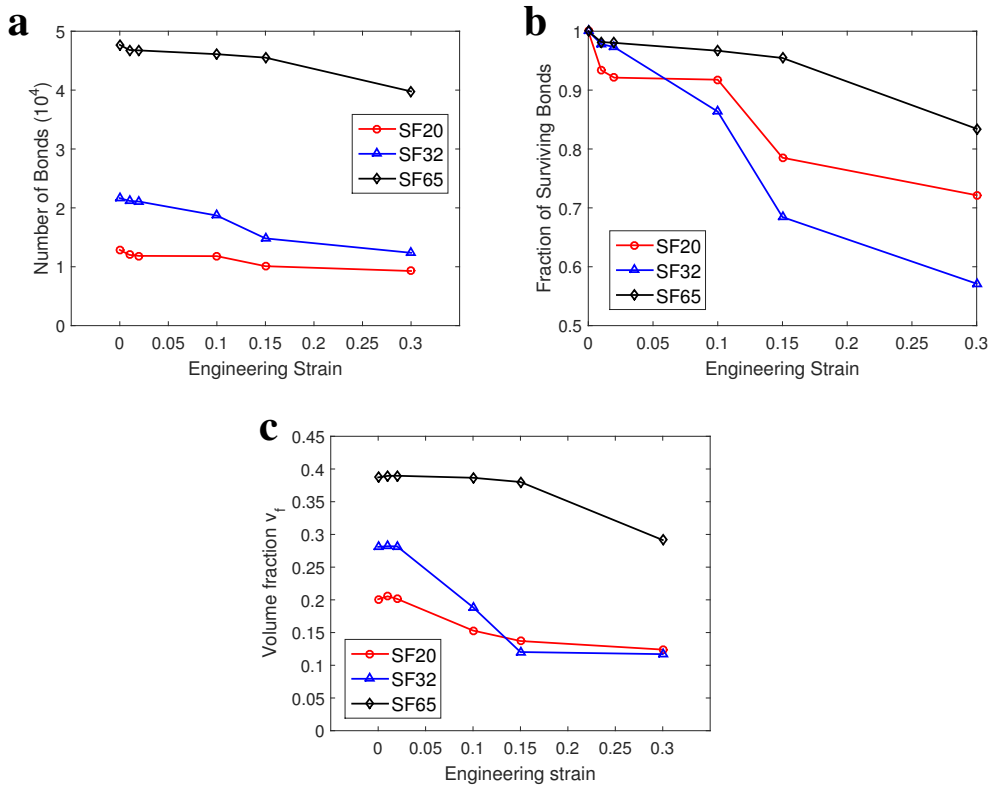

Figure 2.6: The evolution of (a) number of bonds, (b) fraction of initial bonds that remain and (c) volume fraction v_f as a function of applied strain.

study the areal weight effects on the fiber alignment.

The PP fibers present in the non-wovens are semicrystalline with axisymmetric crystalline orientation, which makes XRD a feasible method for probing fiber orientation distribution. Figure 2.7a shows the XRD pattern of a single horizontally aligned fiber (parallel to the loading axis). Three diffraction peaks are observed at an azimuthal angle of 90°, and two others peak can be seen at azimuthal angles of 50° and 130°. The 2θ angles of these peaks are 14.2°, 17.1°, 18.7° and 22.1° corresponding to crystalline planes aligned in (110), (040), (130), and (111) and (131) directions, respectively. This diffraction pattern is consistent with alpha phase PP fibers (Iijima and Strobl, 2000). Each individual fiber has

the same diffraction pattern. Therefore, a one-to-one relationship between fiber orientation and diffraction spot (2θ and azimuthal angle) location can be used to track fiber orientation in the non-woven. The intensity distribution along the azimuthal angle of a ring represents fiber angular distribution. The average diffraction pattern of an undeformed SF32 specimen is shown in Figure 2.7b.

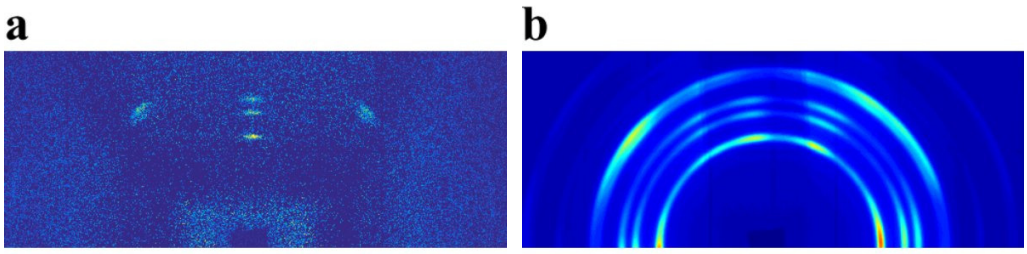

Figure 2.7: 2D XRD pattern of (a) a single PP fiber and (b)an undeformed SF32 non-woven specimen.

The fiber orientation evolution in the non-wovens during uniaxial tensile loading is shown in Figure 2.8. Detailed orientation distribution functions and a discussion of how fiber diffraction intensity change under loading affects orientation calculation results can be found in the supplementary material 2.5. Here, homogenized orientation parameter p (Equation 1) is plotted as a function of applied strain. Changes in p may differ somewhat with specimen size, particularly for SF20. The differences in the orientation evolution process among the three materials are readily apparent. The orientation parameters of SF32 and SF65 were nearly constant until a strain of 0.3 and 0.4 respectively, at which point each increased monotonically until large scale failure. The onset of realignment in both materials occurred just prior to the peak stress and the orientation parameter is much less than predicted with an affine deformation assumption (see supplementary material 2.5). On the contrary, the orientation parameter of SF20 increased from the beginning until a strain of 0.1, and then

fluctuated with no overall trend. In high areal weight non-wovens, the discrepancy between the timing of fiber reorientation and the initiation of deformation can be explained using two arguments. First, the existence of large number of bonds provides strong constraints and limits the fiber-fiber rotation. Second, due to short bond-to-bond segment lengths, fibers are more difficult to bend, and hence the fibers transverse to the loading direction kinematically inhibit rotation of partially aligned fibers with the loading direction. SF20 is a sparse network and has long fiber segment length between bonds. Bond damage quickly affects the fiber orientation with fibers tending to bend and rotate, so that fiber realignment starts at small strains. Since the incident XRD beam is only 1mm by 1mm, the exact values of these orientation parameters vary from specimen to specimen, particularly at strains larger than the peak stress for which strain inhomogeneity is significant, however these trends hold across specimens.

Even though fiber alignment was observed in all three types of non-wovens, the unloading slope decreases in the cyclic tests. This decrease demonstrates that the effect of fiber alignment is overcome by bond damage and fiber fracture. One should also note that bond fracture changes the network topology, leading to a structure in which fibers are longer and easier to bend. The orientation parameters of high areal weight non-wovens therefore change sharply (Figure 2.8) at finite strains when bond fracture reaches a great extent.

The constraints provided by bonds are also evident in the stress relaxation tests. In Figure 2.9, two representative sets of fiber orientation curves taken during relaxation tests are shown. Each plot consists of four curves corresponding to fiber orientation distributions at four different time points: the initial point, the start point of relaxation, 50 s and 100 s after relaxation. For the SF32 spec-

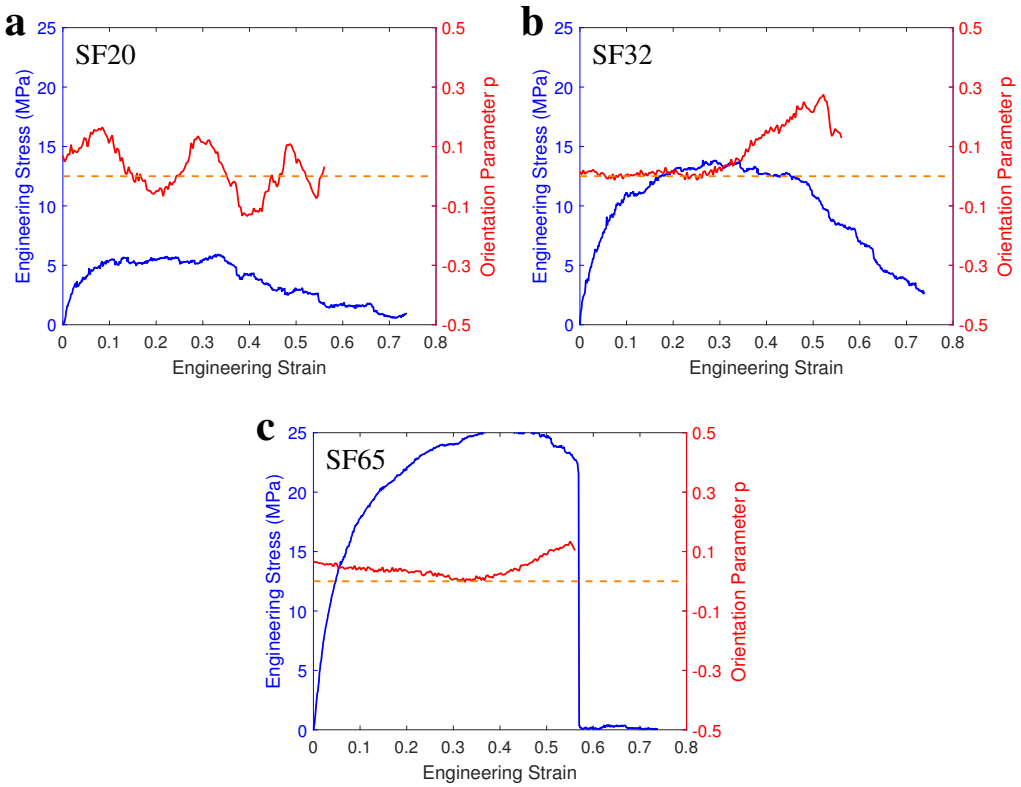

Figure 2.8: Stress and orientation parameter as a function of strain for (a) SF20, (b) SF32 and (c) SF65.

imen (and the not shown SF65), there was minimal fiber orientation change within 100 s of relaxation time. For the SF20 specimen, the number of fibers aligned in -30° and 70° changed significantly during the first 50 s of relaxation. This orientation change stems from fiber reorientation due to bond breakage as was evident in the surface images taken by an optical camera. Bond breakage during relaxation was only observed in specimens that were already largely damaged prior to relaxation. This indicates that as long as the strong bond constraints remain, the non-woven microstructure is "frozen" during the relaxation period, and the macroscopic stress relaxation mainly originates from fiber relaxation rather than structure change.

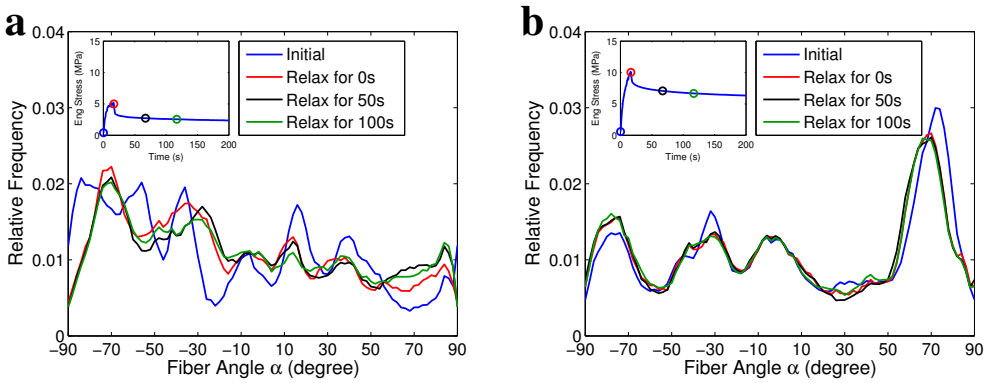

Figure 2.9: Fiber orientation change at four time points for (a) SF20 and (b) SF32. Inset: stress relaxation curve. The SF65 specimen (not shown) behaved similarly to the SF32.

2.4 Conclusion

In this chapter, the deformation mechanisms of a series of thermally-bonded PP non-wovens and the dependence of these mechanisms on areal weight were investigated. Mechanical characterization revealed the elastic-plastic behavior of the material, as well as two distinct areal weight dependent failure modes: gradual damage progression and rupture-like failure. Higher areal weight non-wovens tended to fail in a rupture-like manner, whereas lower areal weight material failed gradually (larger size specimens show similar trends, see supplementary materials 2.5). Moreover, higher areal weight non-wovens exhibited higher mass scaled strength, larger failure strain and longer relaxation time. Mechanical characterization of the constituent PP fiber revealed that the fiber is also elastic-plastic with stiffness close to three times the scaled non-woven stiffness, suggesting bond properties do not effect initial non-woven elasticity. The deformation process of three types of non-wovens were visualized by in-situ μCT experiments. As applied macroscopic strain increased, fiber bending and internal fiber layer delamination became visually apparent. In higher areal

weight material, the bending segment length was shorter and width reduction was less compared to lower areal weight material at same strain. The volume fraction and bond number decrease in the highest areal weight material (SF65) are less significant than the other two materials at low strains. At strains past the peak stress all the non-wovens exhibit a decrease in tangent stiffness and number of bonds. In-situ XRD experiments were used to track non-woven fiber orientation evolution during tensile loading and relaxation. The initiation of significant fiber realignment in high areal weight material was observed in the middle of the rollover yield region, which can be explained by the large bond number density and short bond-to-bond fiber segment length. In contrast, large scale damage occurred much earlier in the low areal weight non-woven (SF20) resulting in an irregular fiber orientation evolution process. Localized sets of fibers aligned, plastically deformed, and eventually fractured. In the stress relaxation experiments, stress decreased in all cases. Fiber orientation only occurred if large scale damage was present prior to the start of the strain hold period.

This study reveals the transition of non-woven microstructure from predominantly planar to 3D under tensile loading. The structural reorganizations observed here indicate that considering interweaving and the fiber-fiber connectivity in the thickness direction is necessary for predicting non-woven mechanical strength. Moreover, the strong influence of bond damage on the fiber realignment process points to the need to accurately capture bond properties. Each of these observations will be applied in future work.

2.5 Supplementary material

S1. Dual actuator load frame

In-situ synchrotron experiments required a device to uniaxially deform a specimen while keeping the center aligned with the X-ray beam. For μCT imaging, the specimen needed to rotate within the beamspot. In order to satisfy these requirements, a dual-actuator driven load frame was constructed (Figure 2.10). The device features two symmetrically placed frames, onto which the specimen is clamped. Uniaxial elongation of a specimen is achieved through horizontal movement of the frames, each of which is driven by a stepper motor at the base. Load and displacement signals were measured by a 250 N load cell and a step motor counter, respectively. A pair of Huber 410 goniometers enabled specimen rotation along the loading axis. The load frame was fully adjustable to allow for specimen alignment with the loading axis, perpendicular to the X-ray beam.

S2. Fiber diffraction intensity change during loading

Fiber deformation can in general affect crystalline structure by changing the lattice spacing or crystallographic orientation of the fiber. For the PP fibers tested in this investigation, the diffraction spots did not change position throughout tensile loading of single fibers, but did decrease in intensity. This intensity decrease is shown as the dotted blue line in Figure 2.11. The intensity decrease partially comes from the change of fiber volume inside the diffraction volume, due to the decrease in fiber diameter during stretching (Poisson effect). A prediction of fiber diffraction intensity change induced solely by Poisson effect is shown

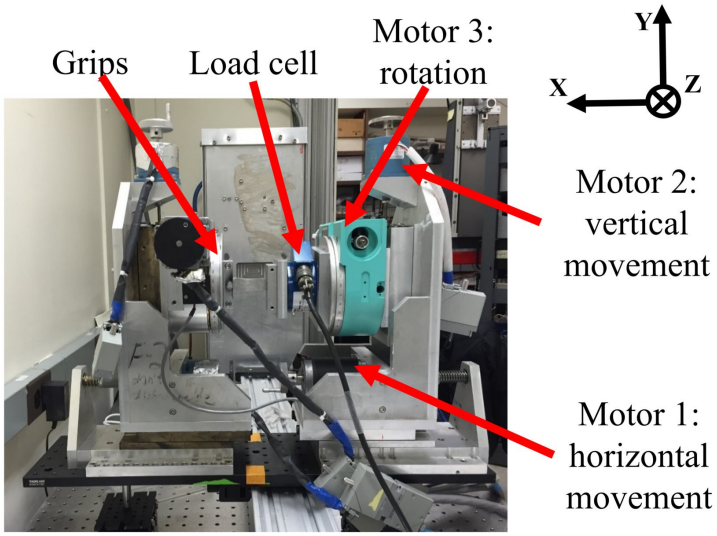

Figure 2.10: Customized dual actuator load frame for in-situ XRD and μCT experiments.

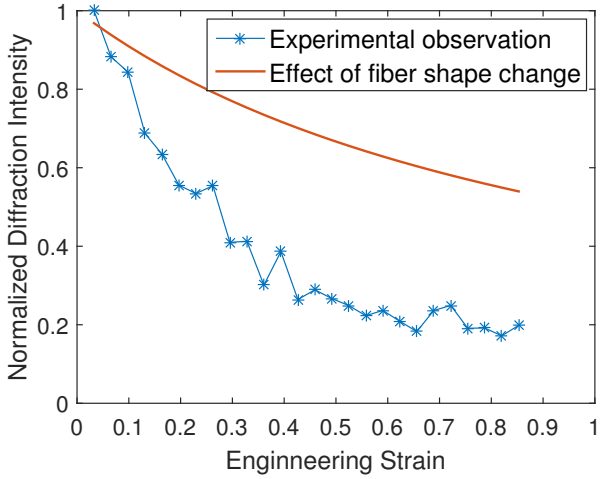

Figure 2.11: Diffraction intensity as a function of applied strain.

as the red line in Figure 2.11. The difference between the dotted blue line and red line indicates that there is another mechanism contributing to the diffraction intensity decrease. One possible explanation to this is that fiber stretching leads to some damage on the crystallite inside the fiber. We estimated the maximum

orientation parameter error could be caused by the intrinsic fiber intensity decrease using computer simulations, and found that that this error is small and does not affect the conclusions made in the X-ray diffraction section. If a 2D fiber network with the same fiber density as SF32 is deformed with affine deformation assumption, the orientation parameter error induced by the intrinsic fiber intensity decrease is around 0.01 when the macroscopic strain is 0.1.

S3. Non-woven specimen size effect

Non-wovens consist of randomly placed fibers. The stochastic nature of this material leads to different mechanical behaviors under different length scales. In this section, we report the mechanical test results of different size specimens. A discussion of how representative 27 mm long $\times$ 9 mm wide specimens are of bulk material mechanisms is also included.

Four different size specimens of each type nonwoven were tested under uniaxial tension. The dimension was scaled from 27 mm $\times$ 9 mm by factors: 2/9, 1/2, 2 and 3, while the length to width aspect ratio was kept the same (3:1). All the other mechanical test conditions were kept the same as before. Figures 2.12 and 2.13 show the overall stress-strain curves and the scaled elastic modulus, scaled strength, and failure strain respectively. All of the specimens have an apparent elastic-plastic behavior. Moving from small to large specimen size the damage mode becomes more drastic (force falls off more quickly following the peak load). SF20 at 6 mm $\times$ 2 mm is an extreme case of essentially testing single fibers spanning the grips with few enough bonds that the load is not distributed to the non-spanning fibers. This specimen size exhibits a reduced elastic mod-

ulus, highly variable strength, and a large failure strain that is similar to single fibers. SF20 at 13.5 mm × 4.5 mm and SF32 at 6 mm × 2 mm also have some single fiber like deformation behavior. The remaining specimens are all fundamentally deforming as a non-woven. This is apparent in the elastic modulus scaled by the filled volume fraction that is approximately 1/3 the fiber modulus. We note that to acquire SF65 data at the largest (81 mm × 27 mm) specimen size we had to use a tensile testing machine with an analog output since we do not own sufficient grips on our own machine, this led to higher variability in the calculated elastic modulus. The nonwoven strength arises through a number of factors which do not have the same dependence on specimen size (fiber plasticity, fiber fracture stress, stress distribution among the fiber network, number of bonds involved in damage leading up to the onset of major damage) and hence the trends are not as obvious in strength as in the elastic modulus and failure strain. In general, the non-wovens of size 27 mm × 9 mm have a mechanical response that matches larger sized specimens, and provide useful information for non-woven micromechanics study within the areal limits of x-ray techniques.

S4. Non-woven tensile stress-strain curves in μCT experiments

The non-woven tensile stress-strain curves of all the specimens tested in the μCT experiments are shown in Figure 2.14. The sharp drops of stress at strains of 0.01, 0.02, 0.1, 0.15 and 0.3 correspond to stress relaxation before each CT scan. Note that large scale damage in the SF32 specimen occurred at a very early stage, even earlier than the SF20 specimen. This is because of the random nature of non-wovens which causes some SF32 specimens to have very weak mechanical properties. Similar mechanical behaviors of SF32 can also be found

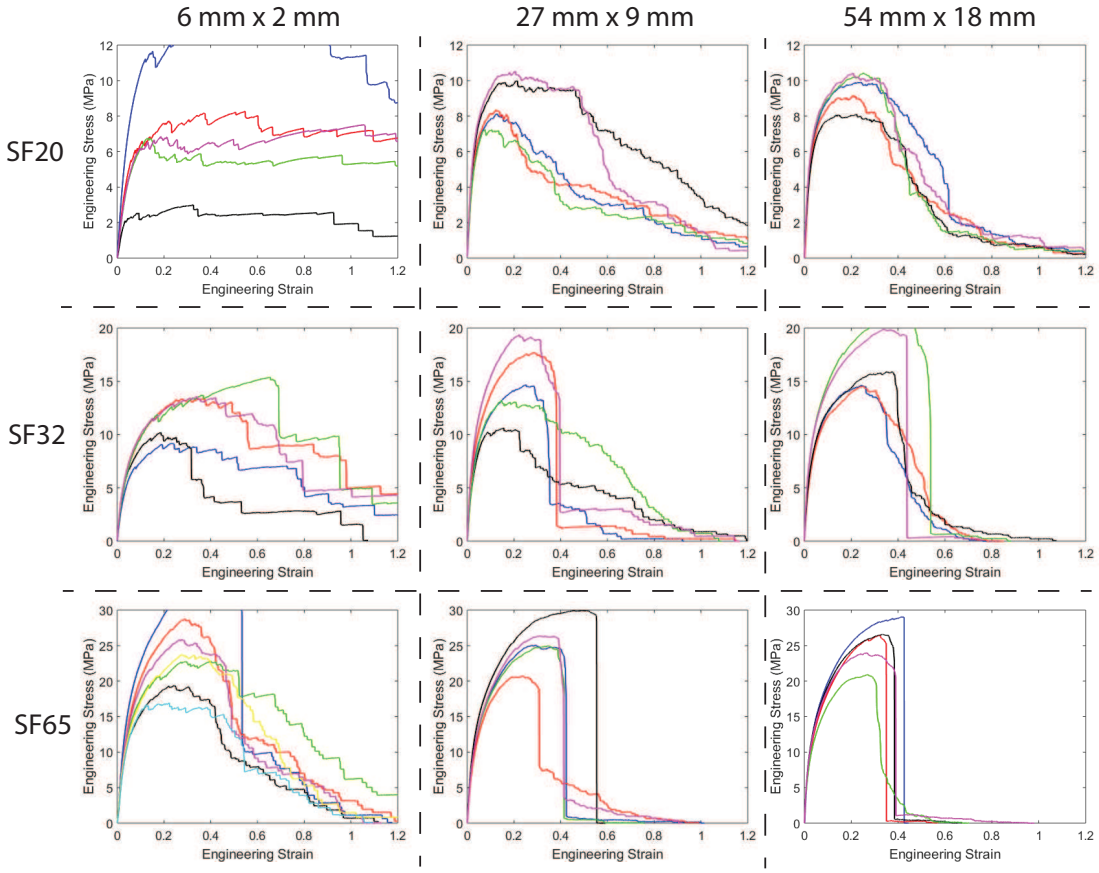

Figure 2.12: Stress-strain response of non-woven specimens of different sizes and areal weights.

in Figure 2.2b, in which the specimen with minimum strength behaves very similarly to SF20.

S5. Fiber orientation

The full fiber orientation distributions of SF20, SF32 and SF65 at four different strains are shown in Figure 2.15. In SF32 the peak of the fiber orientation distribution moved from -70° to -50° and reached 0° as the strain increased from 0 to 0.5, indicating that the fibers became more aligned with the loading axis under

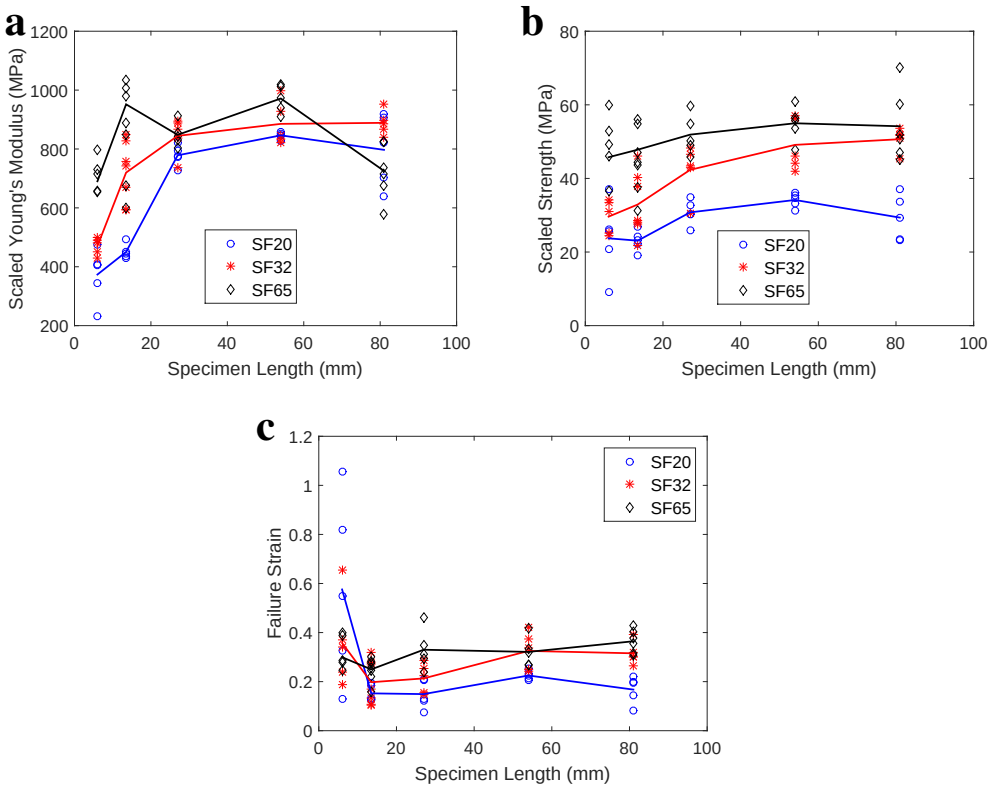

Figure 2.13: Variation in extracted material properties with specimen size while holding specimen aspect ratio constant at 3:1 length:width. (a) Scaled elastic modulus; (b) Scaled strength; (c) Failure strain. Specimens in the manuscript have a length of 27 mm.

uniaxial tensile loading. The orientation distribution peak of SF65 moved from -30° to 0°, but the change of the peak height was much less than for SF32, indicating that the reorientation process in SF65 was less significant than in SF32. Contrary to the two high areal weight materials, the change of fiber orientation in SF20 did not follow a clear trend.

The non-woven fiber orientation distribution change with affine deformation assumption was simulated with user written Matlab R2015a scripts. 2D random fiber networks were generated by randomly placing fibers with infinitesimal diameter inside a region with the same size of the beam window.

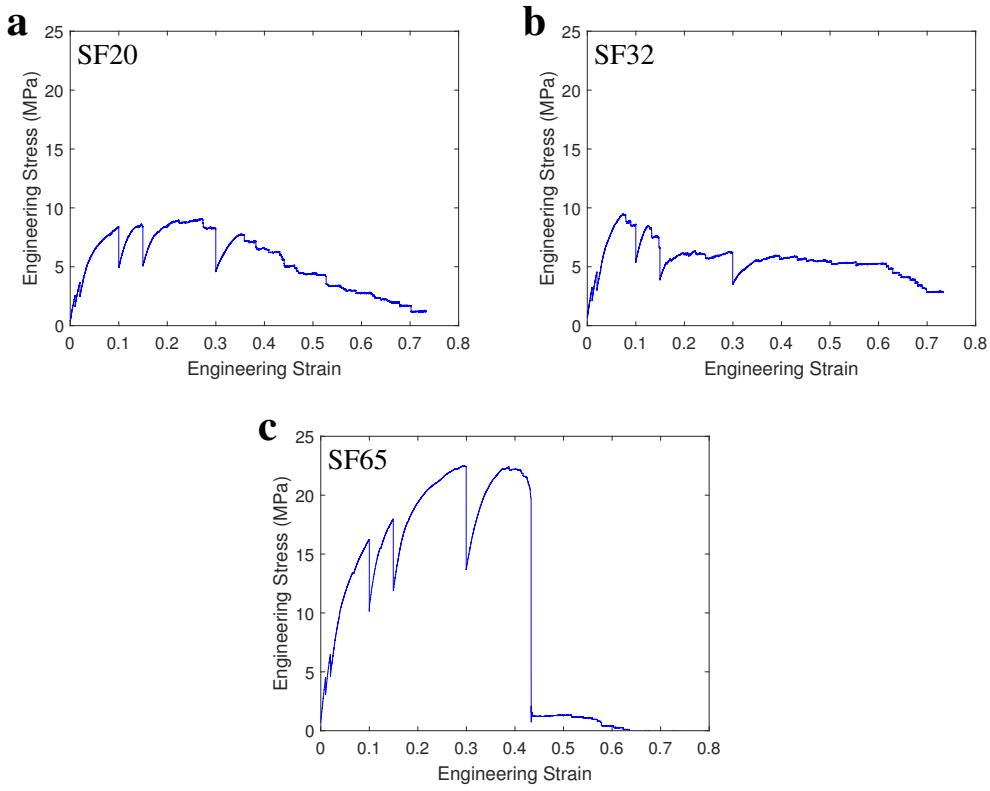

Figure 2.14: The tensile stress-strain curves of non-woven (a)SF20, (b)SF32 and (c)SF65 in the μCT experiments. The stress relaxation before each CT scan is apparent.

Initial fiber density and orientation distribution were set to be the same as the specimen used in XRD experiments. Periodic boundary conditions were then imposed in transferring fiber segments that were out of field view into the opposite side. The deformation gradient **F** was then applied to each fiber in the network assuming a Poisson's ratio of zero, with **F** defined as

$$\begin{pmatrix} 1+\epsilon & 0 & 0 \\ 0 & 1 & 0 \\ 0 & 0 & 1 \end{pmatrix}$$

where ϵ is the macroscopic strain. The orientation parameter of the deformed

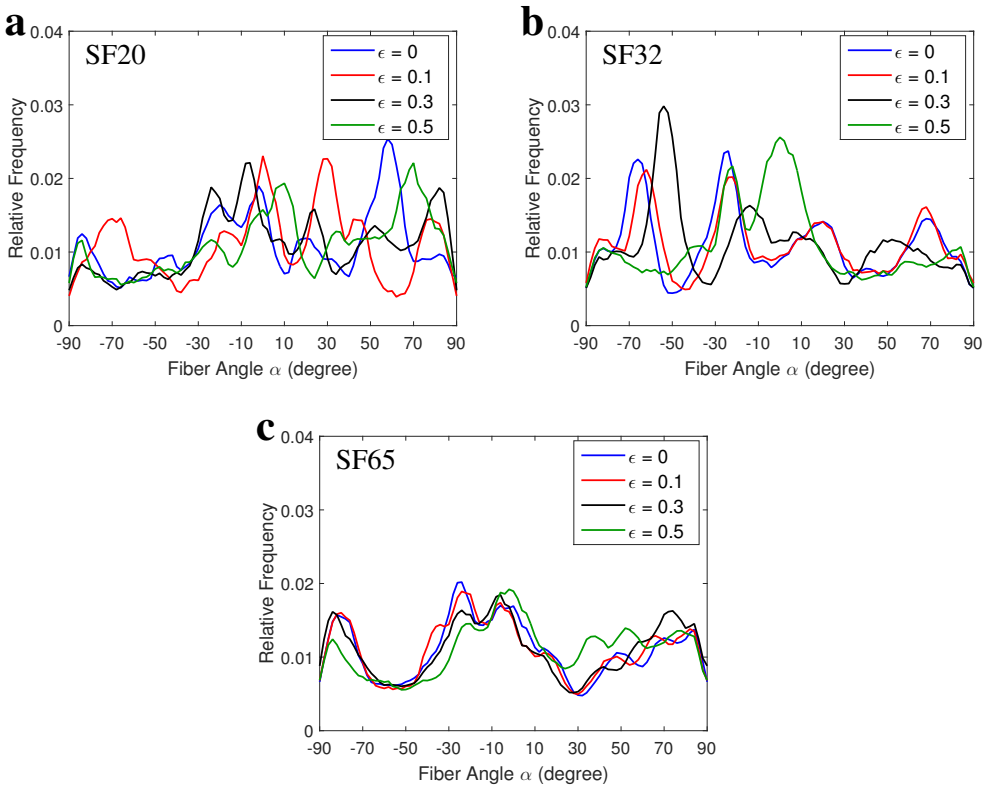

Figure 2.15: The full fiber orientation distributions (a) SF20, (b) SF32 and (c) SF65 at 4 different strains.

configurations were calculated and plotted against strain in Figure 2.16. With an affine deformation assumption, the orientation parameter increases with macroscopic strain, reaching 0.3 at a strain of 0.5. For SF20, the simulation prediction is generally in good agreement with experiment results before a strain of 0.05, but differs afterwards. For SF32 and SF65, this simulation over predicts the orientation parameter values throughout the deformation process.

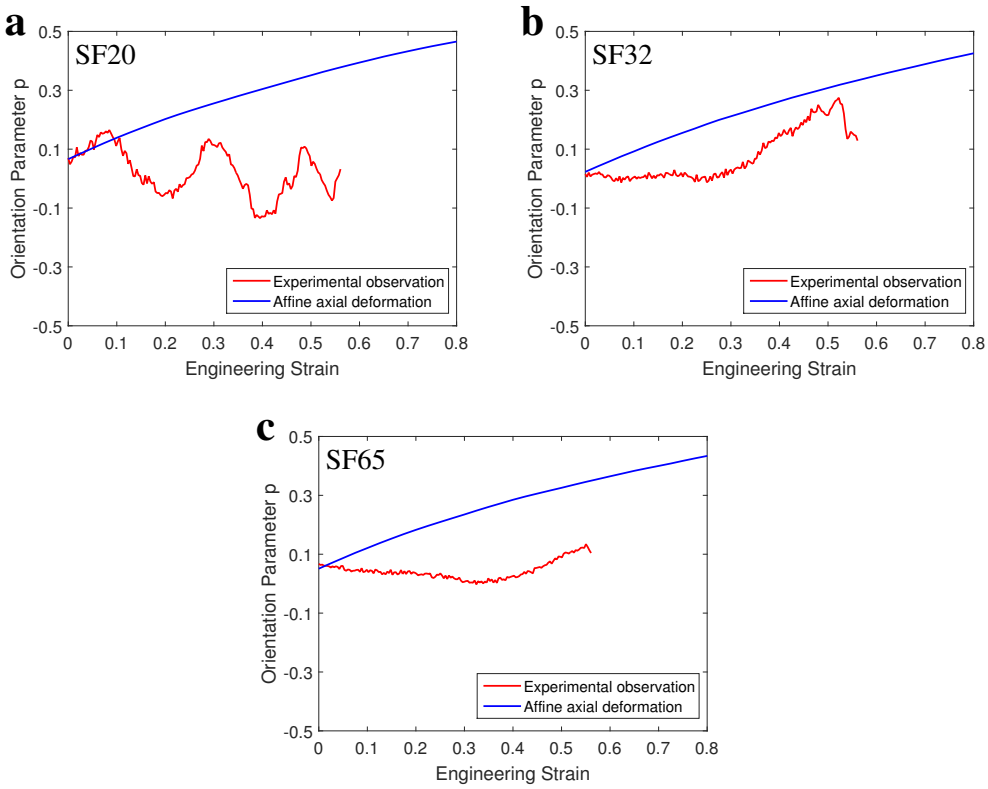

Figure 2.16: A comparison of orientation parameter change between experimental data and simulation with affine deformation assumption for (a) SF20, (b) SF32 and (c) SF65. The fiber realignment in SF32 and SF65 is less than theory prediction.

CHAPTER 3

DETERMINATION OF BOND STRENGTHS IN NON-WOVEN FABRICS: A COMBINED EXPERIMENTAL AND COMPUTATIONAL APPROACH

3.1 Introduction

Non-wovens are a material class that encompasses all fabrics not manufactured through a weaving or knitting process. A typical non-woven consists of a set of fibers consolidated by either bonding or local entanglement. The manufacturing methods for non-woven are versatile, and the product carries advantages including high porosity, high surface area, and high specific toughness. Because of these positive attributes, non-wovens are utilized in a variety of fields including energy, water purification, ballistic protection, tissue engineering and medical disposables (Ahmed et al., 2015; Liu et al., 2013; Russell, 2006; Yoon et al., 2008). Despite wide application, predicting non-woven strength and toughness remains a difficult task. The deformation process involves many micromechanical mechanisms, such as fiber stretching, fiber bending, fiber rotation and bond damage (Ridruejo et al., 2011; Silberstein et al., 2012; Chen et al., 2016b). Among these, bond damage is a major damage mechanism in many non-wovens (Ridruejo et al., 2011; Isaksson et al., 2006; Chen et al., 2016a) however, bond strength is rarely reported due to lack of an effective characterization technique. Therefore, the main objective of this work is to develop a method to determine bond strength.

For non-wovens that are bonded at fiber-fiber intersections, randomly distributed bonds connect and transmit loads between individual intersecting fibers. In the seminal work of Cox (1952), elasticity for this type of non-woven

was derived based on fiber orientation and density, but was not considered to be affected by bonds. However, later finite element simulations showed that Cox' s model neither captured local fiber loading mechanisms nor provided satisfactory predictions of macroscopic behavior (Aström et al., 1994; Räisänen et al., 1997) (especially on sparse networks). It was later found that bond density indeed affected non-woven elastic modulus. As bond density increases, fiber segment length decreases and fibers tend to deform axially rather than bending (Shahsavari and Picu, 2013a). Not only bond density but also bond properties affect non-woven mechanical behavior. Bond damage was found to be the main damage mechanism in paper and geosynthetic materials (Ridruejo et al., 2011; Isaksson et al., 2006; Chen et al., 2016a). By tuning thermal treatment time, temperature, and fiber contact force, non-wovens with different bond properties can be made. The mechanical strength of non-wovens was found to increase with increasing bond strength (Torgnysdotter et al., 2007b; Choi et al., 2004). Though the importance of bonds has been recognized, accurate bond constitutive behavior has not been used in fiber network modeling. In discrete network simulations where bonds were damageable, bonds were considered as rigid and broke in a brittle manner (Aström et al., 1994; Räisänen et al., 1997). Constitutive models incorporated bond damage by introducing a damage variable, but this damage did not have direct relationship to bond properties due to a lack of known bond properties (Ridruejo et al., 2012; Isaksson et al., 2004).

Precise characterization of bond properties is difficult, since non-wovens are composed of fibers that have diameters on the order of microns or less. Direct testing of bond mechanical behaviors has previously been performed with specially designed tensile testing apparatus or atomic force microscopes (AFM) (Torgnysdotter et al., 2007a; Schmied et al., 2012, 2013; Kulachenko and

Uesaka, 2012). In these kinds of tests, individual fiber-fiber bonds were made independently rather than extracted from a non-woven. Whether the result reflects bond properties within actual non-wovens needs further proof. Further, it has been found that bond strength within paper has great variance (Schmied et al., 2012, 2013), this is likely true for other non-wovens as well. Testing individual bonds one at a time is laborious. When only an estimate of average bonding property is needed, peel tests can be used (Koubaa and Koran, 1995; Yousefi Shivyari et al., 2016). This method provides Mode-I interlayer bonding energy in layered non-woven materials, but does not provide individual bond strength. Processing simulations on fiber pairs have been used to establish the relationship between bond formation conditions (temperature, pressure and fiber lay out) and bond properties. For example, the effect of fiber-fiber angle and degree of indentation on maximum stress in the bonding region was studied using 3D finite element simulations (Berhan and Sastry, 2003). The work of adhesion between two 'coalesed' polymeric fibers was calculated through atomic simulations (Buell et al., 2010). However, these model-prediction results have not been experimentally validated.

Here, we present a new method for characterizing fiber-fiber bond strength in non-wovens. The method is inspired by the advancement of image-based direct modeling. The method carries the dual advantages of characterizing actual bonds in a non-woven and characterizing hundreds of bonds simultaneously. The proposed method is introduced in three steps. In section 3.2, the overall scheme of the method is introduced. In section 3.3 and 3.4, the application of the method to a polypropylene non-woven is described. We used a linear irreversible interface law to describe debonding behavior and the model parameters were determined through an optimization process. This interface law has

four parameters: normal stiffness k, shear stiffness βk, separation at the start of damage d_1, and separation at total loss of bond stiffness d_2. In section 3.5, we present two independent validations of the obtained bond strengths.

3.2 Bond strength determination procedure

The bond strength determination method proposed in this chapter has three ingredients: imaging non-woven microstructure, characterizing mechanical properties, and direct simulation of the force response of specimen microstructure to deformation. The overall procedure is shown in Fig 3.1. The first step is to image a small specimen with a 3D imaging technique such as micro computed tomography (μCT) or confocal microscopy. This 3D imaging is required to determine fiber arrangement and resolve bonding sites. The size of the specimen should be sufficiently large for the contained bonds to be a representative subset of bonds in a bulk material (> 100 bonds), and sufficiently small to manage imaging and computational cost. After the imaging step, the stress-strain response of this specimen and its constituent fibers are characterized under uniaxial tension. Next, a digital replica of this specimen is extracted from the 3D image. The replica is then discretized and imported into a finite element framework, in which fibers and bonds are explicitly modeled. The fiber stress-strain constitutive behavior is taken directly from single fiber experimental results. Structural elements should be used to model the fibers so that computational efficiency can be improved. A constitutive law has to be chosen to model bond behavior under deformation. The unknown parameters in the constitutive law are estimated through fitting the FEA simulated uniaxial tensile test to the experimental stress-strain results for that specimen. After the model parameters

are estimated, bond mechanical properties, like stiffness and strength, can be determined accordingly.

The meso-scale specimen avoids the drawbacks of both component level analysis and continuum level analysis. Local bonding conditions and bond properties usually have great variance, which means getting statistical information of bond properties through individual bond testing is cumbersome. Conversely, within a homogenized framework, resolving bond damage from other irreversible mechanisms, like fiber plasticity and fiber fracture, is challenging. The potential application of this proposed method is broad. It can be applied to any fiber network that is bonded at fiber-fiber intersections (e.g. geosynthetics, paper, electrospun mats) for which damage under macroscopic deformation is a concern.

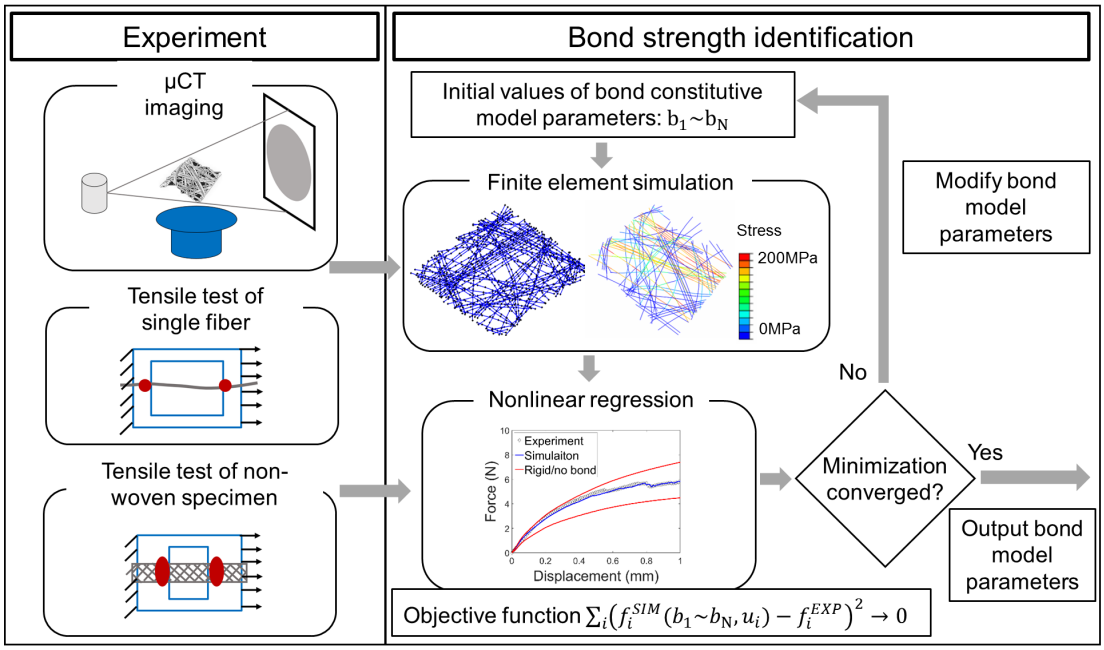

Figure 3.1: Procedure for proposed bond strength determination method.

3.3 Materials and methods

3.3.1 Materials

The method introduced in the previous section is demonstrated here for the Dupont Typar geotextile SF20. This non-woven is composed of polypropylene fibers 40 μm-60 μm in diameter. During the manufacturing process fibers are first laid down on a flat surface and then bonded through application of both heat and mechanical pressure. SEM (scanning electron microscope) images of this material are shown in Figure 3.2. Fibers are deformed and partially fused at each bonding site.

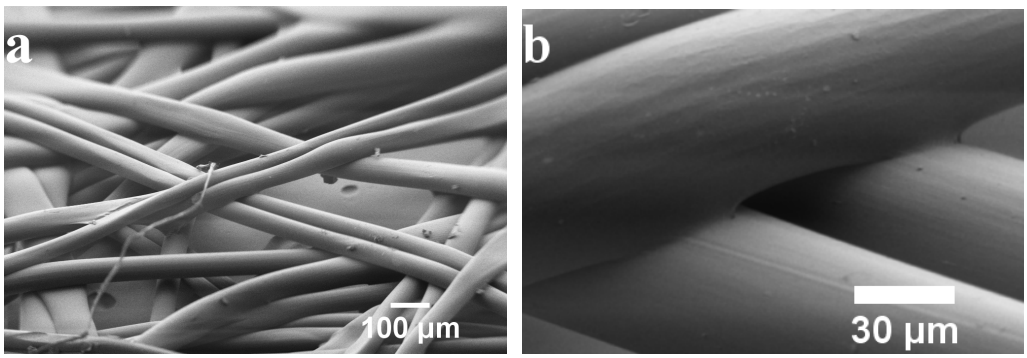

Figure 3.2: SEM images of the non-woven SF20 showing (a) the network morphology, (b) an enlarged view of the bonding region located in the center of (a)

The mechanical properties of the Typar SF series of non-woven have previously been characterized in detail (Ridruejo et al., 2011; Chen et al., 2016a). For convenience, the uniaxial tensile and cyclic behavior of SF20 and the constituent fiber are included as Figure 3.3. Also, some key observations from the literature are summarized in the following:

- Tensile stress-strain curve of this non-woven exhibits an elastic region, a roll over yield region and a highly damaged softening region (long tail) after the peak load. The mechanical properties are summarized in Table 3.1(Chen et al., 2016a).
- Non-woven mechanical behavior has significant specimen to specimen variantion (Ridruejo et al., 2011; Chen et al., 2016a).
- The constituent fiber is elastic-visco-plastic. Under tension, the fiber has a short elastic region that transitions into a plastic hardening regime. The mechanical properties are summarized in Table 3.1 (Chen et al., 2016a).
- In cyclic testing, the non-woven modulus at the beginning of each unloading step decreases with deformation, while fiber modulus remains the same. Both fiber fracture and bond fracture contribute to this modulus decrease (Chen et al., 2016a).
- Bond damage in the non-woven is observed starting at small strains (2.5% nominal strain) (Ridruejo et al., 2011; Chen et al., 2016a).

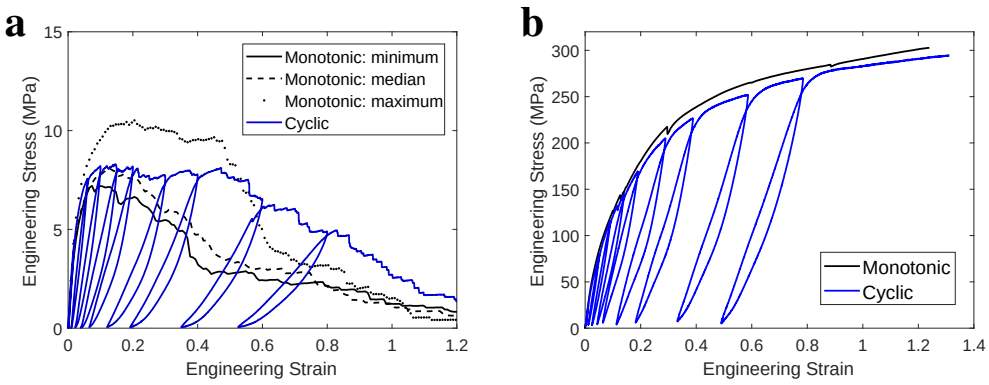

Figure 3.3: (a) Uniaxial tensile behavior of non-woven SF20, (b) uniaxial tensile behavior of constituent fiber. "Reprinted from (Chen et al., 2016a), Copyright (2016), with permission from Elsevier."

Table 3.1: Mechanical properties of constituent fibers and non-woven under uniaxial tensile loading.

Material	Young's modulus (GPa)	Tensile strength (MPa)	Failure strain
Fiber	2.45 ± 0.15	293 ± 8	1.3 ± 0.3
Non-woven	0.22 ± 0.02	8.8 ± 1.4	0.15 ± 0.06

3.3.2 Methods

Following the general procedure described in Section 3.2, a 2 mm wide non-woven SF20 strip was cut from a bulk sheet and glued (Loctite Plastics Bonding System) to a sample holder spanning across a 2 mm gage length. Within the gage section, there were approximately 500 bonds. The specimens were imaged with a commercial CT (Xradia/Zeiss XRM-520 Versa) with voxel side length set to 3.6 μm. The specimen was then tested under uniaxial tensile loading while the load displacement curve was recorded. The crosshead speed was set to 0.1 mm/min. All specimens were examined before and after testing under an optical microscope (Olympus BH-2) and results from any specimens that showed evidence of fiber slippage from the grip region were discarded.

The μCT 3D image of each specimen was converted into an FEA representation. The microstructure was skeletonized using software FNXCT (Wernersson et al., 2014). This software connects several seed points (manually provided) of one fiber with a third order polynomial curve to represent the centerline of this fiber. After the centerlines of each fiber were determined, a bonding site was introduced at a fiber-fiber intersection if the minimum distance between the two fibers was smaller than the sum of their radii. The bond area A was calculated

using the non-adhesive elastic contact solution (Popov, 2010)

$$A = \pi \sqrt{R_1 R_2} d \tag{3.1}$$

where R_1, R_2 are fiber radii, $d = (R_1 + R_2 - d_s)$ is the indentation distance and d_s is fiber spacing. The skeletonized fiber network was further discretized into 1D structural elements and then imported into the FE software Abaqus (Figure 3.4a). The Timoshenko shear flexible beam element (B31) was chosen to mesh fibers due to a relatively short fiber length to diameter ratio (≈ 5). Bonds were modeled by a connector element (CONN3D2), which constitutively defines the interaction between two bonding nodes. Abaqus explicit was used to solve the load-displacement response of the model. All FE simulations were conducted on a desktop with a quad core i7 processor.

Fiber diameters were determined iteratively through image processing and network simulation. An image thresholding step was first applied on the greyscale μCT image to convert it to a binary image. Radius of a fiber was then measured as the distance from the fiber centerline to the background. All the diameters were measured automatically with image threshold value as the only input. The image threshold value was chosen so that the simulation elastic modulus matches that from the corresponding experiment. Bond locations and areas were updated following adjustment of the image threshold.

We used Ortiz' s interfacial cohesive law (Ortiz and Pandolfi, 1999) to describe bond behavior. This law was chosen because of its generality for describing irreversible interface bonding behavior. Bond properties of a cellulose fiber network determined by AFM have also been shown to fit this law (Kulachenko and Uesaka, 2012). The constitutive equation utilizes four parameters: k, β, d_1 and d_2. k is bond elastic modulus in normal direction. β describes the relative

stiffness of shear deformation to normal deformation. d_1 is the critical distance when damage initiates. d_2 is the critical distance when full separation occurs. Interfacial effective displacement is defined as $\Delta_{eff} = \sqrt{\Delta_n^2 + (\beta\Delta_s)^2}$, where Δ_n is normal displacement and Δ_s is shear displacement (Bower, 2009). Bond behavior is linear elastic when $\Delta_{eff} \leqslant d_1$, and bond elastic modulus linearly degrades when $d_1 \leqslant \Delta_{eff} \leqslant d_2$. The load displacement response of a bond under normal separation is shown in Figure 3.4b. Bond strengths in pure normal and pure shear deformation mode are calculated as $\sigma_{normal} = k \times d_1$ and $\sigma_{shear} = \beta \times k \times d_1$, respectively.

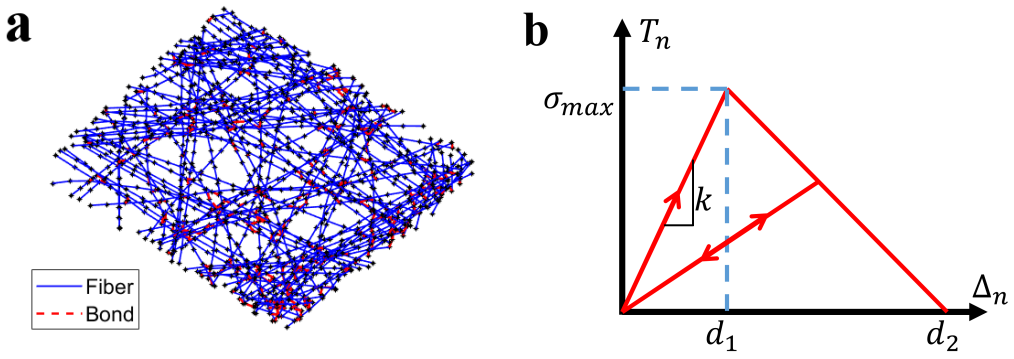

Figure 3.4: (a) Representative finite element mesh of a specimen. Beam elements are marked as blue lines, bond elements are marked as red lines, nodes are marked as black asterisks. (b) Constitutive behavior of a bond deforming under pure tension. Line with double arrows indicates unloading/reloading path for this bond model.

The parameters in the bond model were determined by fitting the FE simulated uniaxial tensile response to experimental data. The nonlinear regression problem was solved in the least-square sense where the L^2 norm of the residual is minimized. Here, residual $\boldsymbol{r}$ describes the difference between simulated force response $\boldsymbol{f}^{sim}$ and experimental force response $\boldsymbol{f}^{exp}$ at each data point:

$$\boldsymbol{r}(\boldsymbol{b}) = \{\boldsymbol{f}^{sim}(\boldsymbol{b}) - \boldsymbol{f}^{exp}\} \in \mathbb{R}^{N_D}, \tag{3.2}$$

where $\boldsymbol{b}$ is a vector of bond parameters $\{k, \beta, d_1, d_2\}$ and N_D is the number of data points. The regression problem is stated (considering the positiveness of bond parameters) as:

$$\text{minimize} \qquad g(\boldsymbol{b}) = \frac{1}{2}\|\boldsymbol{r}(\boldsymbol{b})\|_{L_2} = \frac{1}{2}\boldsymbol{r}^T(\boldsymbol{b})\boldsymbol{r}(\boldsymbol{b}) \tag{3.3}$$

$$\text{subject to} \qquad b_i > 0 \tag{3.4}$$

The objective function $g(\boldsymbol{b})$ is non-smooth due to bond damage along the deformation process. A downhill simplex algorithm (Nelder and Mead, 1965) was used to solve the optimization problem, since a gradient based optimization algorithm would suffer from convergence issues. A simplex is a polytope with $N+1$ vertices in an N dimensional optimization problem. The downhill simplex algorithm starts with constructing a simplex around the initial guess and then takes a series of steps to change simplex shape and move it along the N dimensional topography until it reaches a minima. The direction of simplex shape change depends solely on function evaluations at each vertex. In the present study the downhill simplex method converged in around 15 steps.

3.4 Results

3.4.1 Network microstructure statistics

The microstructure statistics corresponding to six specimens are listed in Table 3.2. Due to the small specimen size the specimen microstructure (arrangement of fibers and bonds) varies significantly. Fiber number ranges from 90 to 138 and total fiber length ranges from 170 mm to 281 mm. These ranges are

self-consistent since fibers are long and should span across the 2 mm specimen region in this non-woven. The number of bonds ranges from 305 to 1026. In plane fiber orientation distribution can be described by an orientation parameter p (Chen et al., 2016a), which is defined as: $p = 2\langle\cos^2\alpha\rangle - 1$, where α is the angle between the fiber axis and the direction of applied strain. This parameter varies from -1 to 1 and equals 0 for a set of fibers randomly oriented in plane. The orientation parameter of the six specimens ranges from -0.19 to 0.23, indicating a nearly uniform fiber orientation distribution. The bond area distribution is shown in Figure 3.5, this distribution is skewed towards small bonding area. The variation in bond area distribution, fiber segment number, and fiber orientation distribution indicates that each specimen has a unique fiber layout and therefore load transmission path. Consequently, the bond strength identification is evaluated by consistency of the bond model parameters estimated from these six different specimens.

Table 3.2: Microstructure statistics and mechanical properties of six tested non-woven specimens.

	Number of fibers	Total fiber length [mm]	Number of bonds	Orientation parameter	Stiffness [N/mm]	Peak load [N]
Specimen 1	106	206	566	−0.055	21.6	8.7
Specimen 2	97	180	629	0.23	23.4	7.0
Specimen 3	138	281	503	0.14	19.4	9.6
Specimen 4	90	170	338	−0.14	16.5	5.9
Specimen 5	130	242	1026	−0.19	22.6	6.1
Specimen 6	107	206	305	0.23	22.7	8.9

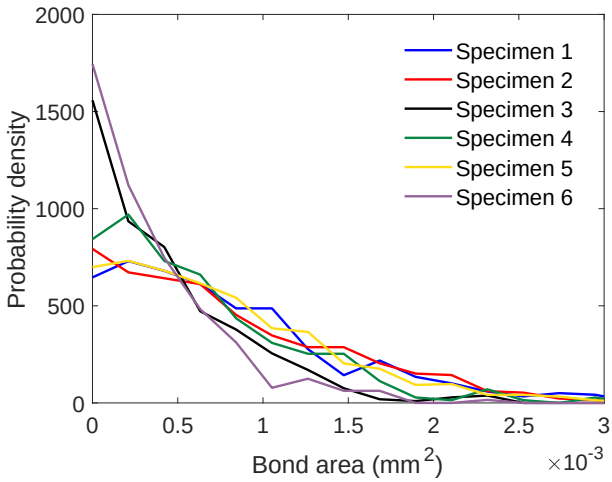

Figure 3.5: Bond area distribution within tested specimens.

3.4.2 Model parameter study

The bond model has four parameters: k, β, d_1, d_2. The value ranges of the four parameters that define the bond constitutive behavior can be estimated based on the physical meaning of each. Since bonds are formed from two fibers, the bond elastic stiffness k should be of the same order as the fibers. If the bond elastic modulus has the same value as its constituent fibers then $k = E_f/l_{ch}$. Fiber modulus is $E_f = 2.4$ GPa. The characteristic length scale l_{ch} is taken as the average fiber-fiber spacing d_s at a bonding site, $l_{ch} \approx 30$ μm. So $k = 80$ MPa/μm. β controls the relative stiffness between shear deformation and normal deformation. Based on the suggestions in Bower (2009), β is typically below 1. Here, we take $\beta = 0.7$ as a reference for the parameter study. d_1 and d_2 describe the displacement between ends of the bond connector element and therefore should be on the scale of microns.

Comparing with the reference case ($k = 80$ MPa/μm, $\beta = 0.7$, $d_1 = 3\mu$m, $d_2 = 3\mu$m), each of the four parameters was modified by a factor of two to

see its effects on macroscopic behavior and damage progression (Figure 3.6). Prior to damage, the simulated curves fall on the rigid bond line for both $k = 80$ MPa/μm and $k = 160$ MPa/μm cases indicating that network elastic stiffness is minimally influenced by bond stiffness. This lack of dependence on bond stiffness has also been observed in literature (Räisänen et al., 1997). When bond damage is considered, parameters d_1 and d_2 come into play. Bond strength σ_{normal} and σ_{shear} are both proportional to $k \times d_1$. For high $k \times d_1$ cases, bonds are stronger, fewer bonds are broken during the tests, and more fibers participate in load carrying (Figure 3.6a-b). Systematic variations in k or d_1 reveal that the model is sensitive to σ_{normal} rather than k and d_1 independently. The effects of β and d_2 are shown in Figure 3.6c-d. Similarly to σ_{normal}, higher β results in higher force response and less bond damage inside the network. However, the effect of β is less significant than σ_{normal} when they are changed by same percent. The model response is not sensitive to d_2, so in later sections d_2 is set equal to d_1.

3.4.3 Bond strength estimation

The experimental and simulation load displacement curves of six tested specimens are shown in Figure 3.7. All the curves have a linear region, a smooth roll-over region and then a kinked region starting at displacement ≈ 0.4 mm. These kinks come from bond fracture and associated fiber stress relaxation. Occasionally, a large number of bonds broke within a short period of time and caused a big force drop. Comparing Figure 3.3a and Figure 3.7a, it should be noted that the load displacement curve of the 2 mm $\times$ 2 mm specimens are jagged compared to larger specimens. This indicates that damage in larger size specimens is distributed while damage in small specimen is more localized and

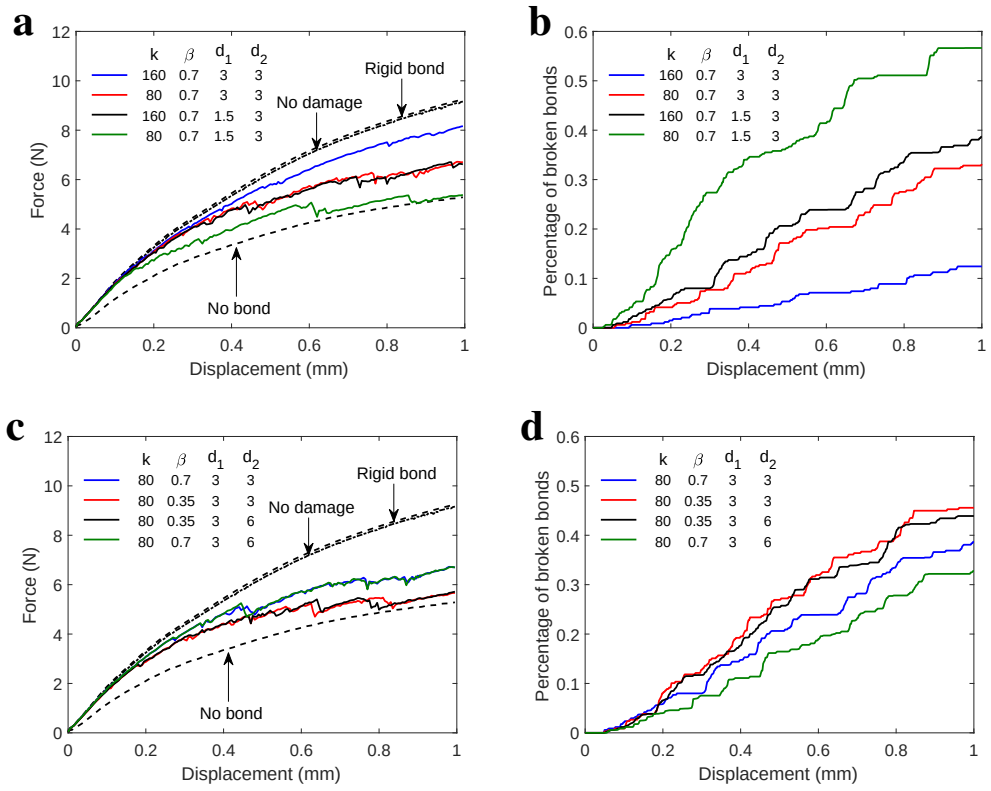

Figure 3.6: (a) Load displacement curves for parameter study of k and d_1, and (b) corresponding damage progression curves. (c) Load displacement curves for parameter study of β and d_2, and (d) corresponding damage progression curves.

apparent even before the peak load (a more detailed discussion of size effects on mechanical behaviors of this material is included in Chapter 2 supplementary material 2.5). These smaller specimens are therefore better for extracting bond parameters. The six tested specimens have distinct microstructures and correspondingly their load-displacement curves vary significantly from each other. Specimens 1, 2, 5 and 6 have similar elastic moduli even though their total fiber lengths ($\propto$ areal weight) are different. Specimen 3 has higher total fiber length but its elastic modulus is lower. Specimen 4 has the lowest fiber length and elastic modulus. From this data it is apparent that different network microstructures have different load transmission paths and different bond break-

ing sequences. A discrete network model that captures the specific network microstructure has the advantage of simulating real damage progression within different specimens.

For each specimen, we solved a nonlinear least square problem (equations 3 to 4) to obtain bond parameters β and d_1. The bond model estimation results are shown in Figure 3.7 and Table 3.3. Individual fitting results show that the model captures the roll-over yield region and major kinks on the load displacement curve. Residual $\boldsymbol{r}$ versus displacement is overlaid on Figure 3.7 as well. In specimens 1, 3, 4 and 6, the residual is small indicating a good fit. In the other specimens, the residual is continuously positive in one region and negative in another. This indicates that model overestimates bond strength in one region and underestimates it in another. One possible reason for this error is the assumption we made that bond strength is proportional to bond area however, the bonding nature may be more complicated. While a more complex bond model could be used, a strong physical basis would be needed to avoid over fitting. Table 3.3 lists estimated bond normal strength and shear strength. Calculating the mean and standard deviation of bond strengths in the six specimens, we have $\sigma_{normal} = (1.3 \pm 0.3) \times 10^2$ MPa, and $\sigma_{shear} = (1.0 \pm 0.2) \times 10^2$ MPa. Specimens 2 and 5 have poorer fit and much lower bond strength than the other specimens. Both of these specimens have less hardening at finite strains. While this reduced hardening is most likely a reflection of low bond strength, it could also have a contribution from small slipping of the fibers at the grip that was not evident within optical microscopy.

Cross validation evaluates how fitted model parameters can be generalized to a new data set. In this work, each of the six tested specimens represents an

Table 3.3: Mean bond strength for each non-woven specimen and goodness of fit for individual optimization and cross-validation.

	Normal strength σ_{normal} [MPa]	Shear strength σ_{shear} [MPa]	Individual fit R^2	Cross validation R^2
Specimen 1	170	133	0.9894	0.8832
Specimen 2	89	72	0.9568	0.8550
Specimen 3	147	98	0.9939	0.9909
Specimen 4	133	97	0.9894	0.9548
Specimen 5	116	72	0.9611	0.8084
Specimen 6	140	112	0.9795	0.9639

independent data set due to its unique network microstructure. We performed leave-one-out cross validation on each individual data set, using five data sets for training to get model parameters and then testing the fidelity of obtained model parameters on the left out data set. This process was repeated until all data sets had been left out once. Table 3.3 shows the cross validation results. Full fit and residual plots are provided in appendix (section 3.7). All validation simulations have reasonably good agreement with experimental data, showing the predictive power of the obtained bond model parameters. Not surprisingly, specimens 2 and 5 have the worst fits since their independent fitted bond strengths are lower than the other specimens.

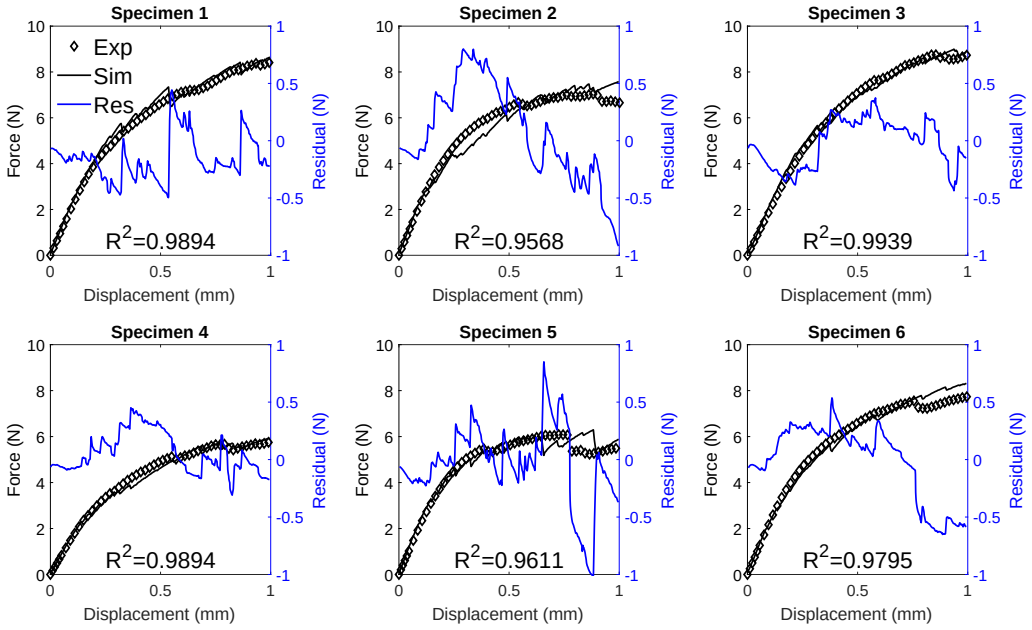

Figure 3.7: Uniaxial tensile response (diamond markers) of six tested non-woven specimens. FE simulation results (solid black line) with estimated bond model are overlaid on the experimental curves. The residual (solid blue line) and goodness of fit (R^2 value) are also reported in each subplot.

3.5 Bond model validation

3.5.1 Larger size specimen validation

Macroscopic damage in non-wovens can be quantitatively characterized by cyclic tests. The slope at the beginning of each unloading step decreases with deformation due to a loss of network connectivity caused by bond fracture (Ridruejo et al., 2011; Chen et al., 2016a). This observation provides a way to test the validity of bond strength values obtained in the previous section. We performed cyclic tests on 6 mm × 6 mm non-woven specimens and FE simula-

tions of the same size artificial random fiber network (RFN). The size of 6 mm $\times$ 6 mm is chosen because at this larger size the response is reasonably insensitive to the specific microstructure and the FE simulation can be done in a timely manner on a typical desktop. The method and result of the validation approach are discussed in this section.

Methods: In the cyclic experiment, a non-woven specimen was stretched to a certain strain and then unloaded to zero force and reloaded again. The displacements at the start of each unloading step were 0.12 mm, 0.36 mm, 0.6 mm, 0.9 mm, 1.2 mm, 1.8 mm, 2.4 mm, 3.6 mm, 4.8 mm, and both load and unload speeds were set to 0.0353 mm/s. A total of five specimens were tested. The computational work started by a RFN generation step. The generation algorithm first generated random seeds within the specimen domain (6 mm $\times$ 6 mm $\times$ 0.3 mm). A straight fiber was then extended from each seed point to the boundaries of the domain. The fiber was assumed to have uniform in-plane angle (randomly drawn from a uniform distribution of 0^o to 180^o), and a slight out of plane angle (randomly drawn from a normal distribution of 0^o to 3^o). Fiber diameter and network density were set to the same as μCT measurement and the network generation step was stopped when the network density reached target value (43 mm/mm^2 from Table 3.2). After all fibers were generated, bonding sites were located and bond areas were calculated following the same procedure as described in section 3.3.2. Since the fiber generation step did not prevent fibers from passing through each other, bond area distribution in the RFN is different from the real material (Fig 3.5). The location of each bonding sites was adjusted along the bond vector so that bond area distribution matches experimental data. The generated RFN was further discretized and imported

into the finite element framework and simulated with unloading at the same displacements as the cyclic experiment.

Results: One representative cyclic test result is shown in Figure 3.8a. The specimen reaches peak load at a displacement of 2 mm and then the force decreases. We measured unloading slopes at the beginning of each unloading step (Figure 3.8b). The unloading slope slightly increases at small strains possibly due to fiber alignment and then the unloading modulus drops because of bond damage. One representative simulation load-displacement curve is overlaid on Figure 3.8a. The simulation result captures the reload to the stress at which unloading started. In the simulation no damage was observed during unloading, so the duration of the unloading step is not important. Since the artificial network is not a replica of specimen geometry, the exact force response is different from the experiment. Figure 3.8b shows that the simulation unloading slope reduction with increasing displacement has good agreement with experiment, thereby showing that the obtained bond model results can be applied on larger size specimens. The mismatch at finite strains comes from either geometry simplification of RFN or potential fiber fracture in experiment. We found that increasing fiber out-of-plane angles would give a better match of damage progressions. But in this case, many fiber ends were landed on RFN surfaces instead of edges which was not observed in a real non-woven specimen. So the current out-of-plane angle distribution was adopted. It should be noted that no fitting parameters are included in these artificial network simulations.

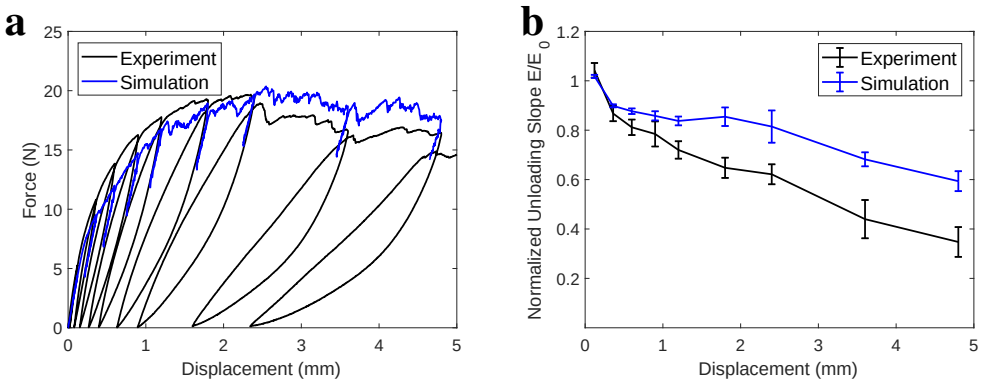

Figure 3.8: Bond strength values are tested on large size network simulations under cyclic loading. (a) Load displacement curves of a representative experiment and a representative artificial network simulation for a 6 mm × 6 mm specimen. (b) Unloading slope normalized by initial elastic modulus. The mean and standard deviation of five experimentally tested specimens and random network simulations are shown.

3.5.2 Peel tests

Peel testing provides a way to experimentally characterize average non-woven bonding energy. As shown in Figure 3.4a and Chen et al. (2016a), fibers in the non-woven SF20 are overlaid on each other forming a multi-layered structure. The ply adhesion energy can be estimated as the total work needed to break all the bonds between the two adjacent layers. The number of bonds within one layer can be obtained from μCT images. Therefore, energy dissipation per bond broken can be approximated by dividing the ply adhesion energy by the number of bonds between two adjacent layers. A similar approach has been applied for paper (Koubaa and Koran, 1995; Yousefi Shivyari et al., 2016). Assuming normal separation, the expected energy dissipation per bond can be estimated from the obtained bond model parameters (see appendix, section 3.7). We used this method to verify the bond strength values obtained with our image based modeling method.

A T-shaped specimen was adopted for the peel test (Fig 3.9). The specimen was made by putting two pieces of adhesive tape on opposite sides of a 20 mm × 100 mm piece of SF20 to form a sandwich structure. Each adhesive tape extended beyond the non-woven and was attached to a cardboard tab for clamping. In the test, the lower cardboard tab was fixed and the upper tab was pulled at a constant speed of 0.5 mm/s. The peel force reached a peak at the beginning of a test and then oscillated within a small range, indicating static peeling (Fig 3.10). The non-woven specimen was fractured along a crack plane and separated into two thinner pieces. If the crack propagation direction deviated from initial interface plane, the data of the specimen was discarded. Since both adhesive tape and non-woven are thin (less than 1 mm), the elastic energy of bending was ignored in the data analysis. Most of the external work in the peel test was supplied to separating bonded layers.

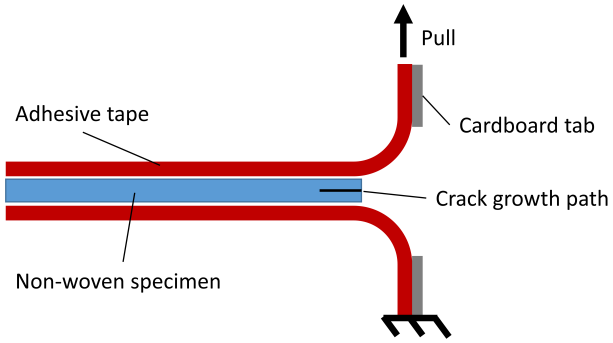

Figure 3.9: Schematic of the specimen used for peel tests. Two adhesive tapes were attached on a non-woven specimen and the tail of each adhesive tape was attached to a cardboard tab for clamping. The crack grew in the middle of the non-woven specimen during peeling, leading to separation of layers.

Five specimens were tested. Three representative load-displacement curves are shown in Figure 3.10. The mechanical work needed for separating two adjacent layers (ply adhesion energy) of these five specimens is 0.12 ± 0.01 kJ/m^2.

Since it is observed in the μCT data that the number of bonds per mm^2 is 120 ± 50 and the number of layers is ≈ 7, the bond number density between two adjacent layers in a T-peel specimen is ≈ 20 per mm^2. The energy dissipation per bond broken is determined by dividing ply energy by total number of bonds between two adjacent layers, and reads $(5.8 \pm 0.3)\mu$J. The energy dissipation per bond broken can also be estimated using the obtained bond strength values from the proposed method (Table 3.3). When a bond is broken in the peel test, energy is dissipated through the separation of two bonding surfaces and the relaxation of the fibers connected to this bond. Assuming all bonds are broken under mode-I loading, energy dissipation per bond broken is calculated as $(1.8 \pm 0.8)\mu$J (see appendix, section 3.7). This value has the same order of magnitude as the one obtained in the peel test, validating the proposed method. Bond strength is likely overestimated in the peel tests because we ignored the energy dissipation away from the fiber-fiber interface. It should also be pointed out that since the exact number of broken bonds on the crack face is unknown, peel tests can only provide a rough estimation of average bond energy.

3.6 Conclusion

In this chapter, we introduce a new method that uses a combination of experimental work and imaged-based modeling to characterize bond properties in non-woven fabrics. In the experimental portion, a non-woven specimen is imaged and then loaded for mechanical characterization. In the computational portion, the undeformed specimen microstructure is discretized and imported into a finite element framework. Since both fibers and bonds are explicitly represented in the finite element model, bond properties can be determined by solv-

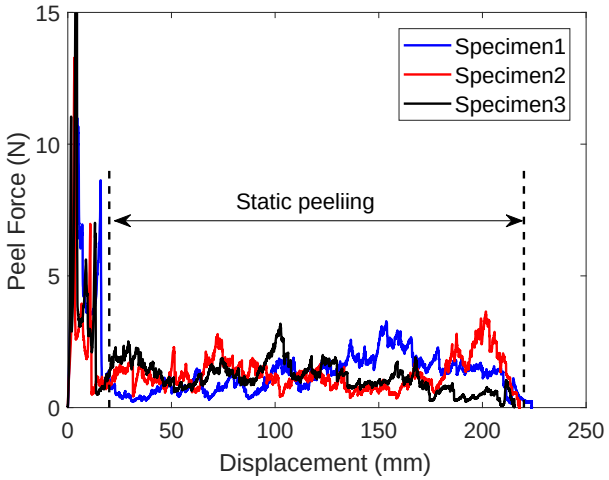

Figure 3.10: Peel test force - displacement curves of three representative specimens. The static peeling region used for the bond energy calculation is indicated.

ing the inverse problem of matching simulated mechanical response to experimental data. We demonstrate the application of this method to a commercial polypropylene non-woven. A bilinear irreversible interfacial law was used to constitutively prescribe bond behavior, and the parameters in this bond model were estimated for each tested non-woven specimen. A cross validation procedure showed that the estimated model parameters can be applied to new data sets to predict non-woven uniaxial tensile behaviors. Simulations of artificial networks showed that the estimated bond strengths can give accurate predictions of damage progression in larger size non-woven specimens. Single bond energy was also confirmed by peel tests, which provided an average interlayer bonding energy measurement.

The proposed method provides a feasible way to characterize a large number of bonds in non-wovens that are bonded at fiber-fiber intersections. The framework of using image based model to identify component behavior can also be applied to other 3D structural materials as well. The measured bond properties

will also serve as good resources for building constitutive models in the future.

3.7 Appendix

Appendix A: Fitted bond parameters

The bond parameter estimation results of individual fitting and cross validation are shown in Table 3.4. The obtained values have good consistency among tested specimens. Figure 3.11 shows the cross validation results. The finite element simulation captures the overall trend of the experimental load-displacement curve, even though the optimization process does not use the experimental data of that specimen. Iterations 2 and 5 have higher simulation force responses than experiments, while the other four iterations show the opposite behavior. This difference is because both specimen 2 and 5 have relatively low bond strength values when fitted independently (Table 3.3), so they lower the bond strength estimations in the cross validation step when one iteration takes them as part of the training set. As mentioned in the earlier text, specimen 2 and 5 are suspectable of fiber slippage and hence underestimating bond strength values. This may be the reason for the mismatch of simulation and experimental load-displacement curve in this cross validation step.

Appendix B: Peel test analysis

Figure 3.12 shows a simplified loading scenario at the crack tip in a peel test. One bond is connected to four fiber segments and each fiber segment is con-

Table 3.4: Optimization results for individual fit and cross-validation.

Individual fit			Cross validation		
Specimen number	β	d_1 [μm]	Left-out specimen	β	d_1 [μm]
1	0.782	2.12	1	0.795	1.43
2	0.811	1.11	2	0.593	1.82
3	0.665	1.83	3	0.891	1.34
4	0.734	1.66	4	0.695	1.52
5	0.615	1.46	5	0.656	1.63
6	0.801	1.75	6	0.731	1.48

nected to the rest of non-woven network structure. When a bond is taking up load, two fiber segments are under tension. When a bond is broken, the total energy dissipation (U_{total}) comes from the energy to separate bonded interfaces (U_b) and the relaxation of strain energy in fibers connected to this bond (U_f).

$$U_{total} = U_b + U_f \tag{3.5}$$

Assuming normal bond separation, U_b can be calculated using the cohesive zone model parameters (Table 3.4):

$$U_b = \frac{1}{2} \times \sigma_{normal} \times A \times d_1 = (0.10 \pm 0.03)\mu\ J \tag{3.6}$$

where A is the bond area.

U_f is the strain energy stored in the two stretched fibers. It is assumed that the stretched fibers are aligned with the loading direction and U_f can be calculated as:

$$U_f = \frac{(\sigma_{normal} \times\ A)^2 \times\ L_{seg}}{E \times\ \pi\ R^2} = (1.7 \pm 0.8)\mu\ J \tag{3.7}$$

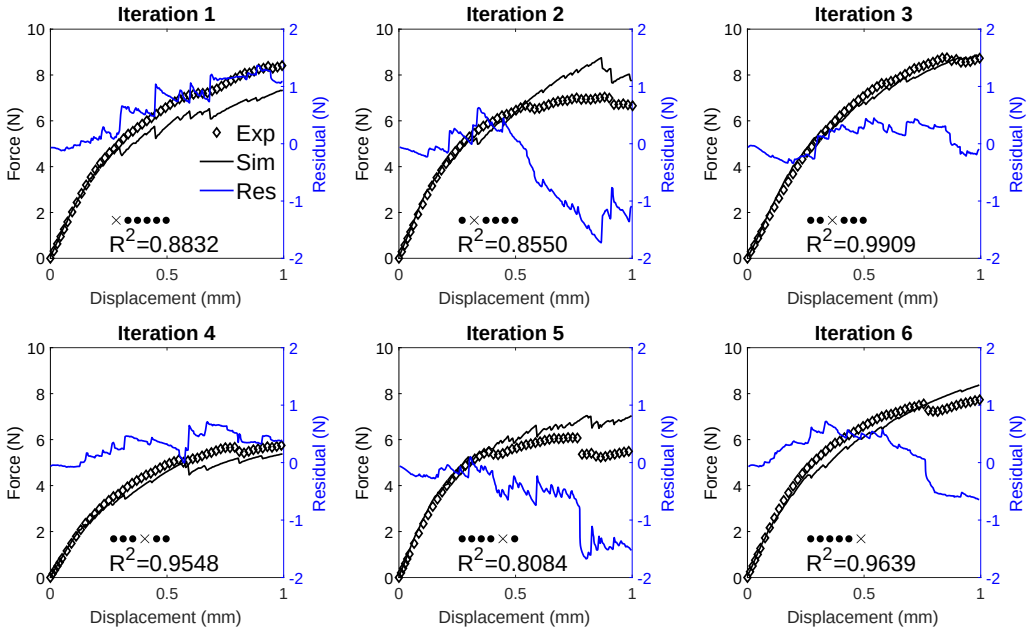

Figure 3.11: Leave-one-out cross validation results. Bond model parameters obtained from training data sets are tested on the left out test data set. The schematic label shows the partition of each iteration, where "×" represents the test data set and "•" represents the training data set. The simulated load-displacement curve, residual and R^2 value of each iteration are shown.

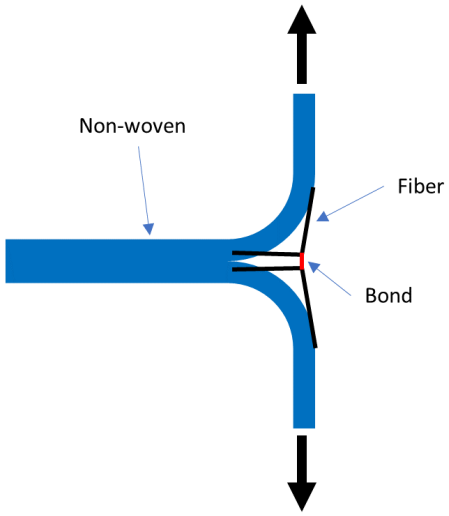

Figure 3.12: The loading approximation of the crack tip in peel tests.

where L_{seg} = 0.2mm is the fiber segment length, E = 2400MPa is the fiber modulus and R = 20μm is the fiber radius.

Summing up Equations 6 and 7, we have

$$U_{total} = (1.8 \pm 0.8)\mu\ J \tag{3.8}$$

as the predicted energy per bond fracture during the static peel test regime.

CHAPTER 4

A MICROMECHANICS-BASED DAMAGE MODEL FOR NON-WOVEN FIBER NETWORKS

4.1 Introduction

Many natural and synthetic materials have bonded fiber network structures, e.g. cytoskeleton of cells (actin micro filament networks), extracellular matrix of soft tissues (collagen fiber networks) and rubbers (molecule chain networks). Non-wovens are man-made networks of nanometer to micrometer diameter fibers. This type of material has advantageous physical properties such as high porosity, high specific strength and high damage tolerance, and hence has been widely used in fields including tissue engineering, water purification, ballistic protection and energy conversion technologies (Russell, 2006; Yoon et al., 2008; Ahmed et al., 2015; Liu et al., 2013). Accurate modeling and prediction of the mechanical properties of fiber networks remains a difficult task (Picu, 2011). The challenges arise both from complex constituent material properties and the microstructural irregularity and heterogeneity. The fibers can intrinsically be highly non-linear at finite strains and fiber-fiber bonds can break under external loading. Both intrinsic material property aspects contribute to macroscopic material non-linearity such as plasticity and damage. Microstructurally, the load transmission path within a fiber network strongly depends on network connectivity. The fiber stress distribution is often distinct from the field solution of a continuum solid. Because of the discrete and irregular microstructure, a physically sound material model for fiber network materials like non-wovens has to account for both the heterogeneity and the intrinsic nonlinearity.

Fiber network materials are typically modeled by either discrete simulations or continuum models. For the discrete modeling strategy, each fiber and bond is modeled explicitly using the finite element method. Such discrete network models have the advantage of capturing the detailed load distribution and deformation profile of a network structure. Discrete network models have been used to study the effects of microstructural features (fiber density, fiber length and bond density) on macroscopic mechanical properties (Heyden, 2000; Bronkhorst, 2003; Ridruejo et al., 2010; Kulachenko and Uesaka, 2012; Jin et al., 2013; Wilbrink et al., 2013). It has been found that fiber density plays an important role in the mechanics of fiber networks. In high density networks, fibers deform nearly affinely and individually deform axially even under local compression due to low fiber segment length to width aspect ratio. In low density networks, fibers deform non-affinely and mostly bend rather than axially compress under compressive end loads (Wilhelm and Frey, 2003; Shahsavari and Picu, 2013a,b; Chen et al., 2015). Though discrete network models capture detailed physics, they are not computationally efficient. Homogenized models are useful for large specimen simulations. In the pioneering work of Cox (1952), two dimensional non-woven small deformation elastic properties were derived theoretically assuming that each material point is an assembly of long straight non-interacting fibers. The load response of a material point can be calculated as the sum of loads carried by each constituent fiber scaled by fiber density. This concept was later extended to three dimensional and finite strain cases (Narter et al., 1999; Planas et al., 2007). In recent years, many researchers have worked towards incorporating different aspects of micromechanics such as fiber undulation, fiber bending, fiber re-orientation process and local entanglement into homogenized modeling frameworks (Pai et al., 2011b; Silberstein et al., 2012;

Raina and Linder, 2014; Martínez-Hergueta et al., 2016b).

Non-wovens experience progressive damage under external loading (Isaksson et al., 2006; Ridruejo et al., 2011). The damage comes from either interfiber bond fracture or fiber fracture. It has been found that interfiber bond damage usually starts accumulating at small strains and affects both mechanical strength and elasticity degradation. Therefore, a good understanding of bond damage mechanics is beneficial for modeling non-woven mechanical behavior. Experimental techniques, including acoustic emission detection, in-situ SEM, and in-situ computed tomography have been used to monitor bond fracture with deformation (Isaksson and Hägglund, 2007; Ridruejo et al., 2011; Chen et al., 2016a). Discrete network simulations have been used to study damage evolution laws (Aström et al., 1994; Hägglund and Isaksson, 2008; Abhilash et al., 2012). Isaksson et al. (2004) developed a constitutive model to capture anisotropic plasticity and damage evolution in paper materials. The parameters in the damage evolution law were obtained by fitting to uniaxial tensile experimental results. Ridruejo et al. (2012) used a phenomenological damage evolution law to describe the effects of bond fracture on the load carrying capacity of the fiber.

In this chapter, we present a micromechanics based constitutive model that can capture damage in different density non-woven fiber networks. First, the damage mechanisms in a network structure are briefly summarized. The constitutive equations for the model are then physically motivated and presented. Finally, a demonstrative example is presented: the proposed model is applied to a commercial non-woven series and numerical simulation results are compared with experiments. Damage evolution and localization for different density non-

wovens will be discussed.

4.2 Background of damage mechanisms in fiber networks

Mechanical testing and imaging results have shown that interfiber bond fracture is a major damage mechanism in some non-wovens including geotextiles, paper and electrospun networks (Ridruejo et al., 2011; Isaksson et al., 2006; Choi et al., 2004). From a microscopic perspective, bond fracture happens when the traction load applied on a bonded interface exceeds a critical value. It has been found that most of the bonded interfaces are broken under shear deformation mode (Mode II fracture)(Deogekar and Picu, 2018). Figure 4.1 is a schematic of undeformed and deformed configurations of a discrete fiber network with a magnified view of a bonding site. At each bonding site, there are two fibers which are separated by the bond into four fiber segments. When a fiber network is under loading, all fiber segments experience different stretches (non-affine deformation (Hatami-Marbini and Picu, 2008)), which results in a traction load on the bonded interface and drives interfacial separation.

Bond fracture reduces non-woven load carrying capacity and affects the overall mechanical behavior. Figure 4.2 is a schematic of a typical non-woven load-displacement curve under tensile loading (elastic-plastic with damage). Once damage initiates, the non-woven mechanical response deviates from that of the no damage case. The nonlinear response after damage initiates is largely determined by the damage evolution law. It has been found that network density has great effects on damage onset and evolution. Upon loading, more bonds are broken in sparse networks than dense networks (Chen et al., 2016a). We as-

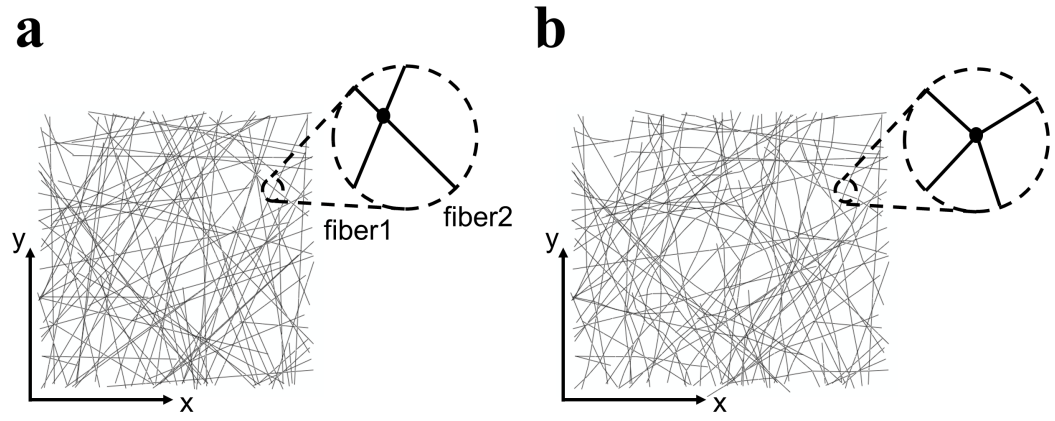

Figure 4.1: Schematic of (a) undeformed and (b) deformed configurations of a discrete fiber network with a magnified view of a typical bonding site under uniaxial tension in the x direction.

sert that the primary cause of the greater bond fracture in sparse networks than in dense networks is that local deformation in sparse networks is highly non-affine. Consequently, there is large variation in fiber segment stresses at bonding sites leading to high tractions on the bonded interface. The local deformation in dense networks is more affine, approaching the behavior of a continuum solid. Fiber segment stress along any given fiber in a dense network only deviates slightly, leading to low bond tractions. The localization zone sizes in different density non-wovens are also different. Dense networks localize damage over a thin strip of material and typically have a rupture-like failure mode. Sparse networks have a large localization zone size and corresponding gradual failure mode.

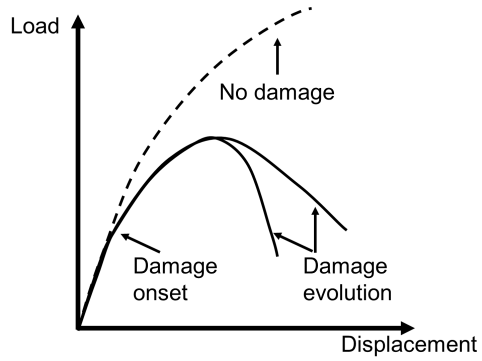

Figure 4.2: Schematic of the load-displacement curve of a non-woven with damage.

4.3 Constitutive model

Our proposed model combines an affine fiber deformation model at the network scale to obtain the overall stress response with a non-affine micromechanical model of bond sites to obtain the damage evolution. The model aims to capture the following features of non-woven macroscopic mechanical behavior:

- Elastic-plastic behavior at finite strains
- Damage progression within a large size specimen
- Damage spatial correlation and localization
- The effects of network density on damage

In the subsequent sections we describe the four parts that compose the model: network model, fiber model, bond damage model and non-local averaging scheme.

4.3.1 Network model

The network model relates the macroscopic stress response to fiber deformation and bond damage. Here, we adopt the framework developed in (Planas et al., 2007; Ridruejo et al., 2012). We focus on modeling planar layered non-wovens and therefore assume that the network structure can be simplified to a 2D continuum solid. Within each material point, there are long straight fibers oriented in different directions (Figure 4.3a). At this network level, we also assume that there is no interaction between fibers, so all fibers deform affinely. Fibers with the same orientation are grouped into one fiber set and the orientation of this fiber set is denoted as $\boldsymbol{N}^{\theta}$ (Figure 4.3b).

Helmholz free energy Ψ, defined per unit undeformed volume of the network is written as the sum of the strain energy density of each fiber set, scaled by the fiber volume fraction.

$$\Psi = \nu_f \sum_{\theta} \nu^{\theta}(1 - D^{\theta})\Phi(\boldsymbol{F}, \xi_i^{\theta}), \qquad i = 1, 2, 3, ... \tag{4.1}$$

where ν_f is fiber volume fraction, ν^{θ} is the fraction of fibers at angle $\boldsymbol{N}^{\theta}$, and Φ is fiber strain energy per unit undeformed volume without damage. The damage variable D^{θ} is incorporated here to describe the damage state associated with this fiber set. D^{θ} takes real values from 0 to 1 ($\{D^{\theta} \in \mathbb{R} | 0 \leq D^{\theta} \leq 1\}$). $D^{\theta} = 0$ indicates no bond damage on the fiber set, while $D^{\theta} = 1$ means a total loss of load carrying capacity of the fiber set. Fiber strain energy density Φ is a function of deformation gradient $\boldsymbol{F}$ (because of the affine assumption) and other necessary state variables ξ_i^{θ} within each fiber set (used for example, to describe plasticity evolution). The deformation gradient $\boldsymbol{F}$ relates deformed and undeformed configurations through $\boldsymbol{F} = \partial \boldsymbol{x} / \partial \boldsymbol{X}$ where $\boldsymbol{X}$ and $\boldsymbol{x}$ are coordinates of a material point in the undeformed and deformed configurations, respectively.

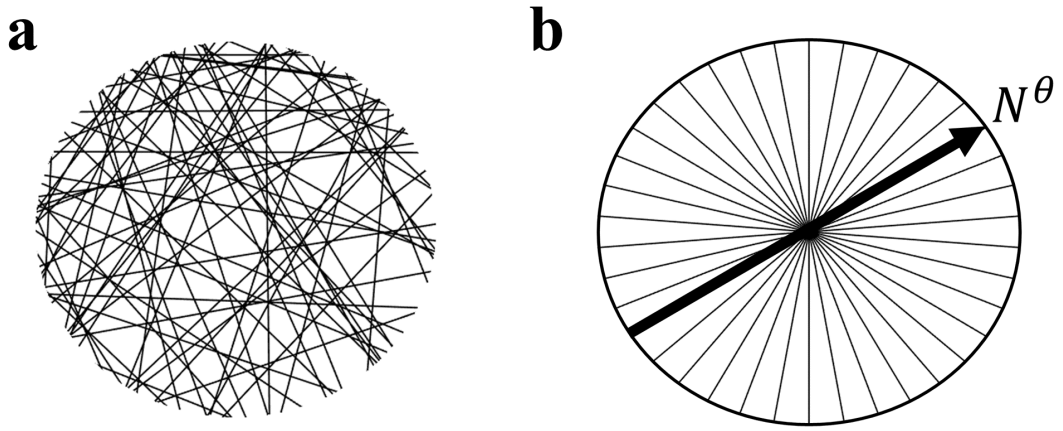

Figure 4.3: Network level concept for 2D random fiber networks. (a) Fiber network structure within a material point. (b) Equivalent continuum solid containing fiber sets unified according to orientation. Fiber set orientation is denoted as $\boldsymbol{N}^{\theta}$.

The Helmholz free energy is written as a function of $\boldsymbol{F}$, D^{θ} and ξ_i^{θ}:

$$\Psi = \Psi(\boldsymbol{F}, D^{\theta}, \xi_i^{\theta}) \tag{4.2}$$

The second law of thermodynamics states that energy dissipation of a material system should not be negative, so the following inequality holds:

$$\boldsymbol{P} : \dot{\boldsymbol{F}} - \dot{\Psi} \geq 0 \tag{4.3}$$

where $\boldsymbol{P}$ is the first Piola-Kirchhoff stress and a dot indicates a time derivative. The first term describes the mechanical power supplied to the material and the second term describes material internal energy change. Considering an isothermal process, the inequality can be expanded as:

$$(\boldsymbol{P} : \dot{\boldsymbol{F}} - \frac{\partial \Psi}{\partial \boldsymbol{F}} : \dot{\boldsymbol{F}}) - \sum_{\theta} \frac{\partial \Psi}{\partial D^{\theta}} \dot{D}^{\theta} - \sum_{\theta} \sum_{i} \frac{\partial \Psi}{\partial \xi_i^{\theta}} \dot{\xi}_i^{\theta} \geq 0 \tag{4.4}$$

Since inequality 4.4 holds for arbitrary load history, the stress response can

be calculated as:

$$\boldsymbol{P} = \frac{\partial \Psi}{\partial \boldsymbol{F}} \tag{4.5}$$

The material model should comply with thermodynamic restrictions:

$$-\frac{\partial \Psi}{\partial D^{\theta}} \dot{D}^{\theta} \geq 0, \qquad -\frac{\partial \Psi}{\partial \xi_i^{\theta}} \dot{\xi}_i^{\theta} \geq 0 \tag{4.6}$$

The fiber stretch λ^{θ} of a fiber set at direction $\boldsymbol{N}^{\theta}$ is related to macroscopic deformation gradient through:

$$\lambda^{\theta} = \sqrt{\boldsymbol{C}\boldsymbol{N}^{\boldsymbol{\theta}} \bullet \boldsymbol{N}^{\boldsymbol{\theta}}} \tag{4.7}$$

where $\boldsymbol{C} = \boldsymbol{F}^{\boldsymbol{T}}\boldsymbol{F}$ is the right Cauchy-Green deformation tensor. The stress response of a material point can be calculated as:

$$\begin{aligned} \boldsymbol{P} &= \frac{\partial \Psi}{\partial \boldsymbol{F}} \\ &= \nu_f \sum_{\theta} \nu^{\theta} (1 - D^{\theta}) \frac{\partial \Phi}{\partial \lambda^{\theta}} \frac{\partial \lambda^{\theta}}{\partial \boldsymbol{F}} \end{aligned} \tag{4.8}$$

The first derivative on the right hand side of 4.8 is evaluated by recognizing that fiber engineering stress s_f^{θ} and stretch ratio λ^{θ} are a work conjugate pair for a 1D member.

$$\frac{\partial \Phi}{\partial \lambda^{\theta}} = s_f^{\theta} \tag{4.9}$$

The second derivative contains kinematic information only and can be simplified as:

$$\begin{aligned} \frac{\partial \lambda^{\theta}}{\partial \boldsymbol{F}} &= \frac{\partial (\boldsymbol{C}\boldsymbol{N}^{\boldsymbol{\theta}} \bullet \boldsymbol{N}^{\boldsymbol{\theta}})^{\frac{1}{2}}}{\partial \boldsymbol{F}} \\ &= (\boldsymbol{C}\boldsymbol{N}^{\boldsymbol{\theta}} \bullet \boldsymbol{N}^{\boldsymbol{\theta}})^{-\frac{1}{2}} \cdot (\boldsymbol{F}\boldsymbol{N}^{\boldsymbol{\theta}} \otimes \boldsymbol{N}^{\boldsymbol{\theta}}) \end{aligned} \tag{4.10}$$

Then, the first Piola-Kirchhoff stress at a material point is:

$$\boldsymbol{P} = \nu_f \sum_{\theta} \nu^{\theta} (1 - D^{\theta}) s_f^{\theta} \frac{\boldsymbol{F}\boldsymbol{N}^{\boldsymbol{\theta}} \otimes \boldsymbol{N}^{\boldsymbol{\theta}}}{(\boldsymbol{C}\boldsymbol{N}^{\boldsymbol{\theta}} \bullet \boldsymbol{N}^{\boldsymbol{\theta}})^{\frac{1}{2}}} \tag{4.11}$$

The Cauchy stress $\boldsymbol{\sigma}$ is related to the first Piola-Kirchhoff stress through:

$$\boldsymbol{\sigma} = \frac{1}{J}\boldsymbol{P}\boldsymbol{F}^{\boldsymbol{T}} \tag{4.12}$$

where J is the determinant of $\boldsymbol{F}$. Since we are constructing a 2D continuum model, J describes material planar area change with deformation.

4.3.2 Fiber model

In the derivation of the network model, fiber strain energy density Φ does not take any specific form. Hence, any thermodynamically consistent constitutive law for the fiber can be used within the framework. In this work, we adopt a simple 1D elastic-viscoplastic model to describe fiber behavior modified from Silberstein and Boyce (2010).

We assume multiplicative decomposition of elastic and plastic stretches (Lee, 1969):

$$\lambda = \lambda^e \lambda^p \tag{4.13}$$

where λ^e is the elastic stretch and λ^p is the plastic stretch. The evolution of λ^p is related to the plastic stretch velocity gradient D^p through:

$$\dot{\lambda^p} = D^p \lambda^p \tag{4.14}$$

The elastic strain energy density of a single fiber takes the following classical quadratic form:

$$\Phi = \frac{1}{2} E_f (\lambda^e - 1)^2 \tag{4.15}$$

where E_f is the fiber elastic modulus. The engineering stress s_f is calculated by taking the derivative of strain energy density with respect to the total deformation λ:

$$s_f = E_f \frac{\lambda^e - 1}{\lambda^p} \tag{4.16}$$

The Cauchy stress is related to engineering stress through $\sigma_f = s_f \lambda$.

The magnitude of the plastic velocity gradient $\dot{\gamma}^p$ takes the following exponential form:

$$\dot{\gamma}^p = \dot{\epsilon^o} \sinh\left(\frac{|\sigma_f|}{s}\right) \tag{4.17}$$

where $\dot{\epsilon^o}$ is the pre-exponential coefficient and s is the shear resistance to plastic flow. D^p is related to $\dot{\gamma}^p$ through:

$$D^p = \dot{\gamma}^p \text{sign}(\sigma_f) \tag{4.18}$$

In modeling the roll-over yielding phenomena observed in fibers like polypropylene, the shear resistance is taken to have two parts:

$$s = s_1 + s_2 \tag{4.19}$$

The first part of the shear resistance s_1 initiates at 0 and evolves with plastic strain λ^p until s_1 reaches a saturated value s_{sat}. The second part s_2 takes a power law form with respect to λ^p:

$$\dot{s_1} = h\left(1 - \frac{s_1}{s_{sat}}\right)\dot{\gamma}^p \tag{4.20}$$

$$\dot{s_2} = s_0 (\lambda^p)^n \dot{\gamma}^p \tag{4.21}$$

where h controls the approach of s_1 to s_{sat}, s_0 is the initial value of s_2, and n is the post-yield hardening exponent.

4.3.3 Bond damage model

We zoom-in to individual bond structures to determine when a bond is broken on fiber set $\boldsymbol{N}^{\theta}$ and to evaluate the effect of a bond breaking on the damage state D^{θ}. We assume that all fiber sets follow the same damage law (note that this does not imply that they will have the same damage under macroscopic loading). As shown in Figure 4.4a, each fiber consists of many bond structures. Each bond structure (Figure 4.4b) is approximated here as one fiber at angle θ (segments 1 and 2) and one fiber at angle $\theta + 90^{o}$ (segments 3 and 4). When a bond is broken, it affects the damage states in both the θ and $\theta + 90^{o}$ orientations, therefore we consider $D^{\theta} = \max\{D^{\theta}, D^{\theta+90^{o}}\}$. Within a bond structure (θ superscript implied for the remaining portions of this section), the horizontal fiber segment stretches and engineering stresses are λ_1, λ_2, s_{f1} and s_{f2}, respectively. Under quasi-static loading, at each time step, fiber segment forces are balanced within a bond structure. The resultant force of fiber 1 and 2 is the traction load on the bonded interface. A bond breaks when this resultant force exceeds a critical value. If local deformation of a network is affine, then micro stretches λ_1 and λ_2 are equal to the overall stretch of the fiber λ, and $s_{f1} = s_{f2}$ and the traction load applied on the bond is zero. In non-wovens, however, local deformation is not affine (Hatami-Marbini and Picu, 2008). s_{f1} and s_{f2} are balanced by s_n, which is the sum of engineering stresses of segments 3 and 4 in horizontal fiber direction (Figure 4.4d).

To model the above mentioned non-affine deformation and local force balance within a continuum mechanics framework remains a difficult task. Researchers have developed a variety of approaches to provide the linkage between local deformation and macroscopic deformation. To name a few,Tkachuk

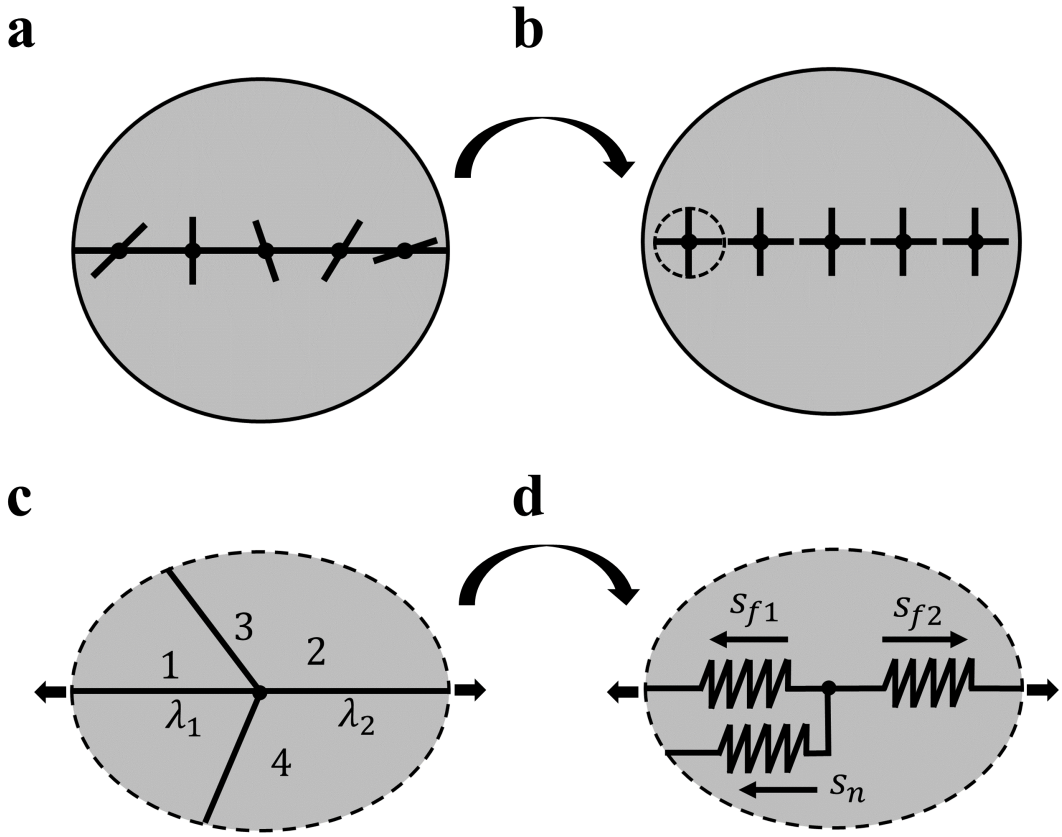

Figure 4.4: (a) Each fiber in a non-woven contains many bond structures. (b) Each bond structure contains four fiber segments and its deformation is assumed independent from each other. (c) Deformed configuration of a bond structure. (d) Engineering stresses of fiber 1 and fiber 2 are s_{f1} and s_{f2}, respectively. The contribution of fiber segments 3 and 4 in the direction of fibers 1 and 2 is replaced by term s_n. The resultant force carried by segment 3 and 4 is s_n multiplied by the initial fiber cross section area.

and Linder (2012) utilized the principle of minimum averaged free energy to determine microscopic fiber stretch, with the kinematic constraints imposed by maximum advance paths theory considered. Kroon (2011) introduced a phenomenological term into the strain energy function of rubber-like material to penalize the non-affine deformation of polymer chains. Also for modeling rubber elasticity, Miehe et al. (2004) related chain micro-stretch fluctuation to macro-stretch through a p-root averaging operator.

In this work, our strategy is to solve the boundary value problem of fibers stretching at a bond site and hence determine the traction load on the bonded interface. We introduce a phenomenological description of s_n to model local force balance at a bond. Assuming that at any given macroscopic deformation $\boldsymbol{F}$ the directions of s_{f1} and s_{f2} are always in line with $\boldsymbol{FN}$ and all fibers have the same initial fiber diameter d:

$$s_{f1} + s_n - s_{f2} = 0 \tag{4.22}$$

The phenomenological term s_n takes the following form:

$$s_n = \frac{P}{(1-D)^\beta} \frac{s_{f1}^3}{E_f^2} \tag{4.23}$$

where P and β are model parameters. The form of s_n is inspired by the elastic solution to stretching a fiber-fiber crossing at small strains (see appendix, section 4.6). Introducing s_n is equivalent to adding a nonlinear spring between the ends of fiber segment 1. s_n drives the differences between the micro-stretches in segment 1 and 2 and from macro-stretch λ, so the affine field assumed in the network model is converted to a non-affine field analogous to the real physical picture. Parameter P describes the degree of non-affinity in a fiber network in the undamaged state. $P = 0$ indicates fully affine deformation, i.e. $s_{f1} = s_{f2}$. Greater P indicates a greater non-affine micro deformation field. Parameter β

controls the evolution of s_n with damage. Greater β corresponds to the degree of non-affinity increasing more rapidly with bond damage.

Another boundary condition for the local force balance on the bond structure comes from the constraints of the surrounding network. The network deforms affinely when $s_n = 0$. Fiber segment engineering stresses (s_{f1} and s_{f2}) are then equal to the overall fiber stress $(1 - D)s_f$ in equation 4.11, where s_f is related to fiber macro-stretch λ. Fiber segment stretches (λ_1 and λ_2) are equal to fiber macro-stretch λ. By introducing s_n, s_{f2} is greater than $(1 - D)s_f$, and $\lambda_1 + \lambda_2 \neq 2\lambda$. We assume superposition is applicable when comparing the two cases of $s_n = 0$ and $s_n \neq 0$. Introducing s_n leads to a change in fiber stress s_{f2} which can be seen as a pulling force on the surrounding network. This pulling force causes the combined end to end length of fibers 1 and 2 to shrink by $l(2\lambda - \lambda_1 - \lambda_2)$, where l is fiber segment length. This physical picture can be approximated as a pressure dipole acting on a continuum solid (see appendix, section 4.6). The following equation then holds:

$$s_{f2} - (1 - D)s_f = \eta E_n(2\lambda - \lambda_1 - \lambda_2) \tag{4.24}$$

where coefficient η is a function of d, l and network thickness t. Here, E_n is equal to initial network modulus $\frac{1}{3}\nu_f E_f$ (Cox, 1952) scaled by the damage state on this fiber:

$$E_n = \frac{1}{3}\nu_f(1 - D)E_f \tag{4.25}$$

Fiber stresses s_{f1} and s_{f2} are related to stretches λ_1 and λ_2 through the fiber constitutive laws. Using equations 4.23 and 4.24 and fiber constitutive laws, λ_1 and λ_2 as well as s_{f1} and s_{f2} can be determined.

Having fiber stresses at hand, the resultant force acting on a bonded interface can be calculated by $\frac{\pi}{4}d^2(s_{f2} - s_{f1})$. We assume that all bonds break in a brittle

manner with bond strength (b) on the fiber set. We define the damage activation function as:

$$\Phi_d = \frac{\pi d^2}{4}(s_{f2} - s_{f1}) - b \tag{4.26}$$

where Φ_d only takes non-positive values. Φ_d is a function of D and current fiber stress states, and defines a damage surface in stress space. When $\Phi_d < 0$, damage is not activated. When $\Phi_d = 0$, the damage state is updated. The damage model is supplemented by the two loading-unloading conditions given as equations 4.27 and 4.28 (Simo and Hughes, 2006). The Kuhn-Tucker condition:

$$\dot{D} \geq 0, \qquad \Phi_d \leq 0, \qquad \dot{D}\Phi_d = 0 \tag{4.27}$$

states that when Φ_d is not activated ($\Phi_d < 0$), the damage variable is not updated ($\dot{D} = 0$); when damage is accumulating ($\dot{D} > 0$), $\Phi_d = 0$. The persistency condition:

$$\dot{D}\dot{\Phi}_d = 0, \qquad \text{if} \quad \Phi_d = 0 \tag{4.28}$$

states that damage is only evolving ($\dot{D} > 0$) when the stress state is moving on the damage surface ($\dot{\Phi}_d = 0$ and $\Phi_d = 0$).

The kinetic law of damage evolution is defined through the functional relation between Φ_d and D. Fiber stresses are solved through equations 4.23 and 4.24, hence they are functions of D. The physical meaning of b is the survival bond strength at D. Consider that each bond structure is independent from each other and its bond strength is a random draw from the bond strength distribution. At damage state D, a fiber set loses a fraction D of the load carrying capacity (network scale model equation 4.11) and a fraction D of bonds are broken on the fiber set. Within this construct, bonds with lower bond strength always

break first, so b is a quantile and is related to D through:

$$b = CDF^{-1}(D) \tag{4.29}$$

where CDF is bond strength cumulative distribution function. Equation 4.29 completes the local constitutive damage model of individual fiber set at angle θ.

4.3.4 Non-local averaging scheme

The non-local averaging scheme introduced in this section is used to model the spatial correlation of damage events in the fiber network structure. The constitutive equations presented in sections 4.3.1, 4.3.2, 4.3.3 are local, that is the deformation and stress response of a local material point are directly related. However, damage in a fiber network has non-local effects. Because of fiber connectivity within the network, a bond fracture has direct influence on load transmission far away from the bond location (Isaksson and Hägglund, 2009). Further, a local constitutive law with damage (softening) model would lead to mesh dependent finite element (FE) results (Jirásek and Bažant, 2002). The damage zone would localize into a single strip of elements and the total energy dissipation would decrease as the mesh is refined. Physically, the source of this problem is that a stress-strain based constitutive law defines energy dissipation based on material volume, whereas damage events in a material (generation of micro-cracks or micro-voids, or breaking bonded interfaces in non-wovens) create new surfaces and hence traction-displacement constitutive laws should be used. One remedy for this problem is to introduce a length scale to convert energy dissipation from a per volume basis into a per area basis.

In this work, we apply the non-local damage theory presented in Jirásek

(1998) and Bažant (1999). The idea of this non-local damage theory is to replace the variable that controls material softening by its non-local counterpart. Here, we introduce $\bar{\lambda}^\theta$ as the non-local version of fiber stretch λ^θ. For a material point at $\boldsymbol{x}$, $\bar{\lambda}^\theta$ is taken as a weighted sum of local fiber stretch λ^θ of all the material points in surrounding domain A (Jirásek and Bažant, 2002):

$$\bar{\lambda}^\theta(\boldsymbol{x}) = \int_A \alpha(\boldsymbol{x}, \boldsymbol{\xi}) \lambda^\theta(\boldsymbol{\xi}) d\boldsymbol{\xi} \tag{4.30}$$

where $\alpha(\boldsymbol{x}, \boldsymbol{\xi})$ is a given non-local function. $\alpha(\boldsymbol{x}, \boldsymbol{\xi})$ is scaled such that $\bar{\lambda}^\theta(\boldsymbol{x}) = \lambda^\theta(\boldsymbol{x})$ when the deformation field is uniform.

$$\alpha(\boldsymbol{x}, \boldsymbol{\xi}) = \frac{\alpha_0(\|\boldsymbol{x} - \boldsymbol{\xi}\|)}{\int_A \alpha_0(\|\boldsymbol{x} - \boldsymbol{\zeta}\|) d\boldsymbol{\zeta}} \tag{4.31}$$

$\|\boldsymbol{x} - \boldsymbol{\zeta}\|$ is the Euclidean distance between $\boldsymbol{x}$ and $\boldsymbol{\zeta}$. The weight function $\alpha_0(r)$ takes the following Gaussian form:

$$\alpha_0(r) = \exp[-(2r/l_{ch})^2] \tag{4.32}$$

where l_{ch} is the length scale parameter. It is assumed that there is no interaction between two material point when $r > l_{ch}$. In an FE setting, after local fiber stretch λ^θ is updated at one incremental step, its value is then replaced by $\bar{\lambda}^\theta$. Physically, l_{ch} describes the maximum interaction distance within a fiber network and is related to the initial network microstructure.

4.4 Results and discussion

As a demonstrative example, we apply the proposed model to a set of commercial non-wovens, the Dupont Typar geotextile series. Three non-wovens with different densities are considered: SF20, SF32 and SF65. These materials are made through the same manufacturing process and are all composed of

polypropylene fibers connected by thermal bonds. In the following sections, previously published experimental characterization results of these materials are summarized. Then, the parameter values used in the model and a parameter study are presented. Finally, numerical simulation results are discussed and compared with experiments.

4.4.1 Experimental results summary

Mechanical characterization results of the constituent fiber, fiber-fiber bonds and these non-woven bulk materials are detailed in Chen et al. (2016a) and Chen and Silberstein (2018) and are briefly summarized here. The constituent fiber has diameter of $40 - 60\mu$m and its mechanical behavior is elastic-plastic (Figure 4.5a). The bond strength statistical distribution takes a Weibull form (Figure 4.5b). The cumulative density function of bond strength is

$$CDF(b) = 1 - e^{-(b/b_1)^{b_2}}, \qquad b \geq 0 \tag{4.33}$$

where b is the bond strength in N, $b_1 = 0.0778$N and $b_2 = 1.14$. The uniaxial tensile response of three non-wovens of size 9mm×27mm are shown in Figure 4.6. All three types of non-wovens have a short elastic region, a roll-over yield region and a highly damaged (softening) region after the peak load. The mechanical behavior variation among specimens of a particular type is significant, arising mainly from the randomness of the material microstructure. After scaling mechanical properties with network density, it was found that all three non-wovens have similar scaled modulus but the high density non-woven has higher mechanical strength.

In-situ micro computed tomography was used in combination with tensile

tests to monitor broken bond quantities in these non-wovens. Change in fraction of surviving bonds with deformation is plotted as the inset of Figure 4.6. In the high density non-woven (SF65), bond damage is not significant until the rupture failure, whereas in the low density non-woven (SF20), a substantial number of bonds are broken starting from small strains.

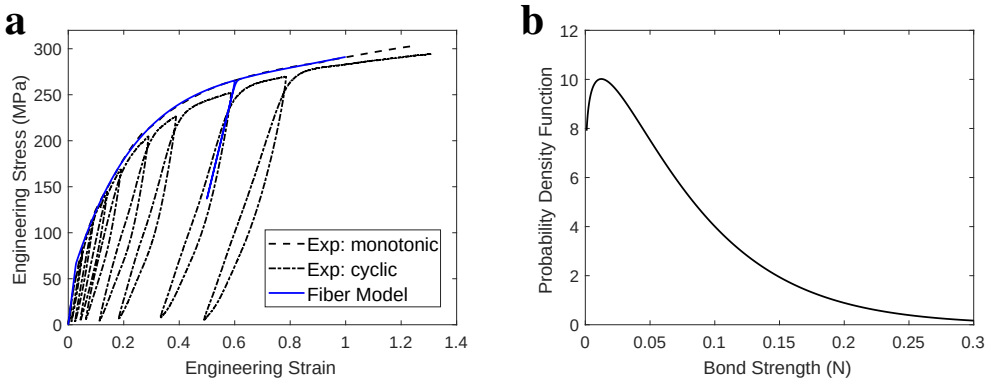

Figure 4.5: Experimental characterization results of constituent fibers and bonds. (a) Monotonic tensile and cyclic behaviors of polypropylene fiber. The 1-D viscoplastic model response is overlaid. (b) Bond strength probability density distribution.

4.4.2 Model parameters

The model parameters used in our simulation are summarized in Table 4.1. Fiber density and fiber diameter values of the three non-wovens are taken from the manufacturer product datasheet (DuPont, 2014). Fiber segment length l and network thickness t in the micro-force balance equation 4.24 are taken from Chen et al. (2016a). Based on our imaging results, fibers are uniformly distributed within the plane. Therefore, fibers are grouped into 20 fiber sets with angles uniformly spanning across $[0, \pi)$. Fiber elastic modulus E_f is directly measured from the fiber tensile stress-strain curve. The pre-exponential coef-

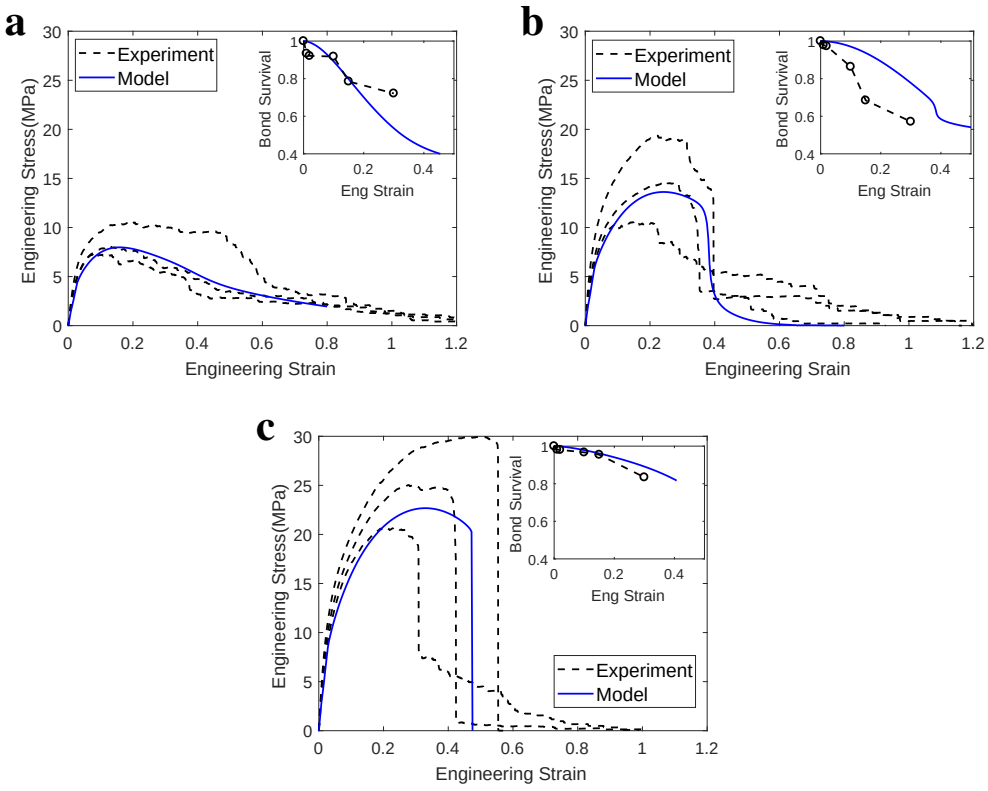

Figure 4.6: Experimental and simulation stress-strain curves of (a)SF20, (b)SF32 and (c)SF65. The three experimental curves represent maximum, median and minimal strength cases. Simulation results are depicted with blue lines. Surviving bond fraction measured by in-situ micro computed tomography and predicted by simulation are compared in the insets.

ficient $\dot{\epsilon}_0$ is taken as a very small value due to limited fiber time dependent behavior. The other four parameters that control fiber plastic flow (initial shear resistance s_0, post-hardening exponent n, rate of shear resistance evolution h and saturated shear resistance s_{sat}) are obtained by fitting the viscoplastic model response to the fiber monotonic tensile experimental data (Figure 4.5a). The bond strength distributions in three non-wovens are taken as the same since all these materials are manufactured through the same process.

Local damage is controlled by parameters P and β. Fiber segment stresses,

micro-stretches and damage evolution with deformation (far field stretch λ) within one fiber set for two sets of P and β are shown in Figure 4.7. By introducing the non-affinity term s_n, the micro-stretches of the two fiber segments (λ_1 and λ_2) deviate from the far field stretch. Damage initiates at small strains since the bond strength distribution skews to low strength values. This early initiation is consistent with experimental observations in Ridruejo et al. (2011). Parameter P describes how far local deformation is from affine deformation. Dense networks are closer to a continuum solid, so P will take a lower value than for sparse networks. Parameter β describes the increase in non-affinity with damage accumulation and hence prescribes the damage evolution rate. A dense network has rapid damage accumulation after localization, so β is expected to take a high value. Figures 4.7a-b are for $P = 30$ and $\beta = 0.1$, values corresponding to a sparse network. In this case, both fiber segment stresses increase monotonically. Figures 4.7c-d are for $P = 4$ and $\beta = 1.6$. In this case, the damage evolution rate is lower at the early stage of deformation than the sparse network case. The two fiber segments have similar stress response before the rupture failure (far field stretch ≈ 1.6) and both experience some unloading after this major damage event. The exact values of P and β for each areal density are chosen to fit the uniaxial tensile stress-strain curves.

Parameter l_{ch} describes the spatial correlation of damage. It controls the strain at which localization occurs and damage zone sizes. Figure 4.8 shows the effects of l_{ch} on the macroscopic stress-strain behavior. When $l_{ch} = 27$mm, the whole specimen deforms homogeneously and localization does not occur. For the other cases, the stress-strain curves deviate from the homogeneous deformation case. The bifurcation point is when damage starts to localize in one part of the specimen. A smaller l_{ch} leads to a more drastic decrease in load carry

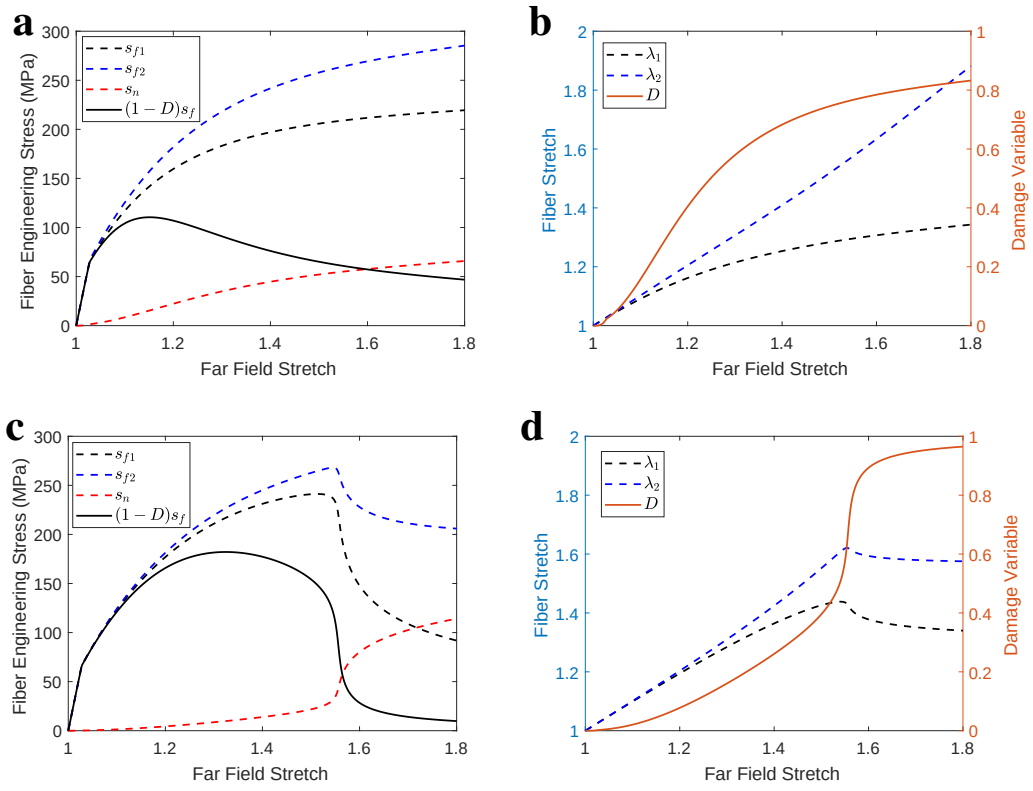

Figure 4.7: Non-affine deformation and damage on a single fiber population. (a)-(b) $P = 30, \beta = 0.1$. (c)-(d) $P = 4, \beta = 1.6$. Fiber segment engineering stresses s_{f1} and s_{f2} (left) and stretches λ_1, λ_2 (right) are plotted. s_n is the magnitude of non-affinity term introduced. $(1 - D)s_f$ is the overall stress carried by a fiber set.

capacity after the peak load and a smaller damage localization zone size. The direct linkage between l_{ch} and network geometry is not yet clear. In the gradient enhanced damage model developed in Isaksson et al. (2004), the internal length scale was taken as two times of fiber length. For the Typar non-wovens we consider in this work, the fibers are longer than the specimens, so l_{ch} should instead be comparable with the specimen dimensions. l_{ch} is taken as 9.0mm (specimen width) for the sparse network (SF20). For SF32 and SF65, l_{ch} is assumed to scale relative to SF20 with network areal weight.

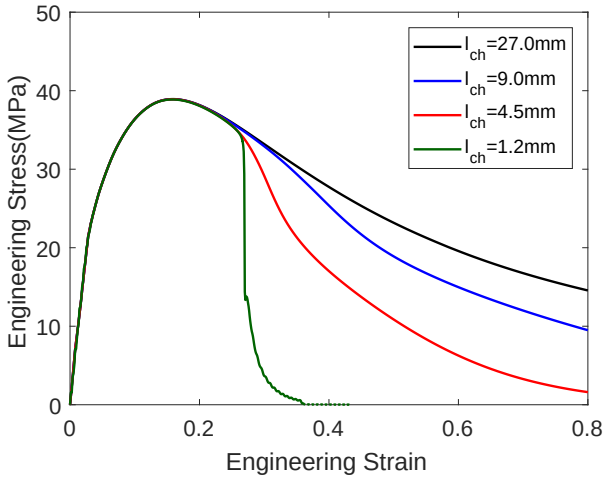

Figure 4.8: The effects of length scale l_{ch} on macroscopic stress-strain curves. The other model parameters are the same as SF20 in Table 4.1.

4.4.3 Full specimen simulation results

The proposed model is implemented into the commercial FE package ABAQUS as a user subroutine VUMAT. The 9mm$\times$27mm specimen domain is discretized into 20×60 CPS4R elements (2D four node bi-linear element with reduced integration). One element in the middle of the specimen domain has $0.9\nu_f$ and serves as a "defect" to guide the location of damage localization. The introduction of this small "defect" does not affect the macroscopic mechanical response prior to localization. Element deletion is triggered when overall damage at a material point $\sum_\theta \nu^\theta D^\theta$ is greater than 0.999. For uniaxial tension, one short edge of the specimen has fixed Cartesian coordinates and the other short edge moves in the loading direction with constant speed at 0.1mm/s. Two lateral edges are traction free. The loading speed is chosen to approximate quasi-static loading condition. All simulations in this work use ABAQUS/Explicit as FE solver.

The stress-strain curves from these simulations are superposed on the cor-

Table 4.1: Model parameters

Model component	Parameter	SF20	SF32	SF65
Network geometry	ν_f	0.205	0.270	0.394
	ν^θ	1/20	1/20	1/20
	l	0.24mm	0.19mm	0.13mm
	t	0.35mm	0.45mm	0.59mm
	d	0.05mm	0.05mm	0.05mm
Fiber properties	E_f	2400MPa		
	$\dot{\epsilon}_0$	10^{-18}		
	s_0	1.73MPa		
	n	4.96		
	h	41.55MPa		
	s_{sat}	10.68MPa		
Bond properties	b_1	0.0778N		
	b_2	1.14		
Damage	P	30	8	4
	β	0.1	1.0	1.6
	l_{ch}	9.0mm	5.4mm	2.7mm

responding experimental results in Figure 4.6. It can be seen that our proposed model can capture the non-linear hardening and post peak damage region for all three types of non-wovens. In the low density non-woven (SF20), peak load is achieved at smaller strain compared to SF32 and SF65, indicating that more damage is accumulated during the early stages of deformation. The damage evolution after the peak load in SF20 is gradual. In the high density non-woven (SF65), after the material reaches the peak load, the stress response first grad-

ually decreases and then drops rapidly when damage localization occurs. For the intermediate density non-woven (SF32), in the median specimen, stress response drops rapidly after the peak load just like SF65. After this major damage event, the specimen can still carry load since there are still a few fibers connecting the two ends. The gradual SF32 behavior can be fit with P and β values intermediate to those of SF20 and SF65. It should be noted that in all three non-wovens a great amount of damage is developed before the peak load. The non-linear hardening region is a result of both fiber plastic straining and network damage accumulation, which are explicitly included in the model. The bond survival fraction corresponding to each simulation is shown in the insets of Figure 4.6. It is shown that the damage evolution predicted by the FE simulation matches well with the imaging results, further validating the model.

To evaluate the ability of the model to capture damage localization sizes in different density non-wovens, we compared the simulated and experimental deformed configurations of SF20 and SF65. It can be seen experimentally that in SF20 the damage localization zone is quite large (over half of the specimen area), whereas in SF65, damage develops from small regions and ruptures the sample (Figure 4.9). This difference in damage localization zone size is well captured by the FE simulations (Figure 4.10). At a strain of 0.1, both SF20 and SF65 have almost homogeneous damage distributions, but the magnitude of damage in SF20 is higher. In the post-localization regime, the damage zone in SF20 is much larger than in SF65.

The mechanical behaviors of the three types of non-wovens have great specimen to specimen variations (Figure 4.6). One source of this variation is that different specimens have different fiber volume fractions v_f. In order to model

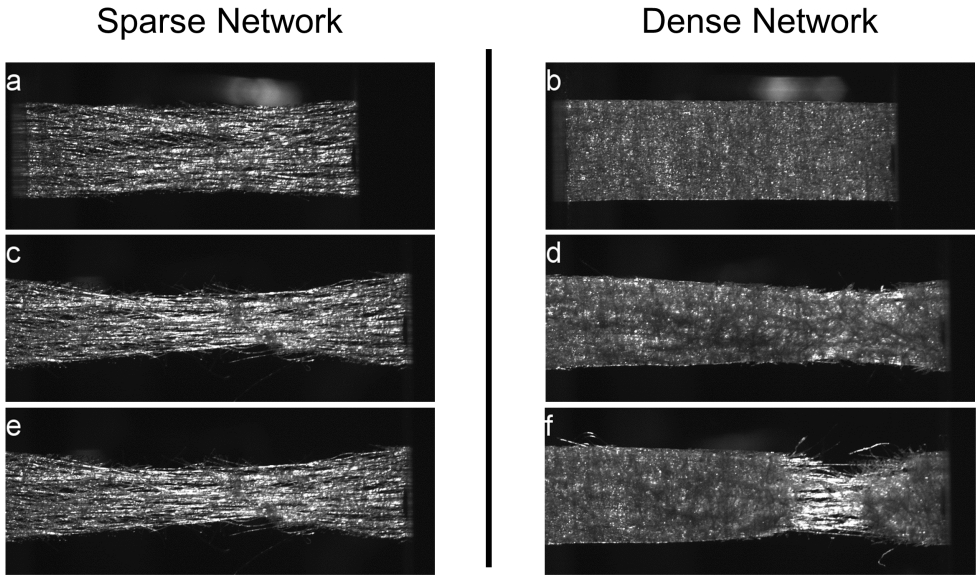

Figure 4.9: Images of SF20 (a, c, e) and SF65 (b, d, f) at engineering strains ϵ = 0.1, 0.43 (before SF65 rupture failure) and 0.43 (after SF65 rupture failure).

this variation, we characterized v_f variation in three types of non-wovens experimentally. Table 4.2 lists v_f values of five specimens of each type of non-woven cut from different regions in a raw bulk material. The mean and standard deviation of v_f are reported. (Note that the v_f measurements are different from the manufacturer datasheet. This is probably because the micrometer compression force is different so the thickness measurement is different). We calculated the ratio between the v_f of each specimen and the mean value, and used these ratios to adjust v_f in the model. In Figure 4.11, the blue bands are the model predicted specimen to specimen variation of mechanical behaviors. The band width increases following the sequence of SF20, SF65 and SF32. In all three type of materials, volume fraction variation is not sufficient to capture the full band of observed behavior. Other sources of the variation include variation of

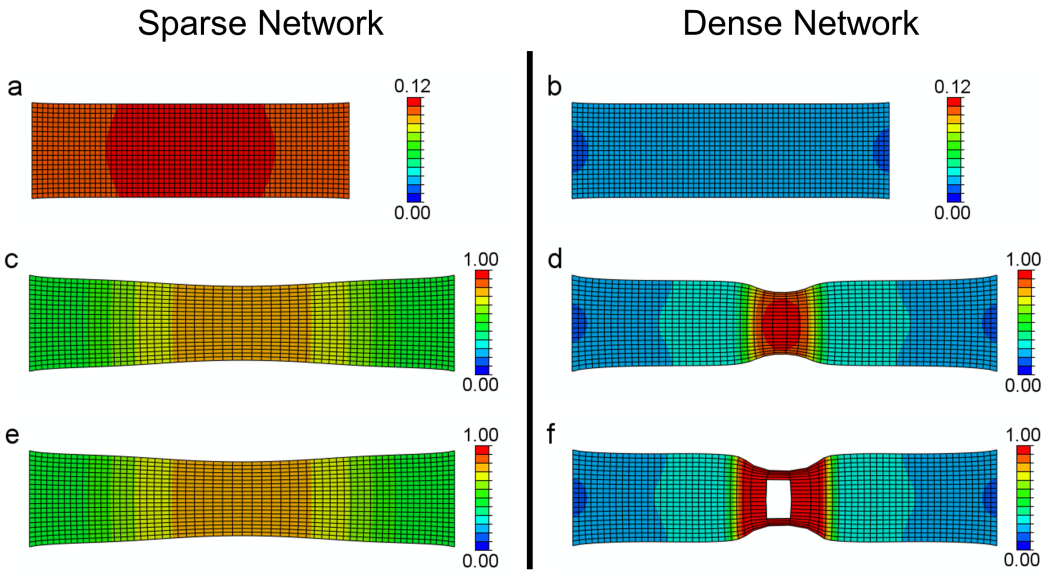

Figure 4.10: Damage contours of SF20 (a, c, e) and SF65 (b, d, f) at engineering strains ϵ = 0.1, 0.47 (before SF65 rupture failure) and 0.47 (after SF65 rupture failure).

bond strength distributions and spatial heterogeneity within a specimen. Both of these two sources can be easily incorporated in the proposed model. More detailed analysis and characterization is needed to provide quantitative information of these two material heterogeneities. (A discussion of heterogeneity and size effect in different fiber network materials can be found in Shahsavari and Picu (2013b)).

4.5 Conclusion

In this chapter, we present a micromechanically based damage model for nonwoven fiber networks. The constitutive equations are established by modeling the individual interfiber bond breaking process and then relating the fraction of

Table 4.2: Fiber volume fraction characterization results

	SF20	SF32	SF65
Specimen 1	0.269	0.338	0.510
Specimen 2	0.276	0.380	0.452
Specimen 3	0.306	0.349	0.502
Specimen 4	0.279	0.307	0.497
Specimen 5	0.303	0.402	0.481
Average	0.29	0.36	0.49
Standard deviation	0.02	0.04	0.02

bond breakage to the macroscopic non-woven stress. We introduce a physically-inspired phenomenological term to describe non-affine deformation of fibers at a bonding site. The effects of network structure on the degree of non-affinity is considered in this term. By solving a boundary value problem at a bonding site, we determine the traction load on a bonded interface and hence determine whether a bond is broken. The spatial correlation of damage is an intrinsic characteristic of a fiber network. We use a non-local averaging scheme to model this mechanism. The proposed model is applied on a series commercial non-wovens as a demonstrative example. The model reproduces all the features of a uniaxial tensile curve including the elastic and plastic slopes, peak load and degradation after peak load. The damage localization zone size qualitatively matches with experimental observations. The accuracy of microscopic damage information (fraction of bond damage) predicted by the model is confirmed by comparing with μCT imaging results.

This model can be applied to all fiber network materials where inter-fiber bond damage is a major damage mechanism. The model incorporates network

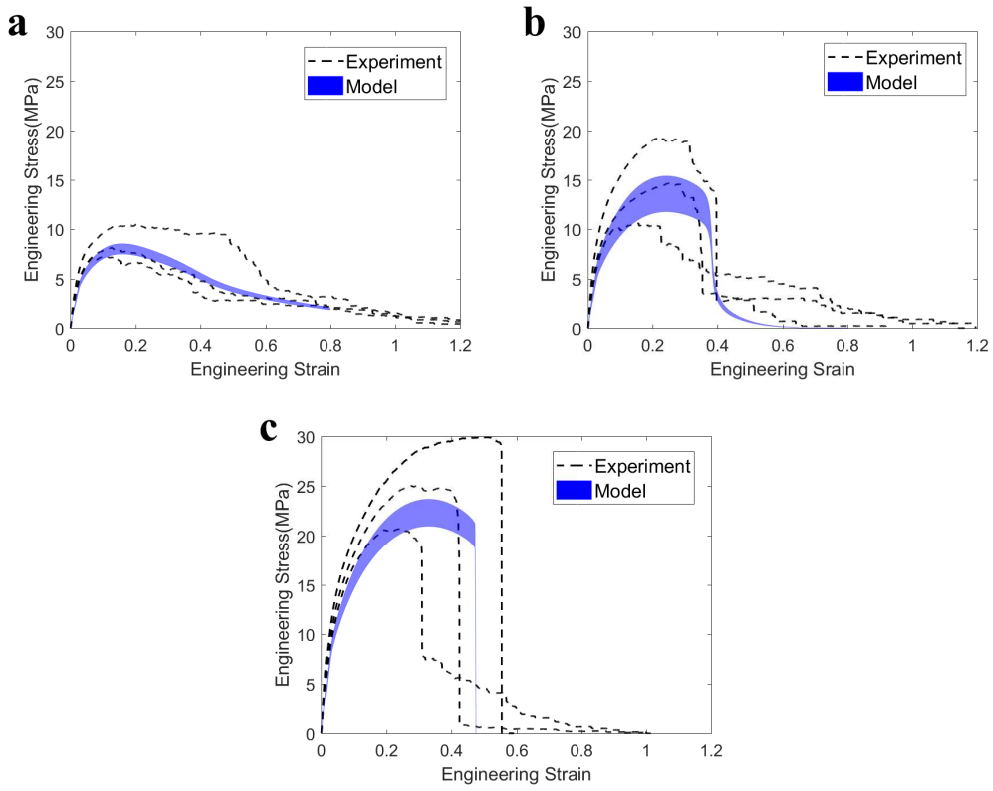

Figure 4.11: Model predicted variations in stress-strain curves (blue band) when variations of fiber volume fraction v_f is incorporated. The black lines are experimental results as detailed in the previous sections.

microstructural effects on damage and network internal length scales. It can be further used to study the fracture behaviors of non-wovens, like crack-tip damage zone sizes and crack growth. It can also be used to predict strength and toughness of non-wovens with different sizes.

4.6 Appendix

Appendix A: Elastic solution of single bond deformation

A simplified boundary value problem for a bond structure deforming is shown in Figure 4.12. One horizontal fiber of length $2l$ (segment 1 and 2) and one vertical fiber of length $k \times 2l$ (segment 3 and 4) are connected at a bond. In this simplified model, all the bonds are modeled as rotating joints (Picu, 2011) so fiber axial deformation mode is the dominate deformation mode. This is because axial stress transfer mode instead of fiber bending is the major load transfer mechanism in a fiber network material (Räisänen et al., 1997). One end of segments 1, 3 and 4 are connected to the surrounding network, and their Cartesian coordinates are fixed. As the free end of segment 2 is pulled, all fiber segments deform and their strains are denoted as $\epsilon_1, \epsilon_2, \epsilon_3$, and ϵ_4. The average strain of segment 1 and 2 is ϵ. Assuming small deformation, the strains can be calculated as:

$$\epsilon_1 = k \tan\theta \tag{4.34}$$

$$\epsilon_2 = 2\epsilon - k \tan\theta \tag{4.35}$$

$$\epsilon_3 = \epsilon_4 = \frac{1}{\cos\theta} - 1 \tag{4.36}$$

where θ is the angle between segment 3 and the vertical direction. The fibers are assumed to be linear elastic with elastic modulus E_f. Equilibrium at a bonding site is:

$$2E_f\epsilon_3 \sin\theta + E_f\epsilon_1 - E_f\epsilon_2 = 0 \tag{4.37}$$

The traction load on the bonded interface is:

$$\begin{aligned} s_n &= 2E_f \epsilon_3 \sin\theta \\ &= 2E_f \left(\frac{\epsilon_1}{k} - \sqrt{\frac{\epsilon_1^2}{k^2 + \epsilon_1^2}} \right) \end{aligned} \tag{4.38}$$

Performing a Taylor expansion of the above equation at $\epsilon_1 = 0$ and taking only the first term, we have:

$$\begin{aligned} s_n &= E_f \left(\frac{\epsilon_1^3}{k^3} + h.o.t \right) \\ &\approx \frac{s_{f1}^3}{k^3 E_f^2} \end{aligned} \tag{4.39}$$

where s_{f1} is fiber stress in segment 1. For finite deformation, anchors that move with the network and elastic-plastic fiber behavior, we therefore propose a traction load of the form $s_n = \frac{P}{(1-D)^\beta} \frac{s_{f1}^3}{E_f^2}$ (equation 4.23).

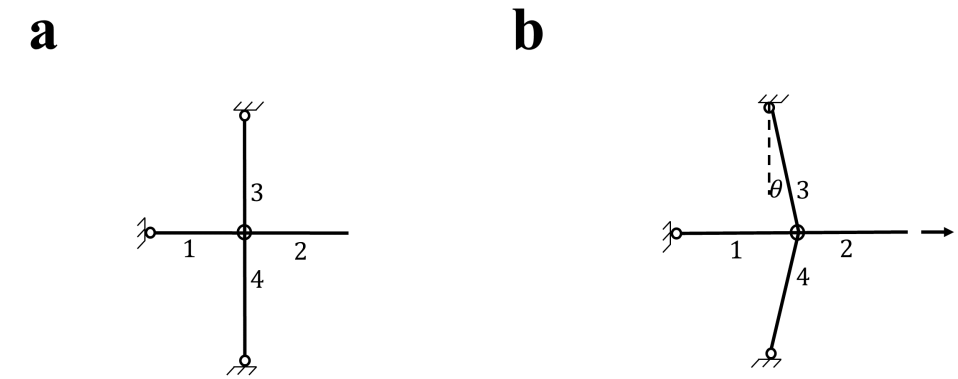

Figure 4.12: A bond structure in (a) undeformed and (b) deformed configurations.

Appendix B: Elastic solution of a pressure dipole on an infinite plate

In this section, we provide the analytical solution of a pressure dipole on an infinite plate problem and relate this solution to the boundary condition in equation 4.24. Introducing the non-affinity term s_n to our bond structure model makes fiber segment stress s_{f2} greater than in the affine deformation case $(1-D)s_f$. This change in fiber stress makes the two ends of the horizontal fiber closer by $l(2\lambda - \lambda_1 - \lambda_2)$ (segment 1 and 2 in Figure 4.13) . In order to find the relationship between this change in fiber stress and network shrinkage, we approximate this configuration as a pressure dipole (fiber stress) applied on an infinite plate (network) (Figure 4.14b). To solve the pressure dipole problem, we first consider the that a point force P (unit [N/m], a line load in thickness direction) is applied on an infinite plate (Figure 4.14a). The stress field of this problem is given in Timoshenko and Goodier (1951):

$$\begin{aligned} \sigma_{rr} &= -\frac{(3+\nu)}{4\pi}\frac{P\cos\theta}{r} \\ \sigma_{\theta\theta} &= \frac{1-\nu}{4\pi}\frac{P\cos\theta}{r} \\ \sigma_{r\theta} &= \frac{1-\nu}{4\pi}\frac{P\sin\theta}{r} \end{aligned} \tag{4.40}$$

where (r,θ) is the polar coordinate of a point of interest. Assuming that the solid is linear elastic and plane stress conditions hold, one can obtain the strain field using $\epsilon_{rr} = \frac{1}{E}\sigma_{rr} - \frac{\nu}{E}\sigma_{\theta\theta}$, $\epsilon_{\theta\theta} = \frac{-\nu}{E}\sigma_{rr} + \frac{1}{E}\sigma_{\theta\theta}$ and $\epsilon_{r\theta} = \frac{1+\nu}{E}\sigma_{r\theta}$ as:

$$\begin{aligned} \epsilon_{rr} &= \frac{(\nu-3)(\nu+1)}{4\pi E}\frac{P\cos\theta}{r} \\ \epsilon_{\theta\theta} &= \frac{(\nu+1)^2}{4\pi E}\frac{P\cos\theta}{r} \\ \epsilon_{r\theta} &= \frac{1-\nu^2}{4\pi E}\frac{P\sin\theta}{r} \end{aligned} \tag{4.41}$$

where E and ν are elastic modulus and Poisson' s ratio of the elastic solid. The displacement field (u_r, u_θ) is related to strain field through $\epsilon_{rr} = \frac{\partial u_r}{\partial r}$, $\epsilon_{\theta\theta} = \frac{u_r}{r} + \frac{1}{r}\frac{\partial u_\theta}{\partial \theta}$ and $\epsilon_{r\theta} = \frac{1}{2}\left(\frac{1}{r}\frac{\partial u_r}{\partial \theta} + \frac{\partial u_\theta}{\partial r} - \frac{u_\theta}{r}\right)$. The displacement field can therefore be calculated by integrating equation 4.41.

$$\begin{aligned} u_r &= \frac{-k_1}{\pi E} P \cos\theta \ln\frac{r}{m} \\ u_\theta &= \frac{-k_1}{\pi E} P \sin\theta \ln\frac{m}{r} + \frac{k_2}{\pi E} P \sin\theta \end{aligned} \tag{4.42}$$

where m is an integration constant that represents rigid body movement. The displacement $u_r = 0$ at location $(r, \theta) = (m, 0)$. k_1 and k_2 are defined as:

$$\begin{aligned} k_1 &= -\frac{\nu^2 - 2\nu - 3}{4} \\ k_2 &= \frac{(\nu + 1)^2}{4} \end{aligned} \tag{4.43}$$

On the vertical plane ($x = 0$), the indentation distance is:

$$u_0 = u_\theta|_{\theta=-\frac{\pi}{2}} = \frac{k_1}{\pi E} P \ln\frac{m}{r} - \frac{k_2}{\pi E} P \tag{4.44}$$

We now extend the above solution to the pressure dipole problem in Figure 4.14b. Pressure load 1 with magnitude q is applied on $x = 0, 0 \le y \le d$, pointing to positive x direction. Pressure load 2 with the same magnitude is applied on $x = L, 0 \le y \le d$, pointing to negative x direction. L is two times fiber segment length l. For each pressure load, the displacement field can be calculated by integrating the point load solution equation 4.42 over the area of this applied pressure. The indentation distance profile on $x = 0$ plane caused by pressure load 1 is $v_1(y)$:

$$\tilde{v_1} = \frac{q}{\pi E}\left\{k_1\Big[\ln\tilde{m} - \tilde{y}\ln\tilde{y} - (1-\tilde{y})\ln(1-\tilde{y})\Big] + k_1 - k_2\right\} \tag{4.45}$$

where we have introduced normalized variables $\tilde{v_1} = v_1/d, \tilde{y} = y/d$ and $\tilde{m} = m/d$. The indentation distance profile on $x = L$ plane caused by pressure load 1 is

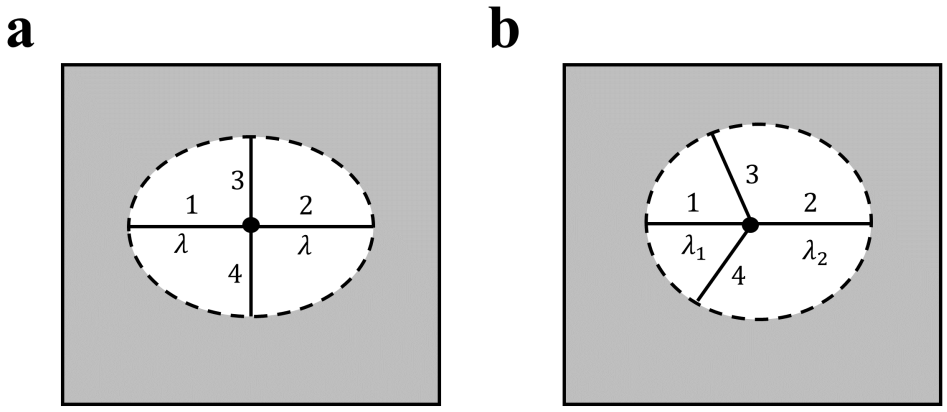

Figure 4.13: (a) Affine deformation of a bond structure. Fiber stretches in segment 1 and 2 are the same and can be calculated from equation 4.7. (b) Non-affine deformation of a bond structure. Fiber stretches in segment 1 and 2 are different. The relationship between these two physical pictures is approximated by a pressure dipole on an infinite plate problem.

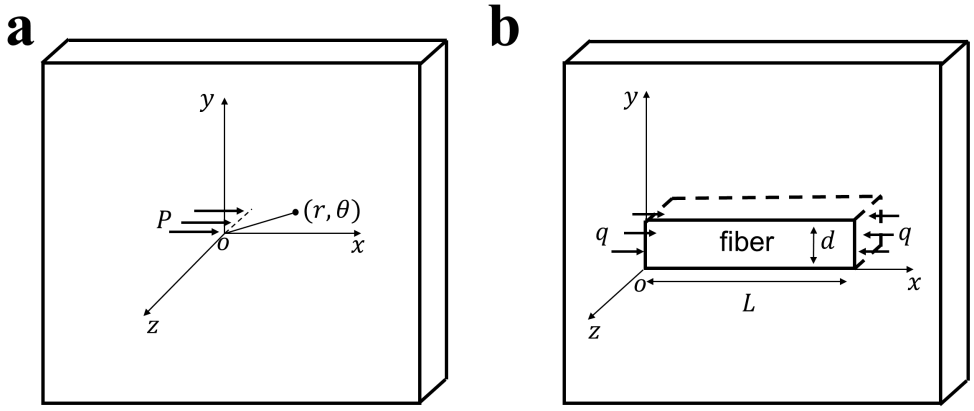

Figure 4.14: (a) A line load P applied on an infinite plate. P is in plane and is defined as force per unit length in thickness direction. (b) A pressure dipole q applied on an infinite plate. q is related to fiber stress through equation 4.49

$v_2(y)$ (normalized variables: $\tilde{v_2} = v_2/d, \tilde{L} = L/d$):

$$\begin{aligned}\tilde{v_2} = \frac{q}{\pi E}\Bigg\{k_1 \ln \frac{\tilde{m}}{\sqrt{\tilde{L}^2 + (1-\tilde{y})^2}} + k_1 \tilde{y} \ln \frac{\sqrt{\tilde{L}^2 + (1-\tilde{y})^2}}{\sqrt{\tilde{L}^2 + \tilde{y}^2}} \\ -(k_1 + k_2)\Bigg[1 + \tilde{L}\arctan\left(-\frac{\tilde{y}}{\tilde{L}}\right) - \tilde{L}\arctan\left(\frac{1-\tilde{y}}{\tilde{L}}\right)\Bigg]\Bigg\}\end{aligned} \tag{4.46}$$

The total indentation profile on plane $x = 0$ is $w(y)$ (normalized variable: $\tilde{w} = w/d$).

$$\tilde{w} = \tilde{v_1} - \tilde{v_2} \tag{4.47}$$

Average indentation distance over the area where the pressure load is applied ($x = 0, 0 \le y \le d$) is:

$$\bar{\tilde{w}} = \int_0^1 \tilde{w} d\tilde{y} \tag{4.48}$$

We apply the above solution to the boundary condition in equation 4.24.

$$s_{f2} - (1-D)s_f = \eta E_n (2\lambda - \lambda_1 - \lambda_2)$$

The goal is to determine η based on network microstructure geometry. We consider fiber stress $s_{f2} - (1-D)s_f$ is evenly distributed over the network thickness direction, so pressure q in the pressure dipole problem can be calculated as:

$$\frac{\pi}{4} d^2 [s_{f2} - (1-D)s_f] = q \cdot t \cdot d \tag{4.49}$$

where t is network thickness. The average indentation distance is horizontal fiber length differences between affine and non-affine case (Figure 4.13):

$$\bar{\tilde{w}} = \frac{l}{2d}(2\lambda - \lambda_1 - \lambda_2) \tag{4.50}$$

The coefficient η is then evaluated as:

$$\eta = \frac{2t}{d} \cdot \frac{l}{K} \tag{4.51}$$

where

$$K = \int_0^1 (\tilde{v_1} - \tilde{v_2}) \cdot \frac{\pi E}{q} d\tilde{y} \tag{4.52}$$

CHAPTER 5

CONCLUSION AND FUTURE WORK

5.1 Conclusion

The overarching goals of this dissertation are (1) to provide an accurate physical picture of non-woven damage mechanics (2) to build a physically sound and computationally efficient non-woven material model. To achieve these goals, I first performed mechanical tests on a series of non-wovens with in-situ imaging techniques incorporated. The effects of network microstructure on deformation mechanisms, and the linkage between deformation mechanisms and macroscopic behaviors were elucidated (Chapter 2). In high fiber density non-wovens, bond density was high and fiber segments were short. Fiber segments had low aspect ratios (stubby) so bending deformation mode was suppressed and fiber alignment process was not significant until peak load. Dense networks had less bond damage than sparse ones before peak load. The mechanical strength of dense networks was also higher. Before moving on to material modeling, I found that there is no effective method for characterizing bond properties even though bond fracture is a major damage mechanism. Motivated by this need, I developed a new method for bond strength characterization and this method was presented in Chapter 3. In addition to providing bond strength values, the image based discrete network model and the artificial network model can be further used to study micromechanics of all fiber network materials. Finally, the observed micromechanics information was incorporated into a homogenized model to capture damage at finite strains. The proposed model links network microstructure features to macroscopic response and hence can provide guid-

ance on manufacturing processes and help facilitate future material design.

5.2 Future work

One interesting possible extension of this work is to explicitly investigate the fracture behavior of non-wovens. Several researchers have tested non-wovens with cracks or notches. Some interesting phenomena were observed:

- The damage process zone in low density paper was quite large. In a single edge crack specimen, the crack did not always grow along the original crack plane and the directions of crack growth paths had great specimen to specimen variation. The damage process zone in high density paper was small and the crack grew straight ahead following the prediction of maximum hoop stress theory (Isaksson and Hägglund, 2009; Isaksson et al., 2012).
- Some glass fiber felts were notch-insensitive, that is the mechanical strength was independent of notch size. Two mechanisms were presented in Ridruejo et al. (2010) and Chen et al. (2016b) that explain this phenomenon: (1) the randomness in fiber layout and bond properties lead to the presence of "weak paths" in a network structure and fracture may not localize at the crack (2) fibers far away from the crack transmit loads away from the crack and reduce the severity of the stress concentration.
- Some tissue scaffolds had significant crack blunting at finite deformations. Under mode-I loading, fibers ahead of the crack tended to group together, aligned along the loading direction and forming a "shield" on the crack. This crack-blunting mechanism strengthens material and increases

its load carrying capacity. This explains the inverse notch-sensitivity phenomenon observed in some geotextiles (Koh et al., 2013; Koh and Oyen, 2015; Ridruejo et al., 2015).

These experimental observations are distinct from the predictions of classical fracture mechanics theory. This difference is due to the internal length scale of a network structure (fiber length) being comparable with macroscopic length scales (specimen size, crack length). The interplay between these two length scales is not yet clear. Theoretical frameworks and predictive models for non-woven fracture behavior have not been well established, especially for finite deformation cases. The numerical tools developed in this dissertation (discrete network model in Chapter 3 and homogenized model in Chapter 4) can be further used to study the crack-tip field, crack growth and fracture criteria of non-wovens.

Second interesting extension would be to find a master curve that relates non-woven microstructure features (fiber density, fiber aspect ratio, crosslink density, etc.) to macroscopic properties (elastic modulus, strength, toughness). Such master curves have been established in Head et al. (2003); Wilhelm and Frey (2003); Shahsavari and Picu (2013a), but the results are all based on small deformation assumptions and nonlinearities in fiber and bond behaviors are not considered. It has been shown that interfiber bond breakage can happen starting from small strains, and a lot of non-wovens experience great structural change under finite deformations. The bond strength data and discrete network model presented in Chapter 3 can be used to establish such a master curve and to predict material strength and toughness. The advancement of modern manufacturing methods, like 3-D printing, makes it possible to quickly prototype new

non-wovens. These manufacturing methods in combination with the characterization methods in Chapter 2 can be useful in validating theoretical predictions from the master curves. The establishment of such master curves would greatly benefit future non-woven material design.

BIBLIOGRAPHY

Abhilash, A., Purohit, P.K., Joshi, S.P., 2012. Stochastic rate-dependent elasticity and failure of soft fibrous networks. Soft Matter 8, 7004–7016. doi:10.1039/c2sm25450f.

Ahmed, F.E., Lalia, B.S., Hashaikeh, R., 2015. A review on electrospinning for membrane fabrication: challenges and applications. Desalination 356, 15–30. doi:10.1016/j.desal.2014.09.033.

Andreassen, E., Myhre, O.J., Hinrichsen, E.L., Braathen, M.D., Grøstad, K., 1995. Relationships between the properties of fibers and thermally bonded nonwoven fabrics made of polypropylene. Journal of Applied Polymer Science 58, 1633–1645.

Aström, J., Saarinen, S., Niskanen, K., Kurkijärvi, J., 1994. Microscopic mechanics of fiber networks. Journal of Applied Physics 75, 2383–2392. doi:10.1063/1.356259.

Bažant, Z.P., 1999. Size effect on structural strength: a review. Archive of Applied Mechanics 69, 703–725. doi:10.1007/s004190050252.

Berhan, L., Sastry, A., 2003. On modeling bonds in fused, porous networks: 3d simulations of fibrous–particulate joints. Journal of Composite Materials 37, 715–740. doi:10.1177/002199803029725.

Bhat, G.S., Jangala, P.K., Spruiell, J.E., 2004. Thermal bonding of polypropylene nonwovens: effect of bonding variables on the structure and properties of the fabrics. Journal of Applied Polymer Science 92, 3593–3600.

Bower, A.F., 2009. Applied mechanics of solids. CRC press.

Bronkhorst, C., 2003. Modelling paper as a two-dimensional elastic–plastic stochastic network. International Journal of Solids and Structures 40, 5441–5454. doi:10.1016/S0020-7683(03)00281-6.

Buell, S., Rutledge, G.C., Vliet, K.J.V., 2010. Predicting polymer nanofiber interactions via molecular simulations. ACS Applied Materials & Interfaces 2, 1164–1172. doi:10.1021/am1000135.

Chen, N., Koker, M.K., Uzun, S., Silberstein, M.N., 2016a. In-situ x-ray study of the deformation mechanisms of non-woven polypropylene. International Journal of Solids and Structures 97, 200–208. doi:10.1016/j.ijsolstr.2016.07.028.

Chen, N., Silberstein, M., 2018. Determination of bond strengths in non-woven fabrics: a combined experimental and computational approach. Experimental Mechanics 58, 343–355. doi:10.1007/s11340-017-0346-3.

Chen, Y., Pan, F., Guo, Z., Liu, B., Zhang, J., 2015. Stiffness threshold of randomly distributed carbon nanotube networks. Journal of the Mechanics and Physics of Solids 84, 395–423. doi:10.1016/j.jmps.2015.07.016.

Chen, Y., Ridruejo, A., González, C., Llorca, J., Siegmund, T., 2016b. Notch effect in failure of fiberglass non-woven materials. International Journal of Solids and Structures 96, 254–264. doi:10.1016/j.ijsolstr.2016.06.004.

Choi, S.S., Lee, S.G., Joo, C.W., Im, S.S., Kim, S.H., 2004. Formation of interfiber bonding in electrospun poly (etherimide) nanofiber web. Journal of Materials Science 39, 1511–1513. doi:10.1023/B:JMSC.0000013931.84760.b0.

Cox, H., 1952. The elasticity and strength of paper and other fibrous materials.

British Journal of Applied Physics 3, 72. doi:10.1088/0508-3443/3/3/302.

Demirci, E., Acar, M., Pourdeyhimi, B., Silberschmidt, V.V., 2011. Finite element modelling of thermally bonded bicomponent fibre nonwovens: tensile behaviour. Computational Materials Science 50, 1286–1291. doi:10.1016/j.commatsci.2010.02.039.

Deogekar, S., Picu, R., 2018. On the strength of random fiber networks. Journal of the Mechanics and Physics of Solids doi:10.1016/j.jmps.2018.03.026.

DuPont, 2014. Dupont Typar Geosynthetics Technical Datasheet. Technical Report. URL: http://www.dupont.co.uk/content/dam/dupont/products-and-services/construction-materials/geotextiles/documents/Typar-UK/Typar-UK-Technical-Datasheets/Typar-UK-datasheets-EU.pdf.

Greiner, A., Wendorff, J.H., 2007. Electrospinning: a fascinating method for the preparation of ultrathin fibers. Angewandte Chemie International Edition 46, 5670–5703. doi:10.1002/anie.200604646.

Hägglund, R., Isaksson, P., 2008. On the coupling between macroscopic material degradation and interfiber bond fracture in an idealized fiber network. International Journal of Solids and Structures 45, 868–878. doi:10.1016/j.ijsolstr.2007.09.011.

Hatami-Marbini, H., Picu, R., 2008. Scaling of nonaffine deformation in random semiflexible fiber networks. Physical Review E 77, 062103. doi:10.1103/PhysRevE.77.062103.

Hatami-Marbini, H., Picu, R., 2009. Heterogeneous long-range correlated deformation of semiflexible random fiber networks. Physical Review E 80, 046703. doi:10.1103/PhysRevE.80.046703.

Head, D., Levine, A., MacKintosh, F., 2003. Distinct regimes of elastic response and deformation modes of cross-linked cytoskeletal and semiflexible polymer networks. Physical Review E 68, 061907. doi:10.1103/PhysRevE.68.061907.

Heyden, S., 2000. Network modelling for evaluation of mechanical properties of cellulose fibre fluff. volume 1011. Susanne Heyden, Division of Structural Mechanics, Box 118, 221 00 Lund, Sweden,.

Huang, Z.M., Zhang, Y.Z., Kotaki, M., Ramakrishna, S., 2003. A review on polymer nanofibers by electrospinning and their applications in nanocomposites. Composites Science and Technology 63, 2223–2253. doi:10.1016/S0266-3538(03)00178-7.

Iijima, M., Strobl, G., 2000. Isothermal crystallization and melting of isotactic polypropylene analyzed by time-and temperature-dependent small-angle x-ray scattering experiments. Macromolecules 33, 5204–5214.

Isaksson, P., Dumont, P., Du Roscoat, S.R., 2012. Crack growth in planar elastic fiber materials. International Journal of Solids and Structures 49, 1900–1907. doi:10.1016/j.ijsolstr.2012.03.037.

Isaksson, P., Gradin, P., Kulachenko, A., 2006. The onset and progression of damage in isotropic paper sheets. International Journal of Solids and Structures 43, 713–726. doi:10.1016/j.ijsolstr.2005.04.035.

Isaksson, P., Hägglund, R., 2007. Evolution of bond fractures in a randomly distributed fiber network. International Journal of Solids and Structures 44, 6135–6147. doi:10.1016/j.ijsolstr.2007.02.013.

Isaksson, P., Hägglund, R., 2009. Structural effects on deformation and fracture of random fiber networks and consequences on continuum models. International Journal of Solids and Structures 46, 2320–2329. doi:10.1016/j.ijsolstr.2009.01.027.

Isaksson, P., Hägglund, R., Gradin, P., 2004. Continuum damage mechanics applied to paper. International Journal of Solids and Structures 41, 4731–4755. doi:10.1016/j.ijsolstr.2004.02.043.

Jearanaisilawong, P., 2008. A continuum model for needlepunched nonwoven fabrics. Ph.D. thesis. Massachusetts Institute of Technology.

Jeon, S.Y., Na, W.J., Choi, Y.O., Lee, M.G., Kim, H.E., Yu, W.R., 2014. In situ monitoring of structural changes in nonwoven mats under tensile loading using x-ray computer tomography. Composites Part A: Applied Science and Manufacturing 63, 1–9. doi:10.1016/j.compositesa.2014.03.019.

Jin, M., Chen, C., Lu, T., 2013. The mechanical behavior of porous metal fiber sintered sheets. Journal of the Mechanics and Physics of Solids 61, 161–174. doi:10.1016/j.jmps.2012.08.006.

Jirásek, M., 1998. Nonlocal models for damage and fracture: comparison of approaches. International Journal of Solids and Structures 35, 4133–4145. doi:10.1016/S0020-7683(97)00306-5.

Jirásek, M., Bažant, Z.P., 2002. Inelastic analysis of structures. John Wiley & Sons.

Jubera, R., Ridruejo, A., González, C., LLorca, J., 2014. Mechanical behavior and deformation micromechanisms of polypropylene nonwoven fabrics as a function of temperature and strain rate. Mechanics of Materials 74, 14–25. doi:10.1016/j.mechmat.2014.03.007.

Koh, C., Oyen, M.L., 2015. Toughening in electrospun fibrous scaffolds. APL Materials 3, 014908. doi:10.1063/1.4901450.

Koh, C.T., Strange, D., Tonsomboon, K., Oyen, M., 2013. Failure mechanisms in fibrous scaffolds. Acta Biomaterialia 9, 7326–7334. doi:10.1016/j.actbio.2013.02.046.

Koubaa, A., Koran, Z., 1995. Measure of the internal bond strength of paper/board. Tappi Journal 78, 103–112.

Kroon, M., 2011. An 8-chain model for rubber-like materials accounting for non-affine chain deformations and topological constraints. Journal of Elasticity 102, 99–116. doi:10.1007/s10659-010-9264-7.

Kulachenko, A., Uesaka, T., 2012. Direct simulations of fiber network deformation and failure. Mechanics of Materials 51, 1–14. doi:10.1016/j.mechmat.2012.03.010.

Lee, E.H., 1969. Elastic-plastic deformation at finite strains. Journal of Applied Mechanics 36, 1–6.

Lee, S.J., Oh, S.H., Liu, J., Soker, S., Atala, A., Yoo, J.J., 2008. The use of thermal treatments to enhance the mechanical properties of electrospun poly (-caprolactone) scaffolds. Biomaterials 29, 1422–1430. doi:10.1016/j.biomaterials.2007.11.024.

Liu, D.S., Ashcraft, J.N., Mannarino, M.M., Silberstein, M.N., Argun, A.A., Rutledge, G.C., Boyce, M.C., Hammond, P.T., 2013. Spray layer-by-layer electrospun composite proton exchange membranes. Advanced Functional Materials 23, 3087–3095. doi:10.1002/adfm.201202892.

Martínez-Hergueta, F., Ridruejo, A., Gálvez, F., González, C., LLorca, J., 2016a. Influence of fiber orientation on the ballistic performance of needlepunched nonwoven fabrics. Mechanics of Materials 94, 106–116. doi:10.1016/j.mechmat.2015.11.019.

Martínez-Hergueta, F., Ridruejo, A., González, C., Llorca, J., 2015. Deformation and energy dissipation mechanisms of needle-punched nonwoven fabrics: a multiscale experimental analysis. International Journal of Solids and Structures 64, 120–131. doi:10.1016/j.ijsolstr.2015.03.018.

Martínez-Hergueta, F., Ridruejo, A., González, C., LLorca, J., 2016b. A multiscale micromechanical model of needlepunched nonwoven fabrics. International Journal of Solids and Structures 96, 81–91. doi:10.1016/j.ijsolstr.2016.06.020.

Michielsen, S., Jain, S., 2010. Thermal bonding of nonwovens as simulated by polypropylene films: effect of time, temperature, and molecular weight. Journal of Applied Polymer Science 117, 3322–3330. doi:10.1002/app.31220.

Michielsen, S., Pourdeyhimi, B., Desai, P., 2006. Review of thermally point-bonded nonwovens: materials, processes, and properties. Journal of Applied Polymer Science 99, 2489–2496. doi:10.1002/app.22858.

Miehe, C., Göktepe, S., Lulei, F., 2004. A micro-macro approach to rubber-like materialspart i: the non-affine micro-sphere model of rubber elasticity. Jour-

nal of the Mechanics and Physics of Solids 52, 2617–2660. doi:10.1016/j.jmps.2004.03.011.

Narter, M.A., Batra, S.K., Buchanan, D.R., 1999. Micromechanics of three-dimensional fibrewebs: constitutive equations, in: Proceedings of the Royal Society of London A: Mathematical, Physical and Engineering Sciences, The Royal Society. pp. 3543–3563. doi:10.1098/rspa.1999.0465.

Nelder, J.A., Mead, R., 1965. A simplex method for function minimization. The Computer Journal 7, 308–313.

OctopusImaging, 2013. Octopus 8.7. URL: https://octopusimaging.eu/octopus/octopus-reconstruction.

Ortiz, M., Pandolfi, A., 1999. Finite-deformation irreversible cohesive elements for three-dimensional crack-propagation analysis. International Journal for Numerical Methods in Engineering 44, 1267–1282.

Pai, C.L., Boyce, M.C., Rutledge, G.C., 2011a. Mechanical properties of individual electrospun pa 6 (3) t fibers and their variation with fiber diameter. Polymer 52, 2295–2301. doi:10.1016/j.polymer.2011.03.041.

Pai, C.L., Boyce, M.C., Rutledge, G.C., 2011b. On the importance of fiber curvature to the elastic moduli of electrospun nonwoven fiber meshes. Polymer 52, 6126–6133. doi:10.1016/j.polymer.2011.10.055.

Picu, R., 2011. Mechanics of random fiber networksa review. Soft Matter 7, 6768–6785. doi:10.1039/c1sm05022b.

Planas, J., Guinea, G., Elices, M., 2007. Constitutive model for fiber-reinforced materials with deformable matrices. Physical Review E 76, 041903. doi:10.1103/PhysRevE.76.041903.

Popov, V., 2010. Contact mechanics and friction: physical principles and applications. Springer Science & Business Media.

Raina, A., Linder, C., 2014. A homogenization approach for nonwoven materials based on fiber undulations and reorientation. Journal of the Mechanics and Physics of Solids 65, 12–34. doi:10.1016/j.jmps.2013.12.011.

Räisänen, V., Alava, M., Niskanen, K., Nieminen, R., 1997. Does the shear-lag model apply to random fiber networks? Journal of Materials Research 12, 2725–2732.

Ridruejo, A., González, C., LLorca, J., 2010. Damage micromechanisms and notch sensitivity of glass-fiber non-woven felts: An experimental and numerical study. Journal of the Mechanics and Physics of Solids 58, 1628–1645. doi:10.1016/j.jmps.2010.07.005.

Ridruejo, A., González, C., LLorca, J., 2011. Micromechanisms of deformation and fracture of polypropylene nonwoven fabrics. International Journal of Solids and Structures 48, 153–162. doi:10.1016/j.ijsolstr.2010.09.013.

Ridruejo, A., González, C., LLorca, J., 2012. A constitutive model for the in-plane mechanical behavior of nonwoven fabrics. International Journal of Solids and Structures 49, 2215–2229. doi:10.1016/j.ijsolstr.2012.04.014.

Ridruejo, A., Jubera, R., González, C., LLorca, J., 2015. Inverse notch sensitivity: cracks can make nonwoven fabrics stronger. Journal of the Mechanics and Physics of Solids 77, 61–69. doi:10.1016/j.jmps.2015.01.004.

Russell, S.J., 2006. Handbook of nonwovens. Woodhead Publishing.

Schmied, F.J., Teichert, C., Kappel, L., Hirn, U., Bauer, W., Schennach, R., 2013. What holds paper together: nanometre scale exploration of bonding between paper fibres. Scientific Reports 3, 2432. doi:10.1038/srep02432.

Schmied, F.J., Teichert, C., Kappel, L., Hirn, U., Schennach, R., 2012. Joint strength measurements of individual fiber-fiber bonds: an atomic force microscopy based method. Review of Scientific Instruments 83, 073902. doi:10.1063/1.4731010.

Shahsavari, A., Picu, R., 2012. Model selection for athermal cross-linked fiber networks. Physical Review E 86, 011923. doi:10.1103/PhysRevE.86.011923.

Shahsavari, A., Picu, R., 2013a. Elasticity of sparsely cross-linked random fibre networks. Philosophical Magazine Letters 93, 356–361. doi:10.1080/09500839.2013.783241.

Shahsavari, A., Picu, R., 2013b. Size effect on mechanical behavior of random fiber networks. International Journal of Solids and Structures 50, 3332–3338. doi:10.1016/j.ijsolstr.2013.06.004.

Silberstein, M.N., Boyce, M.C., 2010. Constitutive modeling of the rate, temperature, and hydration dependent deformation response of nafion to monotonic and cyclic loading. Journal of Power Sources 195, 5692–5706. doi:10.1016/j.jpowsour.2010.03.047.

Silberstein, M.N., Pai, C.L., Rutledge, G.C., Boyce, M.C., 2012. Elastic–plastic behavior of non-woven fibrous mats. Journal of the Mechanics and Physics of Solids 60, 295–318. doi:10.1016/j.jmps.2011.10.007.

Simo, J.C., Hughes, T.J., 2006. Computational inelasticity. volume 7. Springer Science & Business Media. doi:10.1007/b98904.

TheMathworks, 2015. Matlab R2015a. URL: http://www.mathworks.com/products/matlab/.

ThermoFisherScientific, 2014. AVIZO Fire 8.1. URL: http://www.fei.com/software/avizo3d/.

Timoshenko, S., Goodier, J., 1951. Theory of elasticity. McGraw-Hill.

Tkachuk, M., Linder, C., 2012. The maximal advance path constraint for the homogenization of materials with random network microstructure. Philosophical Magazine 92, 2779–2808. doi:10.1080/14786435.2012.675090.

Torgnysdotter, A., Kulachenko, A., Gradin, P., Wgberg, L., 2007a. Fiber/fiber crosses: finite element modeling and comparison with experiment. Journal of Composite Materials 41, 1603–1618. doi:10.1177/0021998306069873.

Torgnysdotter, A., Kulachenko, A., Gradin, P., Wgberg, L., 2007b. The link between the fiber contact zone and the physical properties of paper: a way to control paper properties. Journal of Composite Materials 41, 1619–1633. doi:10.1177/0021998306069875.

Tötzke, C., Gaiselmann, G., Osenberg, M., Bohner, J., Arlt, T., Markötter, H., Hilger, A., Wieder, F., Kupsch, A., Müller, B.R., et al., 2014. Three-dimensional study of compressed gas diffusion layers using synchrotron x-ray imaging. Journal of Power Sources 253, 123–131. doi:10.1016/j.jpowsour.2013.12.062.

Wernersson, E.L., Borodulina, S., Kulachenko, A., Borgefors, G., 2014. Characterisations of fibre networks in paper using micro computed tomography

images. Nord Pulp Pap Res J 29, 468–475. doi:10.3183/NPPRJ-2014-29-03-p468-475.

Wilbrink, D., Beex, L., Peerlings, R., 2013. A discrete network model for bond failure and frictional sliding in fibrous materials. International Journal of Solids and Structures 50, 1354–1363. doi:10.1016/j.ijsolstr.2013.01.012.

Wilhelm, J., Frey, E., 2003. Elasticity of stiff polymer networks. Physical Review Letters 91, 108103. doi:10.1103/PhysRevLett.91.108103.

Williams, G., Watts, D.C., 1970. Non-symmetrical dielectric relaxation behaviour arising from a simple empirical decay function. Transactions of the Faraday society 66, 80–85. doi:10.1039/tf9706600080.

Yano, T., Higaki, Y., Tao, D., Murakami, D., Kobayashi, M., Ohta, N., Koike, J.i., Horigome, M., Masunaga, H., Ogawa, H., et al., 2012. Orientation of poly (vinyl alcohol) nanofiber and crystallites in non-woven electrospun nanofiber mats under uniaxial stretching. Polymer 53, 4702–4708. doi:10.1016/j.polymer.2012.07.067.

Yoon, K., Hsiao, B.S., Chu, B., 2008. Functional nanofibers for environmental applications. Journal of Materials Chemistry 18, 5326–5334. doi:10.1039/b804128h.

Yousefi Shivyari, N., Tajvidi, M., Bousfield, D.W., Gardner, D.J., 2016. Production and characterization of laminates of paper and cellulose nanofibrils. ACS Applied Materials & Interfaces 8, 25520–25528. doi:10.1021/acsami.6b07655.

Yuranov, I., Renken, A., Kiwi-Minsker, L., 2005. Zeolite/sintered metal fibers composites as effective structured catalysts. Applied Catalysis A: General 281, 55–60. doi:10.1016/j.apcata.2004.11.012.